The Electronic Structure of the Oxygen Adsorbed Surface by Angle-resolved Photoelectron Spectroscopy: (Ag 110), Ni (110) and Ag (110)

Lyo CHIWA

The Electronic Structures of the Oxygen Adsorbed Surface by Angle-resolved Photoelectron Spectroscopy: Cu(110), Ni(110) and Ag(110)

Ryo OZAWA

A dissertation submitted to the Doctoral Program in Physics,
University of Tsukuba in partial fulfillment of the requirements
for the degree of Doctor of Philosophy (Science)

January, 1997

Contents

Chapter 1 Introduction 1

1.1 Background 1

1.2 Aim of present study 3

1.3 Organization of present thesis 5

Chapter 2 Theory 7

2.1 Experimental theory 7

2.1.1 Angle resolved ultraviolet photoemission spectroscopy 7

2.1.2 Polarization selection rules 14

2.2 Theory of the linear combination of atomic orbital method 16

2.2.1 Introduction 16

2.2.2 Simplified-linear combination of atomic orbital method 16

2.2.3 Selection of parameters 23

Chapter 3 Experiment 26

3.1 Spectrometer chamber 26

3.1.1 Vacuum system 26

3.1.2 Instruments 30

3.2 Sample preparation 32

3.2.1 Samples 32

3.2.2 Sample holder 33

3.2.3 Sample cleaning 33

3.2.4 Checking the surface cleanliness 36

3.2.5 The oxygen adsorption on Cu(110), Ni(110) and Ag(110) surface 37

3.3 Measurements 39

3.3.1 Light source 39

3.3.2 Angle-resolved ultraviolet photoemission spectroscopy measurements 39

3.3.3 Work-function measurements 40

Chapter 4 Clean and oxygen adsorbed Cu(110) surface 46
4.1 LEED observation and WF measurement 46
4.2 Angle-resolved photoemission study of clean and oxygen adsorbed Cu(110)surface 46
4.3 Simplified-LCAO calculation of Cu(110)/2x1-O surface 48

Chapter 5 Clean and oxygen adsorbed Ni(110) surface 67
5.1 LEED observation and WF measurement 67
5.2 Angle-resolved photoemission study of clean and oxygen adsorbed Ni(110) surface 67
5.3 Simplified-LCAO calculation of Ni(110)/2x1,3x1-O surface 68
5.4 High-exposed Ni(110)/2x1-O surface 71

Chapter 6 Clean and oxygen adsorbed Ag(110) surface 90
6.1 Ag(110)/nx1-O surface 90
6.1.1 LEED observations 90
6.1.2 Work functions 90
6.1.3 Oxygen coverage 91
6.1.4 Angle-resolved photoemission study of clean and Ag(110)/2x1-O surface 93
6.1.5 Simplified-LCAO calculation of Ag(110)/2x1-O surface 95
6.2 Ag(110)/1x2-O surface 114
6.2.1 LEED observations 114
6.2.2 Work functions 115
6.2.3 Oxygen coverage 115
6.2.4 Photoemission study of Ag(110)/1x2-O surface 115
6.2.5 Angle resolved photoemission study of Ag(110)/1x2-O surface 117
6.2.6 Other discussions 118
6.2.7 Ag(110)/1x2-O model and application for LCAO calculation 119

Chapter 7 Conclusion 139
7.1 Oxygen adsorbed Cu(110) surface 139
7.2 Oxygen adsorbed Ni(110) surface 139
7.3 Oxygen adsorbed Ag(110) surface 140

Appendix Phase diagram 141

Acknowledgments 142

References 143

Abstract

The electronic structure of the oxygen adsorbed Cu(110), Ni(110) and Ag(110) surfaces were investigated by Angle-Resolved Ultraviolet Photoelectron Spectroscopy. When these surfaces are exposed to the oxygen gas, the missing row structure, which consists of the one-dimensional oxygen-metal chains, is formed. The experiments were made for getting information on this oxygen-metal bonding in the present thesis. These surfaces are well known as catalysts, and studies of these catalyst surfaces are important for industry as well as for revealing a physical base of surface chemical reactions, such as the oxygen chemisorption. A tight-binding calculation (LCAO) assuming the missing row model was made to compare with the experimental results. It could reproduce the experiment qualitatively, and O-metal interactions were determined quantitatively for each system.

Several ARUPS studies on the Cu(110)/2x1-O surface have been reported, and the interpretations of the band symmetries are different. The present study, therefore, was made carefully, especially to reveal the band symmetries and the band ordering including the hybridization. Some of the oxygen induced bonding and anti-bonding band symmetries were confirmed. It was also confirmed experimentally that the O-p_y and O-p_z bands cross and hybridize. The LCAO calculation was made on the Cu(110)/2x1-O surface assuming the missing row model. It could satisfactorily reproduce the experimental dispersions of the oxygen induced two-dimensional energy bands and band crossing as well as symmetry characteristics.

ARUPS studies on the Ni(110)/2x1-O surface have been reported by two groups, but the dispersions of the oxygen induced bands reported by them are in disagreement. The Ni(110)/2x1-O surface has been studied by ARUPS and the

oxygen induced bonding band symmetries were confirmed. ARUPS study on the Ni(110)/3x1-O (2/3ML) surface was made for the first time. With oxygen exposure lager than 10 L, the high-exposed Ni(110)/2x1-O surface was found. The ARUPS, WF and XPS measurements on this surface indicate almost the same results as the low-exposed Ni(110)/2x1-O surface.

ARUPS studies on the Ag(110)/2x1-O surface have been reported by two groups. However, the band symmetries were not sufficiently distinguished in both studies. ARUPS study, therefore, was made and some of the oxygen induced bonding band symmetries were confirmed.

The LCAO calculations were also made on the oxygen adsorbed Ni(110) and Ag(110) surfaces, and it reproduced the experimental dispersions of the oxygen induced bands qualitatively.

The Ag(110)/1x2-O surface was newly found. It was confirmed that the Ag(110)/1x2-O surface is an oxygen induced reconstructed surface by UPS, WF, LEED and XPS measurements. We proposed a 1x2 missing row model, and calculated the energy bands assuming the 1x2 missing row models with various oxygen atom sites to compare with the experiments. However, at present some revisions may be necessary to reproduce the result more accurately.

Chapter 1 Introduction

1.1 Background

Adsorption of oxygen atoms on metal surfaces such as Cu, Ni, Ag, ... has been a fundamental issue of the surface science. These surfaces are well known as catalysts. For example, Cu(110) surface is a catalyst for the dehydrogenation of methanol CH_3OH to formaldehyde HCHO. Ni(110) surface is a catalyst for the dehydrogenation of ammonia NH_3. And Ag(110) surface is a catalyst for the epoxidation of ethylene C_2H_4 to ethylene oxide C_2H_4O. Studies of these catalyst surfaces are important for industry as well as for revealing a physical base of surface chemical reactions, such as the oxygen chemisorption. When the metal surfaces are exposed to the oxygen gas, the initial O-metal interaction proceeds along several sequential stages which can be generalized as follows [1-28]: the impinging O_2 molecules dissociate on the metal surfaces, and the O atoms get trapped in the chemisorption well. This chemisorption process is accompanied by the breaking of metal-metal surface bonds, and new O-metal bonds are created. As for the Cu(110) surface, the dissociated oxygen atom gets bound to Cu adatoms which are supplied from the step edge and diffuse on the surface. Finally a missing row structure is formed where every second <001> Cu row is missing. This is a reconstructed surface called Cu(110)/2x1-O. On the Cu(110), Ni(110) and Ag(110) surfaces, one-dimensional metal-oxygen chain compound like -O-metal-O-metal-...., is formed along the <001> direction. At small oxygen exposure the O-metal chains can move thermally on the surface, and at oxygen coverage of 1/2 monolayer (ML) they are saturated and reconstructed as the missing row surfaces. Interestingly at the initial oxygen exposure the Cu-O chains gather so that the interaction between them is attractive. On the other hand the Ag-O chains repel each other so that the interaction is repulsive. LEED study [2] on the O/Ag(110) surface shows results which are ascribed to their repulsive feature. As the oxygen coverage increases, the LEED pattern of the Ag(110)

surface changes successively from p(7×1) to p(6×1), p(5×1),... and finally p(2×1), where the notation like p(n×1) is abbreviated as just n×1 from now on. This is an attractive issue. Recently STM studies of the oxygen adsorbed surfaces have been performed [3-13] and n×1 chain-like structures are observed with the O coverage. The stable structures of the Cu(110)/2×1-O and Ag(110)/2×1-O surfaces were investigated by the first-principle energy band calculations [14]. The calculation shows that two Ag rows located below the Ag-O chain contract their interval, whereas the Cu rows do not. This may suggest the repulsive feature between the Ag-O chains, however, it is still an open question.

The oxygen chemisorption on the metals mentioned above has been studied by a number of different experimental techniques such as low-energy electron diffraction (LEED) [47-51], surface-extended X-ray absorption fine-structure spectroscopy (SEXAFS) [47-51], X-ray photoelectron diffraction (XPD) [41], electron-energy-loss spectroscopy (EELS) [49,56-60], high-resolution electron-energy-loss spectroscopy (HREELS) [61], photoemission spectroscopy (PES) [62-65], angle resolved ultraviolet photoelectron spectroscopy (ARUPS) [19,20,22,23,66,67], X-ray photoelectron spectroscopy (XPS) [65,68,69], inverse photoemission spectroscopy (IPS) [70-72], impact-collision ion-scattering spectroscopy (ICISS) [73], high-, medium-, and low-energy ion scattering (HEIS, MEIS, and LEIS) [74-79], thermal desorption spectroscopy (TDS) [80], scanning tunneling microscopy (STM) [3-10] and so on. We have mainly studied on the oxygen adsorbed Cu(110), Ni(110) and Ag(110) surfaces by ARUPS and XPS.

We found in the present study a new phase of the oxygen adsorbed Ag(110) surface: Ag(110)/1×2-O. For this surface we proposed a 1×2 missing row model where every second $<\bar{1}10>$ Ag row is missing. Similar reconstruction phenomena induced by adsorbates have been reported: H on Cu(110) [15], Ni(110) [16] and Ag(110) [17] surfaces. As for the oxygen adsorbed Ni(110) surface, it has been reported that the Ni-O chains grow along the $<\bar{1}10>$ direction at initial stage of the oxygen exposure and the oxygen atom is located on the threefold hollow site

[10]. These may suggest the possibility of the 1×2 missing row model. From the catalytic point of view, the oxidation of the ethylene to the carbon dioxide and water, also occurs simultaneously with the epoxidation on the Ag(110) surface. Concerning the selectivity of ethylene oxidation and epoxidation, it has been argued that the selectivity may be related to the subsurface oxygen located in the first substrate layer. Backs [18] has reported that the subsurface oxygen exists even at temperature over 423 K and desorbes at temperature over 723 K. It has been proposed that there exist two types of oxygen, strongly and weakly chemisorbed, the former corresponds to the oxygen atoms of O-Ag chains, and the latter corresponds to the oxygen atoms chemisorbed on an atop site supported by the subsurface oxygen. And the former and latter atoms may be related to the oxidation and epoxidation, respectively. The study of the Ag(110)/1×2-O surface might give any information on the origin of the selectivity of the ethylene epoxidation.

1.2 Aim of present study

The ARUPS studies on the Cu(110)/2×1-O surface have been reported by Didio et al. [19] and Courths et al. [20]. The dispersions of the oxygen induced bands of two groups are quantitatively almost in agreement with each other. However the interpretations of the band symmetries are different. Didio et al. reported that the band order at $\overline{\Gamma}$ is different from that of at $\overline{Y}$. If their assignment is correct, the bands should cross and hybridize halfway between $\overline{\Gamma}$ and $\overline{Y}$. The tight binding calculation on the Cu(110)/2×1-O surface assuming the missing- and buckled-row model has been reported by Tjeng et al. [21]. They concluded that the calculation assuming the buckled row model was in good agreement with the ARUPS results [19,20]. However the missing row model has now been confirmed by many surface science studies [1-28]. In the present thesis, ARUPS study on the Cu(110)/2×1-O surface was made carefully, especially to reveal the band symmetries and the band ordering including the hybridization. A tight binding

calculation (LCAO method) was made assuming the missing row model to obtain qualitatively the oxygen-metal interactions. The calculated energy bands could reproduce the present ARUPS results.

The ARUPS studies on the Ni(110)/2×1-O surface have been reported by Pollak et al. [22] and Komeda et al. [23]. However the dispersions of the oxygen induced bands reported by two groups are in disagreement. It might be ascribed to the difference of surface preparation. A full potential augmented plane wave (FLAPW) calculation on the Ni(110)/2×1-O surface assuming the seven-layer film has been reported by Weimert et al. [24]. It seems to agree with the result of the former, however only symmetric and antisymmetric bands with respect to the xy mirror plane were obtained so that the x, y and z band symmetries were not distinguished in this calculation. The ARUPS studies on the Ni(110)/3×1-O (1/3 ML) surface have been reported by Komeda et al. [23], whereas the ARUPS studies on the Ni(110)/3×1-O (2/3 ML) surface have not been reported. In the present thesis, ARUPS on the Ni(110)/2×1-O and 3×1-O (2/3 ML) surfaces were investigated. The tight binding calculation was made assuming the 2×1 and 3×1 missing row models. The ARUPS study on the newly found Ni(110)/2×1H-O surface was also performed.

The ARUPS studies on the Ag(110)/2×1-O surface have been reported by Prince et al. [25] and Tjeng et al. [26]. The dispersions of the oxygen induced bands of two groups are quantitatively almost in agreement with each other. However the band symmetries were not sufficiently distinguished in both studies. The tight binding calculation on the Ag(110)/2×1-O surface assuming the missing- and buckled-row models has been reported by Tjeng et al. [26]. They concluded that the calculation assuming the both models were consistent with the ARUPS results [25,26]. The ARUPS study on the Ag(110)/3×1-O surface has been reported by Prince et al. [27]. The similar dispersions as those of the

Ag(110)/2x1-O surface were observed. As for the strongly and weakly chemisorbed oxygen, the ARUPS study on the Ag(110)/c(2x2)-O surface has been reported by Segeth et al. [28]. They reported that the non-dispersing oxygen induced band at -3.1 eV at temperature between 300 and 400 K, and at -3.4 eV at above ~470 K were observed. They concluded that the bondings of the former and latter are weakly and strongly, respectively. In the present thesis, ARUPS study on the Ag(110)/2x1-O surface was made to assign band symmetries. The tight binding calculation was made assuming the 2x1 missing row models. The characterization of the newly found Ag(110)/1x2-O surface was performed by LEED, work function measurements, XPS and ARUPS. The structural model for the Ag(110)/1x2-O surface was proposed. The tight binding calculation was made assuming this proposed model and compared with the experiment. The issues in the present thesis are summarized in table 1-1 together with the previous studies.

1.3 Organization of present thesis

In **Chapter 2**, Theories of ARUPS and simplified-LCAO method is presented briefly. In **Chapter 3**, the experimental equipments, the preparation and cleanliness checking of each sample, and the measuring geometries are presented. In **Chapter 4,5,6**, experimental information and discussions on the Cu(110), Ni(110), and Ag(110) surfaces are described, respectively. In these chapters LEED, WF and ARUPS information and discussions on each system are described at first. And the two dimensional energy bands are simulated by LCAO calculations. In addition the characterization and calculations of the Ag(110)/1x2-O surface were described in **Chapter 6**. **Chapter 7** is the conclusion.

Table 1-1 : List of system, previous studies and new findings in the present thesis.

System	Present study	Previous study	New findings in the present thesis
Cu(110)/2x1-O	LEED, WF	ARUPS [20,21]	Observation of O-p_y and p_z band crossing and hybridization
	ARUPS, LCAO	Calculation [22]	Reproduction of the experimental energy bands by LCAO
			Determination of O-Cu interactions
Ni(110)/2x1-O	LEED, WF	ARUPS [23,24]	Confirming of band ordering with symmetries on 2x1-O
3x1-O (2/3 ML)	ARUPS, LCAO	Calculation [25]	First measurement of 3x1-O (2/3 ML)
			Reproduction of 3x1-O using O-O interaction by LCAO
2x1H-O	LEED, WF, XPS, ARUPS		First measurement of 2x1H-O
Ag(110)/2x1-O	LEED, WF	ARUPS [26,27]	Confirming of band ordering with symmetries
	ARUPS, LCAO	Calculation [27]	Reproduction of the experimental energy bands by LCAO
1x2-O	LEED, WF,XPS		First observation of 1x2-O phase
	ARUPS, LCAO		Characterization of band to be O2*p* character
			Proposal of 1x2-O structural model

Chapter 2 Theory

2.1 Experimental theory

2.1.1 Angle resolved ultraviolet photoemission spectroscopy

When a vacuum ultraviolet light (VUV:hν=10~50eV) is irradiated to a material, photoelectrons are emitted from it by the photoelectric effect. These photoelectrons have information on the surface electronic structure due to its short mean free path. Processes of photoelectron emission are represented in three stages below.

(a) Photoelectron excitation in a crystal

(b) Transfer of the excited electron to the crystal surface

(c) Electron emission from the crystal surface to a vacuum

(a) Photoelectron excitation in a crystal

An electron in an initial state with energy $E_i(\vec{k}_i)$ is excited to a final state with energy $E_f(\vec{k}_f)$ by photon $h\nu$, where $\vec{k}_{i,f}$ are wavevectors and $E_{i,f}$ are referred to the Fermi energy. Then an energy conservation of the photoexcitation process gives,

$$E_f = E_i + h\nu \quad . \tag{2-1}$$

The transition probability per unit time W is given by the Fermi's golden rule,

$$W \propto \left|\vec{A}_0\right|^2 |M_{fi}|^2 \delta(E_f - E_i - h\nu) \quad , \tag{2-2}$$

where M_{fi} is a transition matrix element which is written as :

$$M_{fi} = \int \phi_f^* \exp(i \cdot \vec{k}_{h\nu} \cdot \vec{r}) \cdot \hat{A} \cdot \vec{\nabla} \cdot \phi_i \cdot d\vec{r} \quad , \tag{2-3}$$

where ϕ_i, ϕ_f are wave functions in the initial and final states, respectively and $\hat{A} = \vec{A}_0 / \left|\vec{A}_0\right|$, $\vec{A}_0$: vector potential.

When hν=50eV(VUV), $\left|\vec{k}_{h\nu}\right|$ is about 0.025 Å^{-1}. An integrating effective radius in equation (2-3) corresponds to Bohr radius: $|\vec{r}|$≈0.53 Å. Then the term of $\exp(i \cdot \vec{k}_{h\nu} \cdot \vec{r})$ can be approximated to 1. This is called the dipole approximation. So that equation (2-3) becomes,

$$M_{fi} = \int \phi_f^* \cdot \hat{A} \cdot \vec{\nabla} \cdot \phi_i \cdot d\vec{r} \quad . \tag{2-4}$$

Wave functions in the initial and final states have the Bloch form in the crystal,

$$\phi_n \propto \exp(i \cdot \vec{k}_n \cdot \vec{r}) \cdot u_n(\vec{k}_n, \vec{r}) \quad ; n = i, f \quad , \tag{2-5}$$

where $u_n(\vec{r})$ has a periodicity of a crystal lattice with $u_n(\vec{r}) = u_n(\vec{r} + \vec{T})$. Where $\vec{T}$ is a crystal translation vector. So that equation (2-4) becomes,

$$M_{fi} = \int \exp\{-i \cdot \vec{k}_f \cdot \vec{r}\} \cdot u_f^*(\vec{k}_f, \vec{r}) \cdot \hat{A} \cdot \vec{\nabla} \cdot \exp(i \cdot \vec{k}_i \cdot \vec{r}) \cdot u_i(\vec{k}_i, \vec{r}) \cdot d\vec{r} \quad . \tag{2-6}$$

Here because it has the periodicity of the crystal, M_{fi} is required that,

$$M_{fi}(\vec{r}) = M_{fi}(\vec{r} + \vec{T}) \quad . \tag{2-7}$$

This means that,

$$\exp\{-i(\vec{k}_f - \vec{k}_i) \cdot \vec{T}\} = 1 \tag{2-8}$$

is required. So,

$$\vec{k}_f = \vec{k}_i + \vec{G} \quad . \quad (\vec{G} \text{ is a reciprocal lattice vector}) \tag{2-9}$$

is required. When it is written in a reduced zone scheme, that equation (2-9) becomes,

$$\vec{k}_f = \vec{k}_i \quad . \tag{2-10}$$

Equation (2-10) means a momentum conservation of photoexcitation. So this photoexcitation is a direct transition (see Fig.2.1).

(b) Transfer of the excited electron to the crystal surface

Not only photoelectrons around the crystal surface but also those in the bulk are excited because a mean penetration depth in the crystal of the photon which is used for the PES (photoemission spectroscopy) studies is of the order of μm. PES is, however, extremely useful to investigate surface electronic structures due to a very short mean free path of excited electrons.

When electrons excited in the crystal move to the surface, some of them do not suffer any scattering, some are scattered elastically and some are scattered inelastically; mainly to excite plasmons and phonons. The mean free path of excited electrons (λ) as a function of electron energy is plotted in Fig.2.2 [29-31], which does not depend so much on a material of the crystal. This is called a

universal curve. λ is about 5 Å under optimum energy range (20~100eV) and this corresponds to a length of a few atomic monolayers. Information of the surface electronic structure are selectively observed by choosing these energies as a pumping source. Photoelectrons scattered not only elastically but inelastically are observed simultaneously. But it may be easy to distinguish signals of the former from these of the latter which are observed as a background like a gentle slope. In this study, HeI (21.22 eV), HeII (40.8 eV) and NeI (16.85 and 16.65 eV) are used as a pumping source. Thus we can say that a surface sensitivity of this method (UPS) is very good.

(c) Electron emission from the crystal surface to a vacuum

The work function ϕ of the uniform surface of a metal is defined as the difference in potential energy of an electron between the vacuum level and the Fermi level, corresponding to an energy that is necessary to transfer the electron from the surface to the vacuum. The kinetic energy of the electron in the crystal $E_f(\vec{k}_f)$ and in the vacuum $E(\vec{k})$ have a relation that (see Fig.2.3)

$$E(\vec{k}) = E_f(\vec{k}_f) - \phi \quad . \tag{2-11}$$

In addition to the energy conservation given by equation (2-11), the parallel component to the surface of the momentum is conserved, whereas a perpendicular component to the surface is not conserved in general, when the photoelectron is transferred from the crystal to the vacuum (see Fig.2.4):

$$\vec{k}_{//} = \vec{k}_{f//} + \vec{g}_{//} \quad , \tag{2-12}$$

where $\vec{g}_{//}$ is a reciprocal surface lattice vector.

Thus processes of photoelectron emission are represented in these three stages. Here the initial state of electron in the crystal (E_i, $\vec{k}_i$) and the state in the vacuum (E, $\vec{k}$) have a relation that (in a reduced zone scheme),

$$E_i(\vec{k}_i) = E(\vec{k}) + \phi - h\nu \quad , \tag{2-13}$$

$$\vec{k}_{i//} = \vec{k}_{//} \quad . \tag{2-14}$$

The electron in the vacuum is considered as a free electron :

$$\left|E(\vec{k})\right| = \frac{\hbar^2 \vec{k}^2}{2m_e} \quad , \tag{2-15}$$

where m_e is a mass of the electron. So $\vec{k}$ is, by equation (2-13),

$$k = \frac{\sqrt{2m_e}}{\hbar}\sqrt{h\nu - \phi + E_i(\vec{k}_i)} \quad , \tag{2-16}$$

where all energy terms are the differences between them and the Fermi level. When an emission angle in the collection plane measured from the surface normal is θ_e as in Fig.2.4, that equation (2-16) becomes, by geometrically relation,

$$k_{i//} = k_{//} = \frac{\sqrt{2m_e}}{\hbar}\sqrt{h\nu - \phi + E_i(\vec{k}_i)} \cdot \sin\theta_e \quad . \tag{2-17}$$

This is an equation that connects E_i with $k_{i//}$ of the initial state electron in the crystal. And the other terms (m_e, $\hbar$,$h\nu$, ϕ, θ_e) are the known physical constants and the measurement values.

So it is possible to get a two-dimensional energy band when spectra are measured by the angle resolved analyzer.

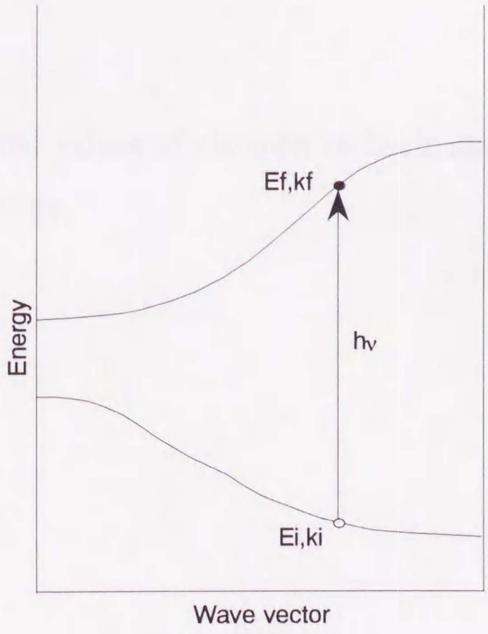

Figure 2-1. Schematic diagram of the direct transition. This means a momentum conservation of photoexcitation.

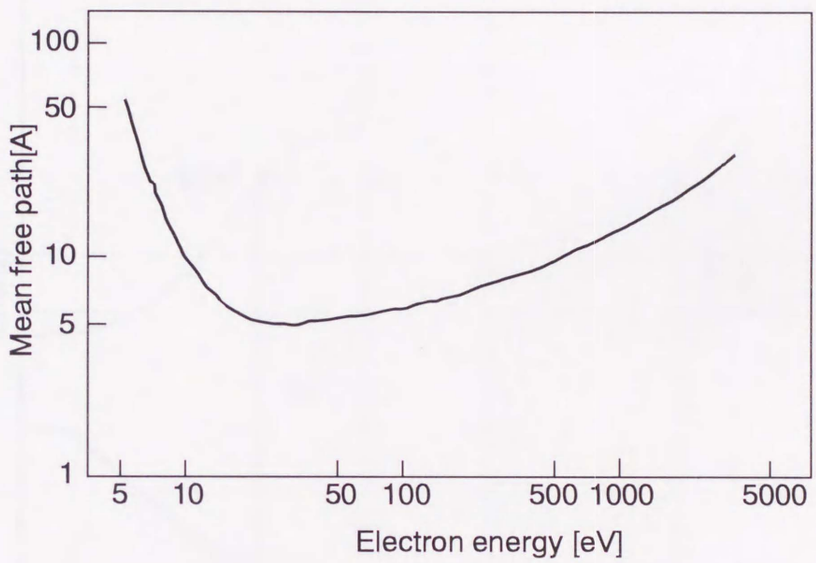

Figure 2-2. Experimental values of electron inelastic mean free path lengths as a function of electron energy.

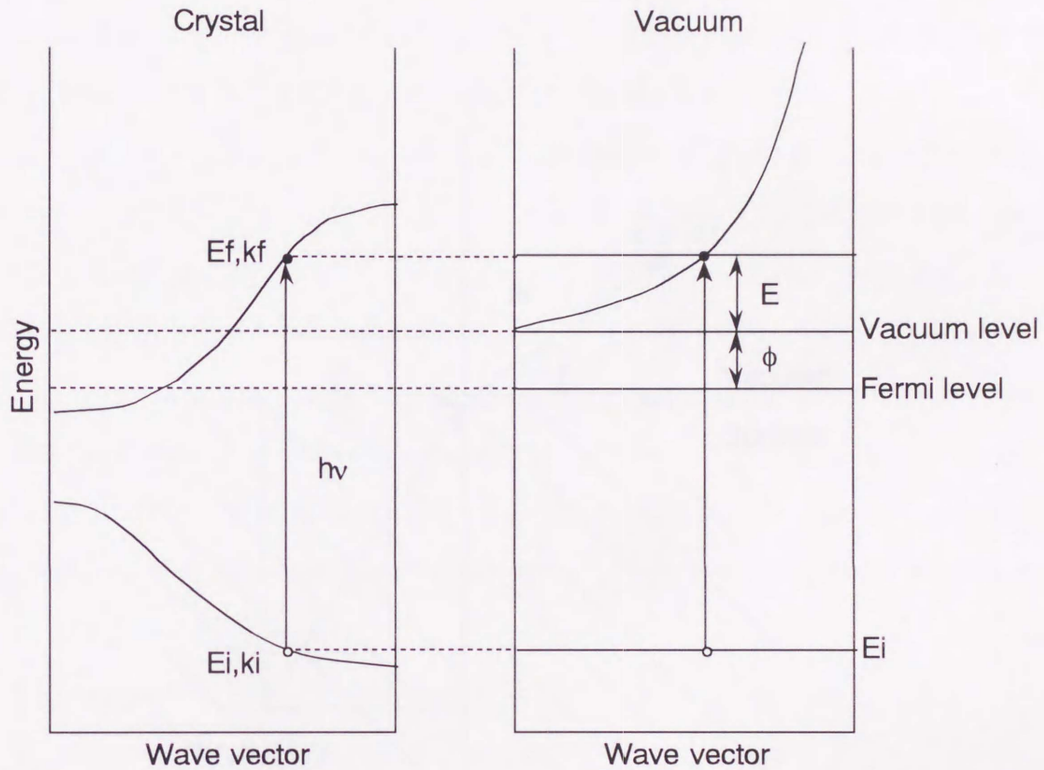

Figure 2-3. Energy diagram of photoexcited electron in the crystal and the vacuum. ϕ is the work function.

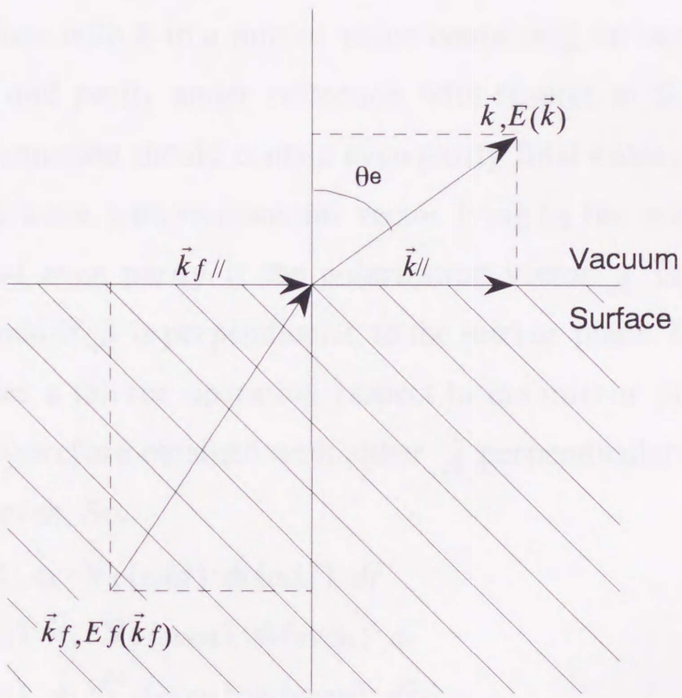

Figure 2-4. Electron emission from the crystal surface to the vacuum. The momentum parallel to the surface is conserved.

2.1.2 Polarization selection rules

Electron wave function in a crystal have extra quantum numbers which are related to the crystal symmetry operations. Those symmetries can be assigned by using polarization selection rules. The direct transitions are described by the transition matrix element (see equation (2-4)). For nonvanishing matrix element, the direct product of the representation of the initial state and the final state contains or is equal to the representation of the dipole operator.

The wave functions with k in a mirror plane containing surface normal should be either even or odd parity under reflection with respect to the mirror plane. The mirror plane emission should contain even parity final states since the emitted electron is a plane wave with momentum vector lying in the mirror plane. The operator $\hat{A}\cdot\vec{\nabla}$ is of even parity if the polarization vector $\hat{A}$ is parallel to the mirror plane and odd if $\hat{A}$ is perpendicular to the mirror plane. Because M_{fi} has to be constant under a mirror operation respect to the mirror plane, a non-zero matrix element is therefore obtained with either $\hat{A}$ perpendicular and ϕ_i odd, or $\hat{A}$ parallel and ϕ_i even. So,

$$\begin{aligned} M_{fi} = & \int \phi_f^*(even)\cdot \hat{A}_x \cdot \vec{\nabla}_x(odd)\cdot \phi_i(odd)\cdot d\vec{r} \\ & + \int \phi_f^*(even)\cdot \hat{A}_y \cdot \vec{\nabla}_y(even)\cdot \phi_i(even)\cdot d\vec{r} \\ & + \int \phi_f^*(even)\cdot \hat{A}_z \cdot \vec{\nabla}_z(even)\cdot \phi_i(even)\cdot d\vec{r} \quad . \end{aligned} \tag{2-18}$$

expresses the permitted transition. Therefore if the polarization vector was known, the initial state parity could be determined. In this experiment, the initial state parities were measured using a linearly polarized light as a light source (see Fig.2-5).

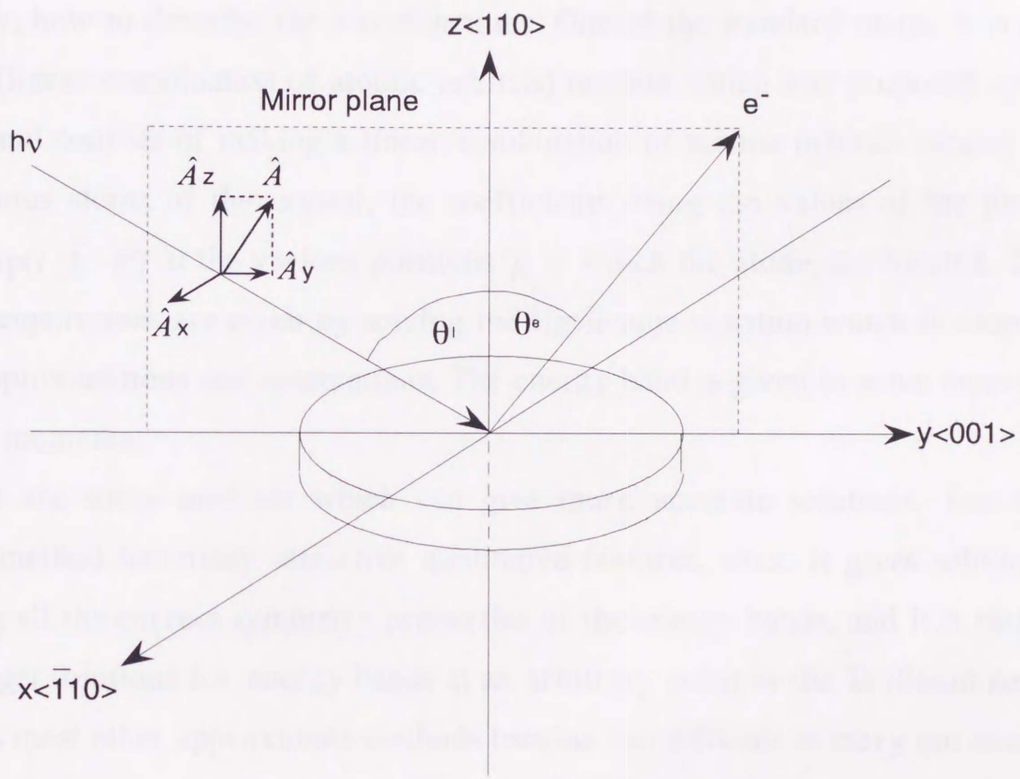

Figure 2-5. Mirror plane and the components of linearly polarized light.

2.2 Theory of the linear combination of atomic orbital method

2.2.1 Introduction

There were many attempts to calculate an electronic structure in the crystal, i.e., to solve the periodic potential problems in the theory of the electronic motions in the crystal. Some assumptions are necessary to solve it; at first, one electron approximation and to adopt a spherically symmetrical potential. And secondly, how to describe the wavefunctions. One of the standard methods is the LCAO (linear combination of atomic orbitals) method which was proposed by F. Bloch, and consists of making a linear combination of atomic orbitals located on the various atoms of the crystal, the coefficients being the values of the plane wave $\exp(i \cdot \vec{k} \cdot \vec{R})$ at the various positions $\vec{R}$ at which the atoms are located. The energy eigenvalues are given by solving the eigenvalue equation which is adopted these approximations and assumptions. The energy band is given to solve them for various momenta.

There are some methods which can give more accurate solutions. But the LCAO method has many attractive qualitative features, since it gives solutions showing all the correct symmetry properties of the energy bands, and it is rather easy to get solutions for energy bands at an arbitrary point in the Brillouin zone, whereas most other approximate methods become too difficult to carry out except at certain symmetry points of the Brillouin zone. The LCAO method is useful, not as a primary method of accurate calculation, but rather as an interpolation method.

2.2.2 Simplified-linear combination of atomic orbital method

There are many matrix components to get solutions of LCAO calculation. So a simplified-LCAO method in which there is an improvement such that some matrix components are neglected and some are treated as parameters with a little reduction of the good features of LCAO method, is adopted.

The solution of the Schrödinger equation for a periodic potential must be of

special form: the Bloch functions (Bloch sums). Here we can construct Bloch sums from atomic functions ϕ_m which are orthogonal to each other.

$$\Psi_m = \frac{1}{\sqrt{N}} \sum_{R_i} \exp(i \cdot \vec{k} \cdot \vec{R}_i)\, \phi_m(\vec{r} - \vec{R}_i) \quad , \tag{2-19}$$

where $\vec{R}_i$ is the vector position of the atom on which the orbital is located, and N is number of unit cells in the repeating region; the normalization is over this repeating region, so $N^{-1/2}$ is the normalization factor. If H is the Hamiltonian operator, the matrix component of energy between two such Bloch sums is

$$H_{mn} = \langle \Psi_m | H | \Psi_n \rangle$$

$$= \frac{1}{N} \sum_{\vec{R}_i, \vec{R}_j} \exp\left\{ i \cdot \vec{k} \cdot (\vec{R}_j - \vec{R}_i) \right\} \langle \phi_m(\vec{r} - \vec{R}_i) | H | \phi_n(\vec{r} - \vec{R}_j) \rangle \quad . \tag{2-20}$$

The sum is over the N unit cells and one of the summations in the double sum of (2-20) can be eliminated, for it amounts to multiplying the single summation by N, which cancels the factor N^{-1}. So that (2-20) becomes,

$$H_{mn} = \sum_{R_j} \exp\left\{ i \cdot \vec{k} \cdot (\vec{R}_j - \vec{R}_i) \right\} \langle \phi_m(\vec{r} - \vec{R}_i) | H | \phi_n(\vec{r} - \vec{R}_j) \rangle \quad . \tag{2-22}$$

When we assume the one electron approximation the Hamiltonian H is described as

$$H = \sum_{R_V} \left\{ -\frac{\hbar^2 \cdot \vec{\nabla}^2}{2m_e} + V(\vec{r} - \vec{R}_V) \right\}, \tag{4}$$

where $V(\vec{r} - \vec{R}_V)$ is a spherically symmetrical potential well located at the atom at position $\vec{R}_V$ of the crystal. So that (2-21) becomes,

$$H_{mn} = \sum_{R_j} \sum_{R_V} \exp\left\{ i \cdot \vec{k} \cdot (\vec{R}_j - \vec{R}_i) \right\}$$

$$\times \left\{ \left\langle \phi_m(\vec{r} - \vec{R}_i) \left| -\frac{\hbar^2 \cdot \vec{\nabla}^2}{2m_e} \right| \phi_n(\vec{r} - \vec{R}_j) \right\rangle + \left\langle \phi_m(\vec{r} - \vec{R}_i) | V(\vec{r} - \vec{R}_V) | \phi_n(\vec{r} - \vec{R}_j) \right\rangle \right\} \quad . \tag{2-23}$$

The first term is the overlap integrals which are negligibly small than the

second term in general, so these are eliminated in Simplified-LCAO method (concrete examples: ref.[21] and ref.[26] for Cui and Ag, respectively).

The second term is a linear combination of integrals of a product of an atomic function $\phi_m(\vec{r} - \vec{R}_i)$ located on the atom at position $\vec{R}_i$, another atomic function $\phi_n(\vec{r} - \vec{R}_j)$ on the atom at $\vec{R}_j$, and a spherical potential function located on the atom at $\vec{R}_V$. In other words, we need considering the three centers of integral. This is called the three-center integrals. So the matrix components H_{mn} consist of the linear combinations of integrals which are listed below:

$\vec{R}_V = \vec{R}_i = \vec{R}_j$: one-center integrals

$\vec{R}_V = \vec{R}_i \neq \vec{R}_j$: two-center integrals

$\vec{R}_V \neq \vec{R}_i \neq \vec{R}_j$: three-center integrals

It is extremely difficult to calculate all these integrals because there are countless number of integrals, combined in such complicated ways. For simplification, only integrals of atomic function located on the same atom, between the atom and the nearest neighbor atoms, and between the atom and the second nearest neighbor atoms, are calculated. And we assume that the other integrals are eliminated. Some of the atomic functions are eliminated, for example; the core level electron orbitals which do not take part in the chemical bondings so much. Furthermore, we assume that three-center integrals are eliminated because they are small than one-center and two-center integrals in general. This is the two-center approximation.

The atomic function ϕ in polar coordinates (r, θ, φ) is,

$$\phi_{nlm}(\vec{r}) = R_{n,l}(r) \cdot Y_{l,m}(\theta, \varphi) \quad , \qquad (2\text{-}24)$$

where (l, m, n) are the quantum numbers, $R_{n,l}(r)$ is the radial distribution function and $Y_{l,m}(\theta, \varphi)$ is the spherical surface harmonics. We now consider d, s and p atomic orbitals for the transition metals and $2p$ atomic orbitals for the oxygen. The concrete forms of the spherical surface harmonics of s, p and d orbitals are:

$$s \text{ orbital} : Y_{0,0}(\theta, \varphi) = \frac{1}{\sqrt{4\pi}}$$

(l=0)

p orbital : $Y_{1,0}(\theta,\varphi) = \sqrt{3/4\pi} \cdot \cos\theta$

(l=1) $Y_{1,\pm1}(\theta,\varphi) = \mp\sqrt{3/8\pi} \cdot \sin\theta \cdot \exp(\pm i \cdot \varphi)$

d orbital : $Y_{2,0}(\theta,\varphi) = \sqrt{5/16\pi} \cdot (3\cos^2\theta - 1)$

(l=2) $Y_{2,\pm1}(\theta,\varphi) = \mp\sqrt{15/8\pi} \cdot \sin\theta \cdot \cos\theta \cdot \exp(\pm i \cdot \varphi)$

$Y_{2,\pm2}(\theta,\varphi) = \mp\sqrt{15/32\pi} \cdot \sin^2\theta \cdot \exp(\pm 2i \cdot \varphi)$

Here the atomic function of s orbital is,

$$\phi_{n00}(\vec{r}) = \frac{1}{\sqrt{4\pi}} \cdot R_{n,0}(r) \quad . \tag{2-25}$$

On the other hand, it is convenient for the p and d orbitals to make the atomic functions which are linear combinations of the spherical surface harmonics, to have an angle dependence being proportional to a length from the center of the atom, and to be along one of the three Cartesian coordinates. For example, we make such an atomic function of p orbital.

Relations between the three Cartesian and the polar coordinates are,

$$x = r\sin\theta\cos\varphi \quad ;$$

$$y = r\sin\theta\sin\varphi \quad ;$$

$$z = r\cos\theta \quad . \tag{2-26}$$

A linear combination of $Y_{1,-1}$ and $Y_{1,1}$ becomes,

$$\begin{aligned}\frac{1}{\sqrt{2}}(Y_{1,-1} - Y_{1,1}) &= \frac{1}{\sqrt{2}}\sqrt{3/8\pi} \cdot \sin\theta \cdot \{\exp(-i\cdot\varphi) + \exp(i\cdot\varphi)\} \\ &= \frac{1}{2}\sqrt{3/4\pi} \cdot \sin\theta \cdot \{\cos\varphi - i\cdot\sin\varphi + \cos\varphi + i\cdot\sin\varphi\} \\ &= \sqrt{3/4\pi} \cdot \sin\theta \cdot \cos\varphi \\ &= \sqrt{3/4\pi} \cdot r \cdot \sin\theta \cdot \cos\varphi / r \\ &= \sqrt{3/4\pi} \cdot x / r \quad .\end{aligned} \tag{2-27}$$

In the same way,

$$\begin{aligned}\frac{i}{\sqrt{2}}(Y_{1,-1} + Y_{1,1}) &= \frac{i}{\sqrt{2}}\sqrt{3/8\pi} \cdot \sin\theta \cdot \{\exp(-i\cdot\varphi) - \exp(i\cdot\varphi)\} \\ &= \sqrt{3/4\pi} \cdot \sin\theta \cdot \sin\varphi \\ &= \sqrt{3/4\pi} \cdot y / r \quad .\end{aligned} \tag{2-28}$$

And,

$$Y_{1,0}(\theta,\varphi) = \sqrt{3/4\pi}\cdot\cos\theta$$
$$= \sqrt{3/4\pi}\cdot r\cdot\cos\theta/r$$
$$= \sqrt{3/4\pi}\cdot z/r \quad . \tag{2-29}$$

Thus we can make an atomic function of p orbital to multiply the equations (2-27, 28 and 29) by the radial distribution function. In the same way, we can make functions of d orbital. The atomic functions of s, p and d orbitals (ϕ_k ; an index k denotes that which orbital is) are,

$$\phi_s = \frac{1}{\sqrt{4\pi}}\cdot R_{n,0}(r) \quad ;$$
$$\phi_x = \sqrt{3/4\pi}\cdot R_{n,1}(r)\cdot x/r \quad ;$$
$$\phi_y = \sqrt{3/4\pi}\cdot R_{n,1}(r)\cdot y/r \quad ;$$
$$\phi_z = \sqrt{3/4\pi}\cdot R_{n,1}(r)\cdot z/r \quad ;$$
$$\phi_{xy} = \sqrt{15/4\pi}\cdot R_{n,2}(r)\cdot xy/r^2 \quad ;$$
$$\phi_{yz} = \sqrt{15/4\pi}\cdot R_{n,2}(r)\cdot yz/r^2 \quad ;$$
$$\phi_{zx} = \sqrt{15/4\pi}\cdot R_{n,2}(r)\cdot zx/r^2 \quad ;$$
$$\phi_{x^2-y^2} = \sqrt{15/4\pi}\cdot R_{n,2}(r)\cdot\left(x^2-y^2\right)/2r^2 \quad ;$$
$$\phi_{3z^2-r^2} = \sqrt{15/4\pi}\cdot R_{n,2}(r)\cdot\left(3z^2-r^2\right)/2\sqrt{3}r^2 \quad . \tag{2-30}$$

The indices correspond as below:

$k = s$	: s orbital
$k = x, y, z$	: p orbital
$k = xy, yz, zx, x^2\text{-}y^2, 3z^2\text{-}r^2$	: d orbital

This is concerning to the radical distributions and a symmetry of atomic functions. In this paper, these atomic functions are adopted.

Now $\vec{R}_i = \vec{R}_V$ (the two-center approximation); as a result, the second term of (2-23) becomes,

$$\left\langle \phi_m(\vec{r}-\vec{R}_i)\middle|V(\vec{r}-\vec{R}_i)\middle|\phi_n(\vec{r}-\vec{R}_j)\right\rangle \equiv E_{mn}(l,m,n) \quad . \tag{2-31}$$

The $E_{mn}(l,m,n)$ is given by Slater et al. [32] and showed in table 2-1. For example, let $E_{x,xy}(l,m,n)$ be an integral in which the function ϕ_m is a p_x-like function; ϕ_n, a d function with symmetry properties like xy. This particular function can be written approximately in terms of two integrals: that between a pσ orbital on the first atom and a dσ orbital on the second; and that between a pπ

on the first and a dπ on the second. Let the first of these be symbolized by pdσ and the second by pdπ.

In the Simplified-LCAO, ssσ, spσ, ppσ, ppπ, sdσ, pdσ, pdπ, ddσ, ddπ and ddδ in table 2-1 are treated as parameters. And each on-site energy of orbital:

$$E_m = \left\langle \phi_m(\vec{r} - \vec{R}_i) | H | \phi_m(\vec{r} - \vec{R}_i) \right\rangle \quad , \tag{2-32}$$

is also treated as a parameter. As far as the p orbitals, the forms of p_x, p_y and p_z orbitals are equal to each other. So they are written as just Ep. As far as d orbitals, they are divided in two groups by their forms.

Now we can calculate the whole H_{mn} which give energy eigenvalues. The energy distribution is given by calculating the eigenvalues for each wave vector.

Table 2-1 : Energy integrals for crystal in terms of two-center integrals [32], where $(l,m,n)=\vec{R}_j - \vec{R}_i$.

Es,s	$= (ss\sigma)$
Es,x	$= l\,(sp\sigma)$
Ex,x	$= l^2\,(pp\sigma)+(1-l^2)\,(pp\pi)$
Ex,y	$= lm\,(pp\sigma)-lm\,(pp\pi)$
Ex,z	$= ln\,(pp\sigma)-ln\,(pp\pi)$
Es,xy	$= 3^{1/2}lm(sd\sigma)$
Es,x^2-y^2	$= 1/2\cdot3^{1/2}(l^2-m^2)\,(sd\sigma)$
Es,$3z^2$-r^2	$= [n^2-1/2(l^2+m^2)]\,(sd\sigma)$
Ex,xy	$= 3^{1/2}l^2m\,(pd\sigma)+m\,(1-2l^2)\,(pd\pi)$
Ex,yz	$= 3^{1/2}lmn\,(pd\sigma)-2lmn\,(pd\pi)$
Ex,zx	$= 3^{1/2}l^2n\,(pd\sigma)+n\,(1-2l^2)\,(pd\pi)$
Ex,x^2-y^2	$= 1/2\cdot3^{1/2}l\,(l^2-m^2)\,(pd\sigma)+l\,(1-l^2+m^2)\,(pd\pi)$
Ey,x^2-y^2	$= 1/2\cdot3^{1/2}m(l^2-m^2)\,(pd\sigma)-m(1+l^2-m^2)\,(pd\pi)$
Ez,x^2-y^2	$= 1/2\cdot3^{1/2}n(l^2-m^2)\,(pd\sigma)-n(l^2-m^2)\,(pd\pi)$
Ex,$3z^2$-r^2	$= l[n^2-1/2(l^2+m^2)]\,(pd\sigma)-3^{1/2}ln^2\,(pd\pi)$
Ey,$3z^2$-r^2	$= m[n^2-1/2(l^2+m^2)]\,(pd\sigma)-3^{1/2}mn^2\,(pd\pi)$
Ez,$3z^2$-r^2	$= n[n^2-1/2(l^2+m^2)]\,(pd\sigma)+3^{1/2}n(l^2+m^2)\,(pd\pi)$
Exy,xy	$= 3l^2m^2\,(dd\sigma)+(l^2+m^2-4l^2m^2)\,(dd\pi)+(n^2+l^2m^2)\,(dd\delta)$
Exy,yz	$= 3lm^2n\,(dd\sigma)+ln\,(1-4m^2)\,(dd\pi)+ln\,(m^2-1)\,(dd\delta)$
Exy,zx	$= 3l^2mn\,(dd\sigma)+mn\,(1-4l^2)\,(dd\pi)+mn\,(l^2-1)\,(dd\delta)$
Exy,x^2-y^2	$= 3/2lm\,(l^2-m^2)\,(dd\sigma)+2lm\,(m^2-l^2)\,(dd\pi)+1/2lm\,(l^2-m^2)\,(dd\delta)$
Eyz,x^2-y^2	$= 3/2mn\,(l^2-m^2)\,(dd\sigma)-mn[1+2(l^2-m^2)]\,(dd\pi)+mn[1+1/2(l^2-m^2)\,(dd\delta)$
Ezx,x^2-y^2	$= 3/2nl\,(l^2-m^2)\,(dd\sigma)+nl[1-2(l^2-m^2)]\,(dd\pi)-nl[1-1/2(l^2-m^2)]\,(dd\delta)$
Exy,$3z^2$-r^2	$= 3^{1/2}lm[n^2-1/2(l^2+m^2)]\,(dd\sigma)-3^{1/2}\cdot2lmn^2\,(dd\pi)+1/2\cdot3^{1/2}lm\,(1+n^2)\,(dd\delta)$
Eyz,$3z^2$-r^2	$= 3^{1/2}mn[n^2-1/2(l^2+m^2)]\,(dd\sigma)+3^{1/2}mn(l^2+m^2-n^2)\,(dd\pi)-1/2\cdot3^{1/2}mn\,(l^2+m^2)\,(dd\delta)$
Ezx,$3z^2$-r^2	$= 3^{1/2}ln[n^2-1/2(l^2+m^2)\,]\,(dd\sigma)+3^{1/2}ln\,(l^2+m^2-n^2)\,(dd\pi)-1/2\cdot3^{1/2}ln(l^2+m^2)\,(dd\delta)$
x^2-y^2,x^2-y^2	$= 3/4(l^2-m^2)^2(dd\sigma)+[l^2+m^2-(l^2-m^2)^2]\,(dd\pi)+[n^2+1/4(l^2-m^2)^2]\,(dd\delta)$
x^2-y^2,$3z^2$-r^2	$= 1/2\cdot3^{1/2}(l^2-m^2)[n^2-1/2(l^2+m^2)](dd\sigma)$ $+3^{1/2}n^2(m^2-l^2)(dd\pi)+1/4\cdot3^{1/2}(1+n^2)\,(l^2-m^2)\,(dd\delta)$
E$3z^2$-r^2,$3z^2$-r^2	$= [n^2-1/2(l^2+m^2)]^2\,(dd\sigma)+3n^2(l^2+m^2)\,(dd\pi)+3/4(l^2+m^2)^{\,2}(dd\delta)$

2.2.3 Selection of parameters

The 2x1 missing-row model adopted for the Simplified-LCAO calculation are shown in figure 2-6. The oxygen atoms are shown by filled circles. Marks ; t, 1 and 2 denote the topmost, first and second substrate (Cu, Ni or Ag) layer, respectively. A square line denotes an unit cell for the 2x1-O surface.

Matrices contain elements of the oxygen atoms, the topmost layer and the substrate layers; down to the 16th substrate layers for Cu, the 20th for Ni and the 24th for Ag. And a matrix component of oxygen consists of *2p* electron orbitals (*x, y, z*) and matrix components of copper, nickel and silver consist of ; *3d*(*xy, yz, zx,* x^2-y^2, $3z^2$-r^2), *4s* and *4p* (*x, y, z*) for Cu and Ni, and *4d*, *5p* and *5s* for Ag. The oxygen *2s* electron is assumed not to contribute to a chemical bondings because it is in the core level at energy -24 eV.

Matrices contain (a) integrals between the substrate atoms, (b) integrals between the oxygen and substrate atoms, and (c) the on-site energies on the oxygen and substrate atoms. As far as (a) and (b), only interactions between the nearest and next nearest neighbors are adopted, and these are described as the two-center integrals. And (c) are described as the one-center integrals. Table 2-2 shows parameters above. It was assumed that the oxygen atom lies in the topmost layer plane and there is no surface relaxation. Because structural unstableness of the substrate atoms around the surface make their energies to be higher than that of bulk, another parameter, surface-shift (ss), is added to the on-site energies of the atoms on the topmost layer and the first substrate layer.

Table 2-2 : Notation of one-center and two-center integrals. (a) Metal-metal two-center integrals. (b) Oxygen-metal two-center integrals. (c) One-center integrals (On-site energy). The notation (nn) and (nnn) denotes the nearest neighbor and second nearest neighbor, respectively.

(a) metal-metal interaction

ssσ(nn)	,	ssσ(nnn)
spσ(nn)	,	spσ(nnn)
ppσ(nn)	,	ppσ(nnn)
ppπ(nn)	,	ppπ(nnn)
sdσ(nn)	,	sdσ(nnn)
pdσ(nn)	,	pdσ(nnn)
pdπ(nn)	,	pdπ(nnn)
ddσ(nn)	,	ddσ(nnn)
ddπ(nn)	,	ddπ(nnn)
ddδ(nn)	,	ddδ(nnn)

(b) oxygen-metal interaction

sPσ(nn)	,	sPσ(nnn)
pPσ(nn)	,	pPσ(nnn)
pPπ(nn)	,	pPπ(nnn)
Pdσ(nn)	,	Pdσ(nnn)
Pdπ(nn)	,	Pdπ(nnn)

(c) On-site energy of metal and oxygen

E_{Op}	:	O2p orbital
Es	:	Cu4s, Ni4s, Ag5s orbital
Ep	:	Cu4p, Ni4p, Ag5p orbital
Ed1	:	Cu 3d, Ni 3d, Ag 4d orbital (xy, yz, zx)
Ed2	:	Cu 3d, Ni 3d, Ag 4d orbital (x^2-y^2, $3z^2$-r^2)

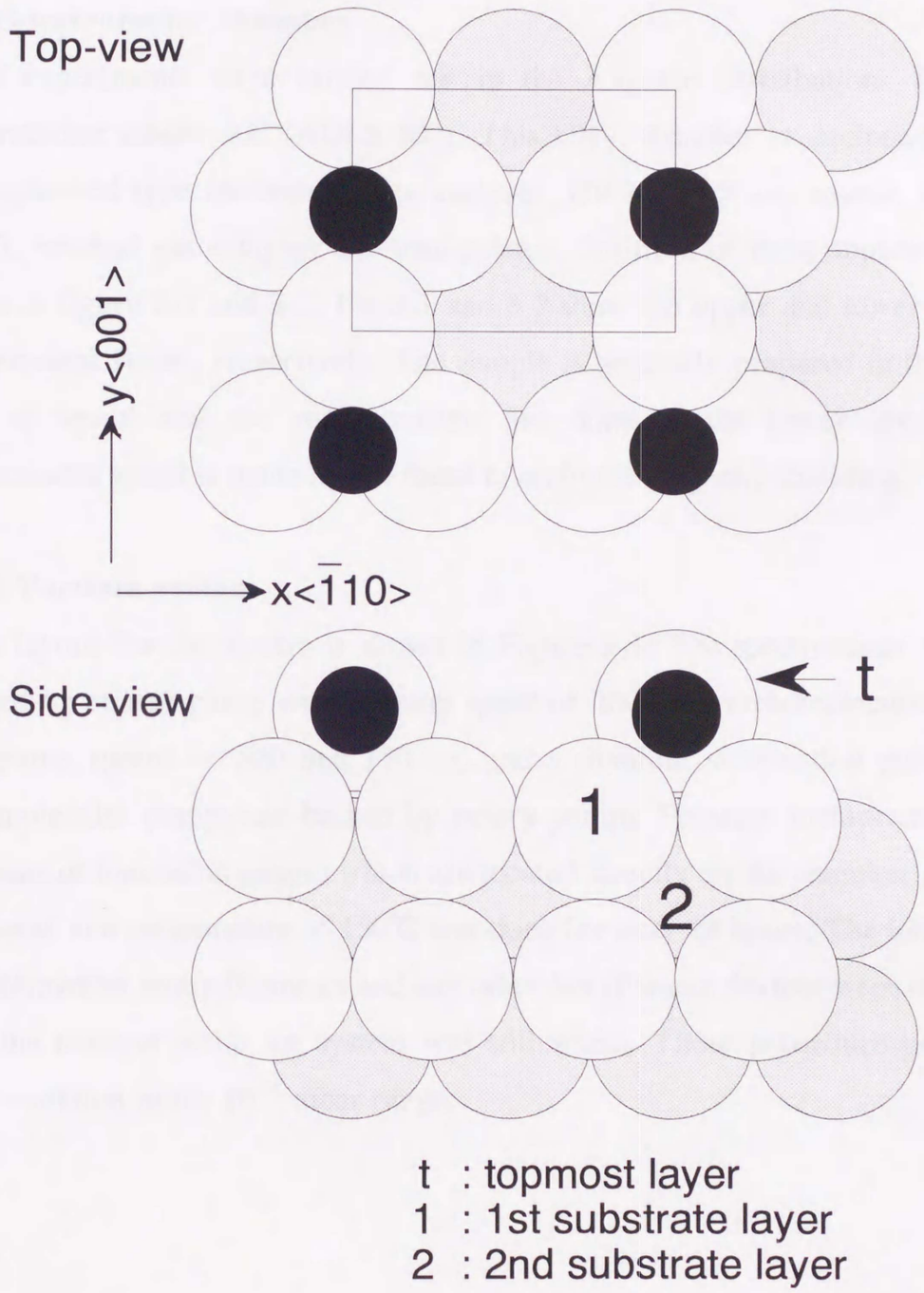

Figure 2-6. Schematic diagram of the 2x1 missing-row model adopted for the Simplified-LCAO calculation. The oxygen atoms are denoted by filled circles. A square line denotes the unit cell for the 2x1-O surface.

Chapter 3 Experiment

3.1 Spectrometer chamber

The experiments were carried out in the Angular Distributions Electron Spectrometer model 400 (ADES-400). This UHV chamber is equipped with a 150° spherical type electron energy analyzer, UV lamp, X-ray source, ion gun, LEED, residual gas analyzer and manipulator. Positions of these apparatuses are drawn in figure 3-1 and 3-2. Fig.3-1 and 3-2 show the upper and lower level of experimental vessel, respectively. The sample is generally prepared in the upper level of vessel and the measurements are done in the lower level. This spectrometer vessel is made of mu-metal to optimize magnetic shielding.

3.1.1 Vacuum system

The layout for the system is shown in Figure 3-3. The spectrometer vessel is pumped by an ion pump with a pump speed of 2000 l/s, turbomolecular pumps with pump speeds of 520 and 170 l/s, and a titanium sublimation pump. The turbomolecular pumps are backed by rotary pumps. Pressure measurements are by means of ionization gauges which are located directly on the chamber.

Bakeout at a temperature of 150℃ was done for over 24 hours. The ion gauges, the sublimation pump filaments and any other hot filament devices were outgassed after the bakeout while the system was still warm. Those procedure permitted UHV condition in the 10^{-11} mbar range.

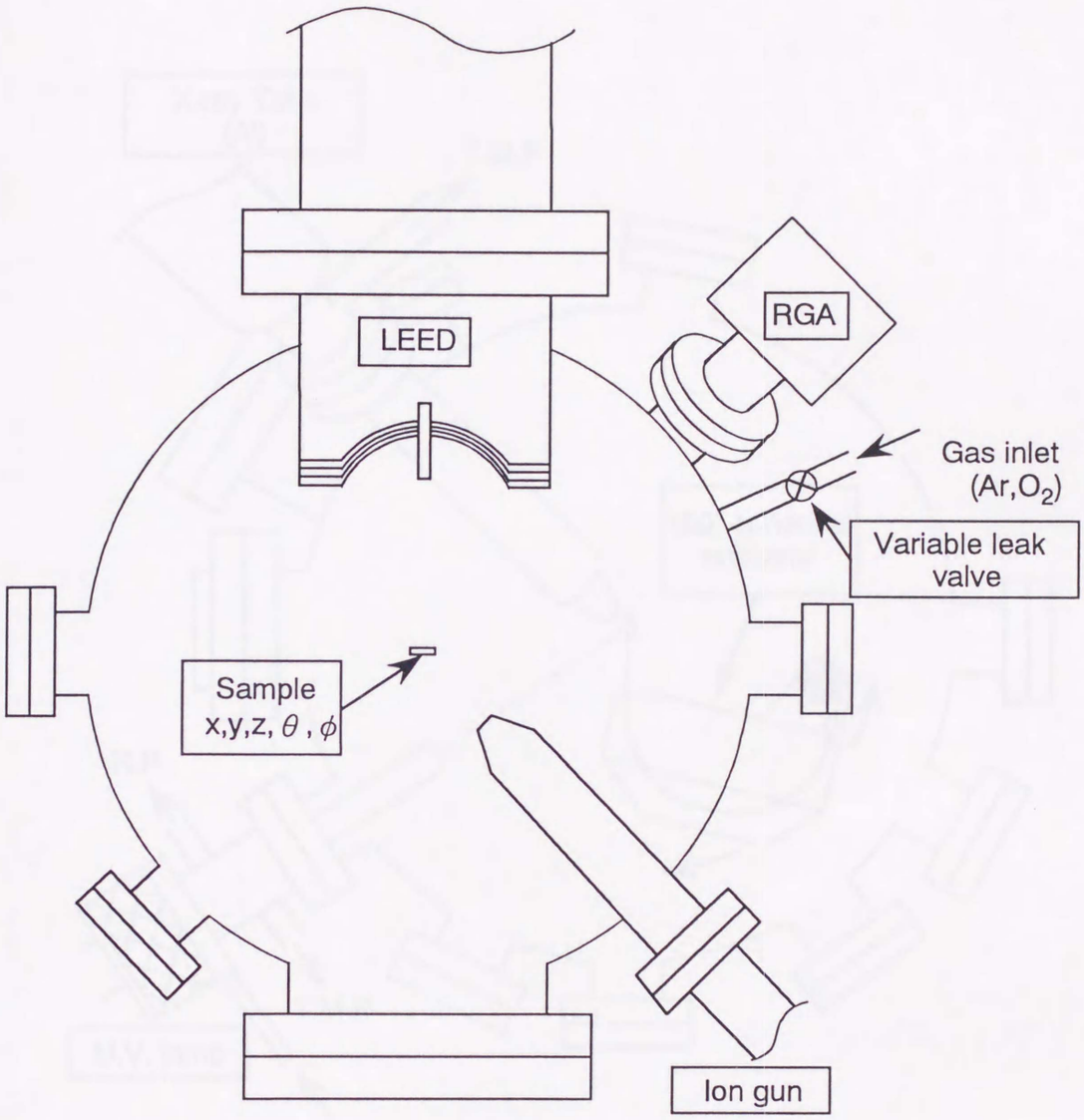

Figure 3-1. Upper level of experimental vessel (VG Ltd. ADES-400).

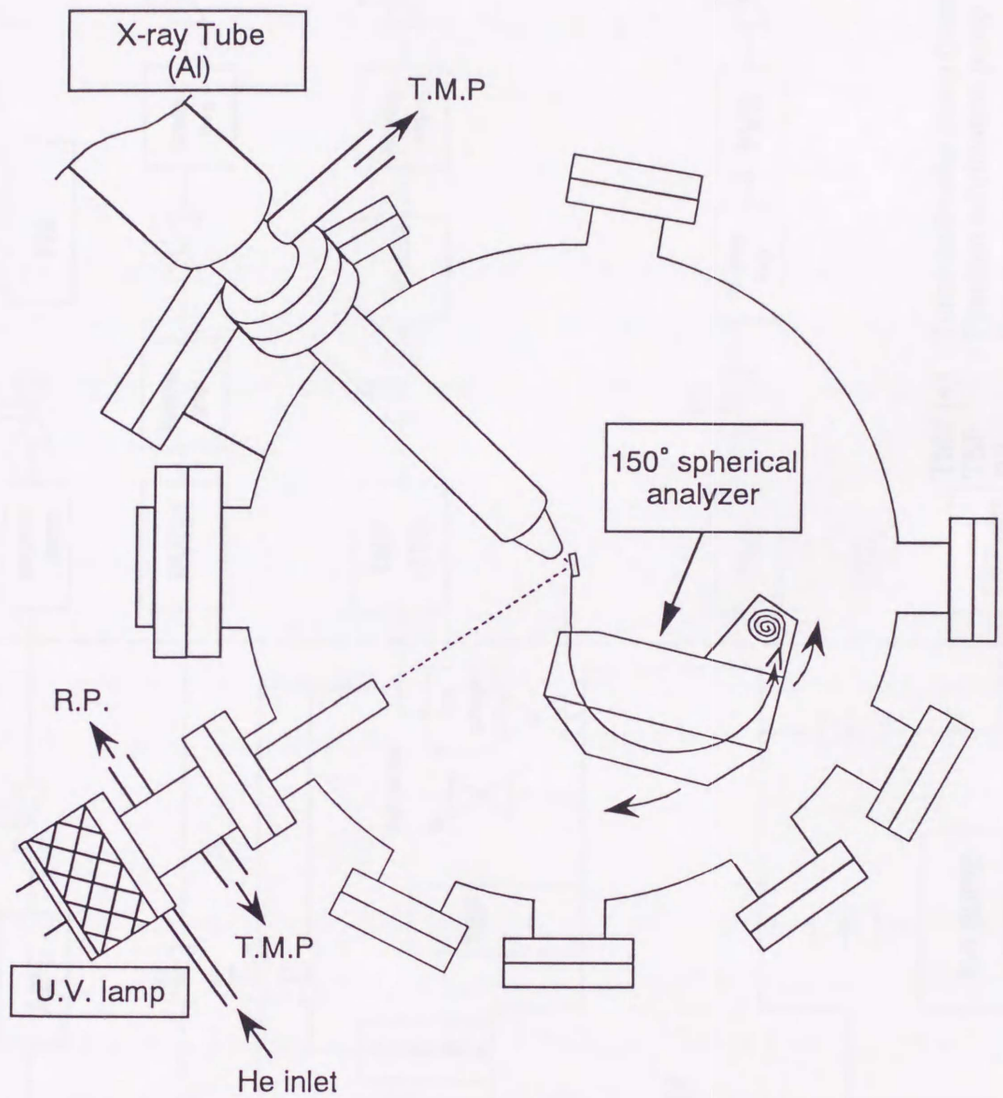

Figure 3-2. Lower level of experimental vessel.

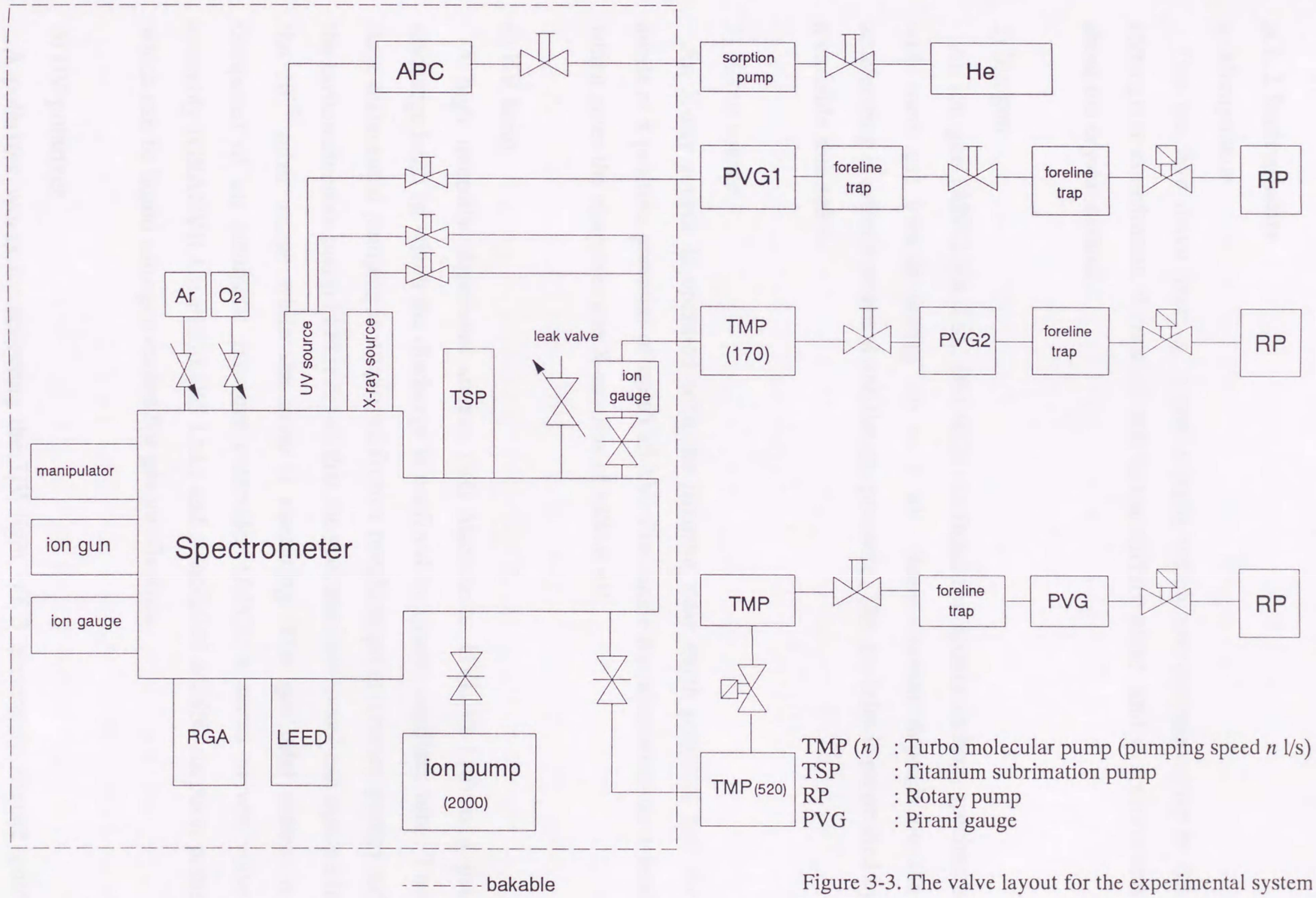

Figure 3-3. The valve layout for the experimental system

3.1.2 Instruments

1) Manipulator

This has five drive axes; x, y and z shifts which are corresponding to the rectangular coordinates, θ rotation axis in the surface plane, and ϕ rotation axis about the crystal normal.

2) Ion gun

An ion gun (ANELVA Ltd., 981-9201) is fitted for sputter etching specimens with inert gas ions at energy up to 3 kV. Beam current depends on the accelerating electrode potential and the gas pressure. The gas inlet is controlled by a variable leak valve.

3) X-ray source

An X-ray source is operated with the filament near earth potential and the anode at a positive potential of up to 15 kV. The anode has aluminum on a head which gives the characteristic X-ray line at 1486.6 eV.

4) UV lamp

A high intensity ultraviolet source (VG Microtech, UVL-HI-126) is a gas discharge lamp in which the discharge is confined by quartz capillary tube. Two stage differential pumping is employed from a roughing pump (rotary pump) and the turbomoleculer pump (TPU170) so that the spectrometer vessel can operate in the 10^{-10} mbar range while the lamp is operating. The gas inlet system is composed of an automatic pressure controller (APC), a servo driven valve assembly (GRANVILLE-PHILLIRS Ltd.) and a modified MSS50 sorption pump which can be liquid nitrogen cooled for gas purification.

5) UV polarizer

A polarizer works by reflecting the UV light off 3 accurately aligned gold

plated mirrors. The angle of incidence of the light onto these mirrors has been optimized to polarize HeI radiation. The optical system can rotate off axis with respect to the UV beam so that it is possible to have two directions of polarization at right angles to each other. In addition there is a straight through unpolarized light position. The degree of polarization is greater than 90%.

6) Residual gas analyzer (RGA)

An RGA (Anelva Co., AGA-100) is composed of an ion source, a quadrupole mass filter and a Faraday cup. This is fitted to the vessel and the residual gasses are ionized by the ion source. The gas ions are collected by the Faraday cup depending on their mass and charge through the mass filter. A mass pattern of residual gasses of the vessel is measured.

7) Low energy electron diffraction (LEED)

A LEED (ULVAC Co., Model 15 LEED optics) is composed of an electron gun, four mesh grids and a screen. A diameter of the electron beam is 1 mm or less. The electron beam emits to specimens at energy up to 3 kV. The screen is coated by Zn_2SiO_4 and subtends an angle of 120° at the specimen. A screen bias voltage is up to 5 kV.

8) Analyzer

An electron energy analyzer is a 150° spherical type analyzer with a 50 mm mean radius. The analyzer can be operated in either of two modes. The first is the constant analyzer energy (CAE) mode where the pass energy of the electrons transmitted through the analyzer is fixed during a spectrum. The second is the constant retard ratio (CRR) mode where the ratio of kinetic energy to pass energy is constant during a spectrum. In the CAE mode, energy resolution ΔE is fixed during a spectrum and is determined by the analyzer pass energy setting.

The inlet and exit slit widths of the analyzer are 1 mm. An angular resolution is

2°. The analyzer is mounted on a rotatable table so that it can be moved in one plane around a specimen (both vertically and horizontally). The electron passed through the analyzer are detected by a channel electron multiplier (channeltron) mounted behind the exit slit.

9) Spectrometer control

A spectrometer control system is schematically drawn in figure 3-4. A spectrometer control unit (SCU) provides operating voltage for the analyzer. It supplies positive and negative hemisphere voltages and retard potential. The SCU includes providing programming outputs for multiplier supply and external inputs for computer control of the spectrometer. The SCU is controlled by a computer (NEC, PC9801). Pulses from the channeltron are fed via a DC isolating capacitor to the pulse counting circuits. They first encounter pulse sharping and amplifying circuits and then encounter a discriminator which allows only those pulses whose heights are sufficiently large to pass. Those pulses which are approximately 5 V in amplitude and of 500 ns duration, are finally fed to the counter.

3.2 Sample preparation

3.2.1 Samples

a) Copper

A Cu(110) single crystal (Johnson&Massay Ltd.) of 99.999% purity with <0.5° miscut was mechanically polished with alumina paste (Baiokalox) down to 0.05μm and electrochemically etched by 6% nitric acid for few seconds. Immediately it was washed clean with distilled water before installation in the spectrometer. Its dimension was 10mm diameter and 2mm thickness.

b) Nickel

A Ni(110) single crystal (Metal Crystals & Oxides Ltd.) of 99.999% purity with <1° miscut was mechanically polished with diamond compound (Buehler)

down to 0.25μm and electrochemically etched by 5% nitric acid for few seconds. Immediately it was washed clean with alcohol and distilled water before installation in the spectrometer. Its dimension was 10mm diameter and 2mm thickness.

c) Silver

An Ag(110) single crystal (Material-Technologie & Kristalle) was of 99.999% purity, <0.5° miscut and <0.03μm surface roughness. Its dimension was 10mm diameter and 1mm thickness. It was electrochemically etched by 6% nitric acid for few seconds. Immediately it was washed clean with distilled water before installation in the spectrometer.

3.2.2 Sample holder

Figure 3-5 shows a sample holder. The sample was fitted on a processed Mo plate by Ta tips. A filament (1% thoriated tungsten wire of ϕ0.3 mm) was installed behind the sample for the purpose of sample heating by its radiation. This sample holder was mounted on a rotatable table of the manipulator. As written in 3.1.2, the manipulator allows linear motions in three directions and axial rotations. The rotatable table could be rotated about the crystal normal (azimuth ϕ) and about an axis in the surface plane (polar angle θ), see Figure 3-5. An error of the crystal surface normal depending to the azimuth (ϕ), was adjusted within 0.2°. The sample was electronically isolated by ceramic insulators. A Chromel-Alumel thermocouple was attached to the end of the sample.

3.2.3 Sample cleaning

The surface of sample was polished mechanically and electrochemically, whereas it is unevenness microscopically and has impurities. Then an argon ion bombardment and an annealing were necessary for the purpose of leveling the unevenness and removing impurities.

The samples were cleaned by repeated cycles of the Ar ion bombardment and annealing.

1) Argon ion bombardment

High purity argon gas (99.999%) was induced to the spectrometer vessel via a gas inlet variable leak valve. The argon gas was ionized and accelerated at a beam energy which is corresponding to a voltage between a filament of the ion gun and the sample. These accelerated ions sputter impurities.

2) Annealing

The sample was heated by the radiation of the filament installed behind the sample. This was done for the purpose of leveling and ordering the surface.

The concrete conditions of cleaning procedures are described below:

a) Cleaning of Copper

For cleaning, a procedure of argon ion bombardment and annealing like below was done. In addition, a short annealing was made to keep the clean surface every 2 hours.

Argon ion bombardment

Target current	~3 μA
Beam energy	~500 V
Incident angle	45°
Inlet gas pressure	5×10^{-5} mbar
Emission current	20 mA
Duration	30 min

Annealing

Temperature	673 K

Duration 60 min

Short annealing

Series of at 773 K for 2 min and at 673 K for 10 min.

b) Cleaning of Nickel

Argon ion bombardment

Target current	~3 μA
Beam energy	~700 V
Incident angle	45°
Inlet gas pressure	5×10^{-5} mbar
Emission current	20 mA
Duration	15 min

Annealing

Temperature	773 K
Duration	30 min

c) Cleaning of Silver

Argon ion bombardment

Target current	~3 μA
Beam energy	~500 V
Incident angle	45°
Inlet gas pressure	5×10^{-5} mbar
Emission current	20 mA
Duration	30~60 min

Annealing

Temperature	673 K
Duration	20 min

3.2.4 Checking the surface cleanliness

The surface was checked about impurities and an ordering by some techniques like below, whether the surface was clean or not.

1) X-ray photoelectron spectroscopy (XPS)

Electrons in core levels of the specimen could be exited by X-ray because its energy is enough high (1486.6 eV). It is able to determine atomic species due to their characteristic core levels by measuring XPS spectra. The sample surface was checked whether impurities like Carbon, Sulfur, Oxygen and so on, were removed by the cleaning procedure. After several cleaning procedures, ratios of numbers of various impurity atoms to a number of Cu, Ni or Ag atoms were all 1% or less.

For example, Figure 3-6 and 3-7 show XPS spectra of Ag before and after cleaning at photon energy 1486.6 eV (Al Kα line). Before cleaning, C*1s* peak at 283.4 eV and O*1s* peak at 531.3 eV are observed with Ag*3s*, *3p(1/2,3/2)*, *3d(3/2,5/2)*, *4s*, *4p* and *4d* peaks. After cleaning, the peaks of impurities vanish.

2) Low energy electron diffraction (LEED)

When a low energy (~100 eV) electron beam is irradiated to the sample surface, its diffraction pattern, which is a map of a reciprocal lattice of a crystal, is observed on a fluorescent screen. The high atomic scattering cross sections for electrons with energies less than 1000 eV suggest that LEED should be extremely sensitive to surface atomic arrangements. Because this is diffraction, when the sharp spots with a low background are observed the surface crystal is well ordered.

Sharp spots with a low background were observed for all samples after cleaning procedures.

In addition, ultraviolet photoelectron spectroscopy (UPS) spectra and work

functions (WF) were measured for reference.

Electrons in valence bands are mainly observed by UPS. Because the valence bands have a close relation to conditions of the surface, the time dependence of UPS spectra shapes is a good reference for conditions of the surface.

A value of WF is sensitive to conditions of the surface. So this is also a good reference. Each WF of surfaces was checked before measuring.

3.2.5 The oxygen adsorption on Cu(110), Ni(110) and Ag(110) surface

The samples were exposed to oxygen with 99.99% purity in the spectrometer vessel to prepare O-induced reconstruction surfaces.

a) Copper

The clean Cu(110) surface was exposed to 100 Langmuir*) (L) O_2 ($=1.0\times10^{-6}$ mbar $\times$ 133sec.) immediately after cleaning. The surface was then annealed at 473 K for 2 min. Then a very sharp and intense 2×1 LEED pattern appeared. The ARUPS measurements were performed within 8 hours to keep free from contaminations referring to the WF and the shapes of ARUPS spectra.

*) 1 L = 1.0×10^{-6} torr sec.

b) Nickel

The clean Ni(110) surface was exposed to 0.8 L O_2 ($=2.0\times10^{-8}$ mbar $\times$ 53sec.) and 4 L at temperature 700 K. Then a very sharp and intense 2×1 and 3×1 LEED pattern appeared, respectively. The ARUPS measurements were performed within 6 hours to keep free from contaminations referring to the WF and the shapes of ARUPS spectra.

c) Silver

When the clean Ag(110) surface was exposed to 3,600~22,500 L O_2 at sample temperature from 480 K to around a room temperature, the Ag(110)/nx1-O and 1x2-O LEED patterns appeared. Since a phase boundary condition between the Ag(110)/nx1-O and 1x2-O surfaces is not obvious yet, the surfaces were prepared under various conditions. Then most adopted conditions for preparing the Ag(110)/2x1-O and 1x2-O surfaces are described below.

Ag(110)/2x1-O

The clean Ag(110) surface was exposed to 15,000 L (=2×10^{-5} mbar x 1,020 sec) O_2 at sample temperature from 400 K to 360 K. Then a very sharp and intense 2 × 1 LEED pattern appeared. The ARUPS measurements were performed within 2 hours to keep free from contaminations referring to the WF, LEED observation and the shapes of ARUPS spectra.

Ag(110)/1x2-O

The clean Ag(110) surface was exposed to 12,000 L (=2×10^{-5} mbar x 800 sec) O_2 at sample temperature from 380 K to 360 K. Then a very sharp and intense 1 × 2 LEED pattern appeared. The ARUPS measurements were performed within 9 hours to keep free from contaminations referring to the WF and the shapes of ARUPS spectra.

3.3 Measurements

3.3.1 Light source

HeI(21.22 eV), HeII(40.8 eV) and NeI(16.85 and 16.65 eV) resonance lines were used for measurements of ARUPS as light sources. A linearly polarized light of HeI was prepared by the polarizer for revealing band symmetries.

3.3.2 Angle-resolved ultraviolet photoemission spectroscopy measurements

A schematic illustration of the experimental arrangement is shown in figure 3-8. An incident angle of the light to the surface normal (<110> direction) was θi, and an emission angle of photoelectrons to the surface normal was θe. The measurements were performed at various θe within an incident plane to map energy bands. The sample could be rotated about a vertical axis (θm) to change the incident angle. And it could be rotated around the surface normal (ϕ), then the measurements were capable in the $(\bar{1}10)$ or (001) mirror plane. The orientation of the crystal with respect to the analyzer as checked by LEED observation, and the surface normal was determined as an angle corresponding to a mirror point of symmetrical energy bands.

It is convenient to define binding energy as a difference from the Fermi edge (E_F), then the value of binding energies are described as positive values. UPS spectra at $\theta e=0^\circ$ were measured to determine the Fermi edges of the samples. The form of Fermi-Dirac distribution function and an energy resolution of the analyzer contribute to the width of the Fermi edge. Because a value of the former is about 25 meV at room temperature and enough smaller than that of the latter, the width of the Fermi edge is regarded as an energy resolution of the analyzer. In this experiment, energy resolutions for HeI at pass energy(Ep) -5 eV and HeII at Ep -20 eV were 120 meV and 170 meV, respectively.

3.3.3 Work function measurements

The work function was measured by the Fermi edge and a cutoff of secondary electrons in the UPS spectrum. For these work function measurements, the sample was biased by several volts ($-V_B$) to avoid some problems originating from a work function difference between the sample and the analyzer, and from that it is difficult to detect photoelectrons emitted from around the cutoff level because their kinetic energies are nearly equal zero. Then the work function (ϕ) is given by an equation below:

$$E_{cut,biased} + V_B - E_F = h\nu - \phi \ ,$$

where $E_{cut,biased}$ is a energy level of the cutoff biased by V_B.

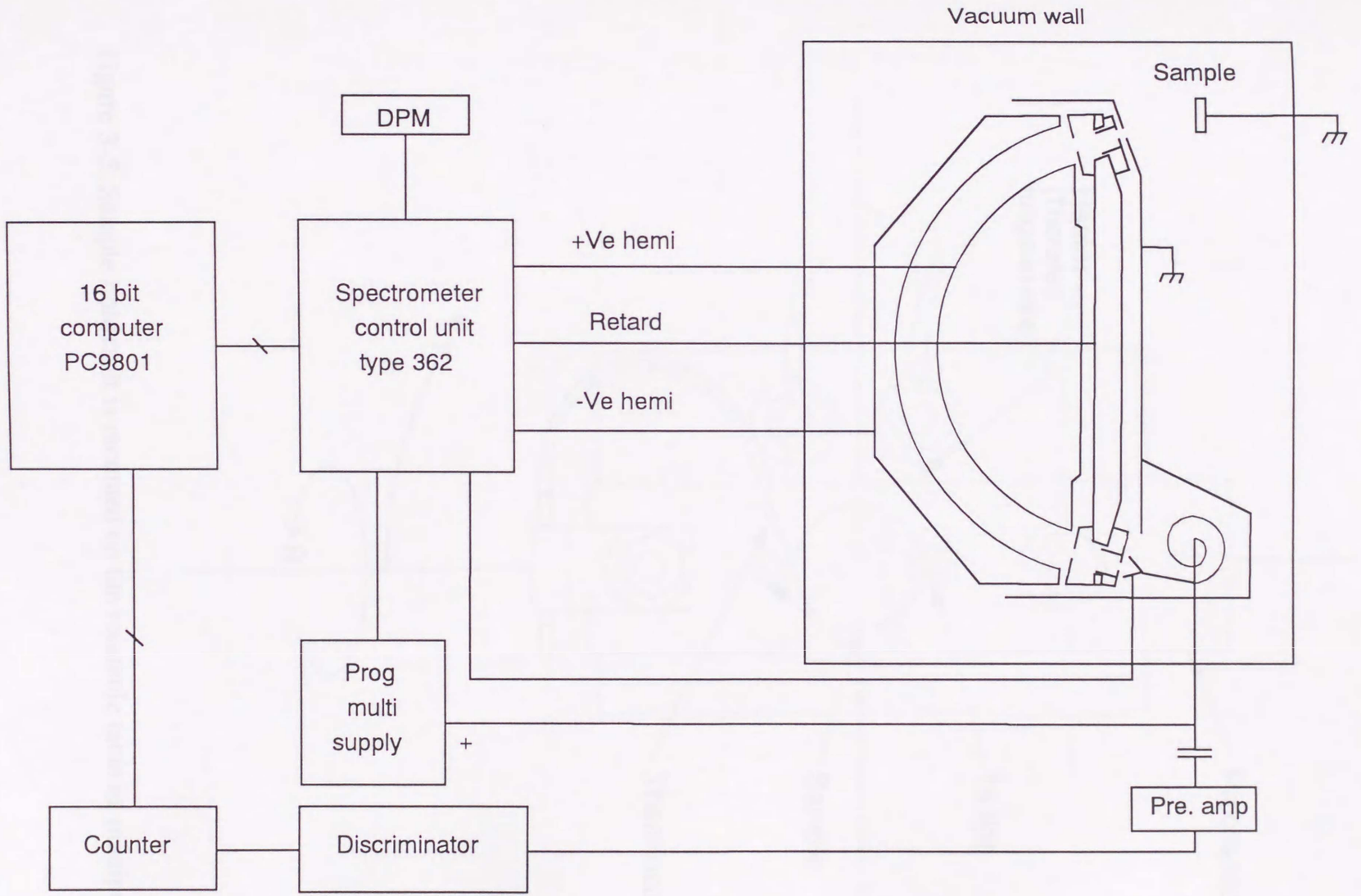

Figure 3-4. Block diagram of spectrometer control system.

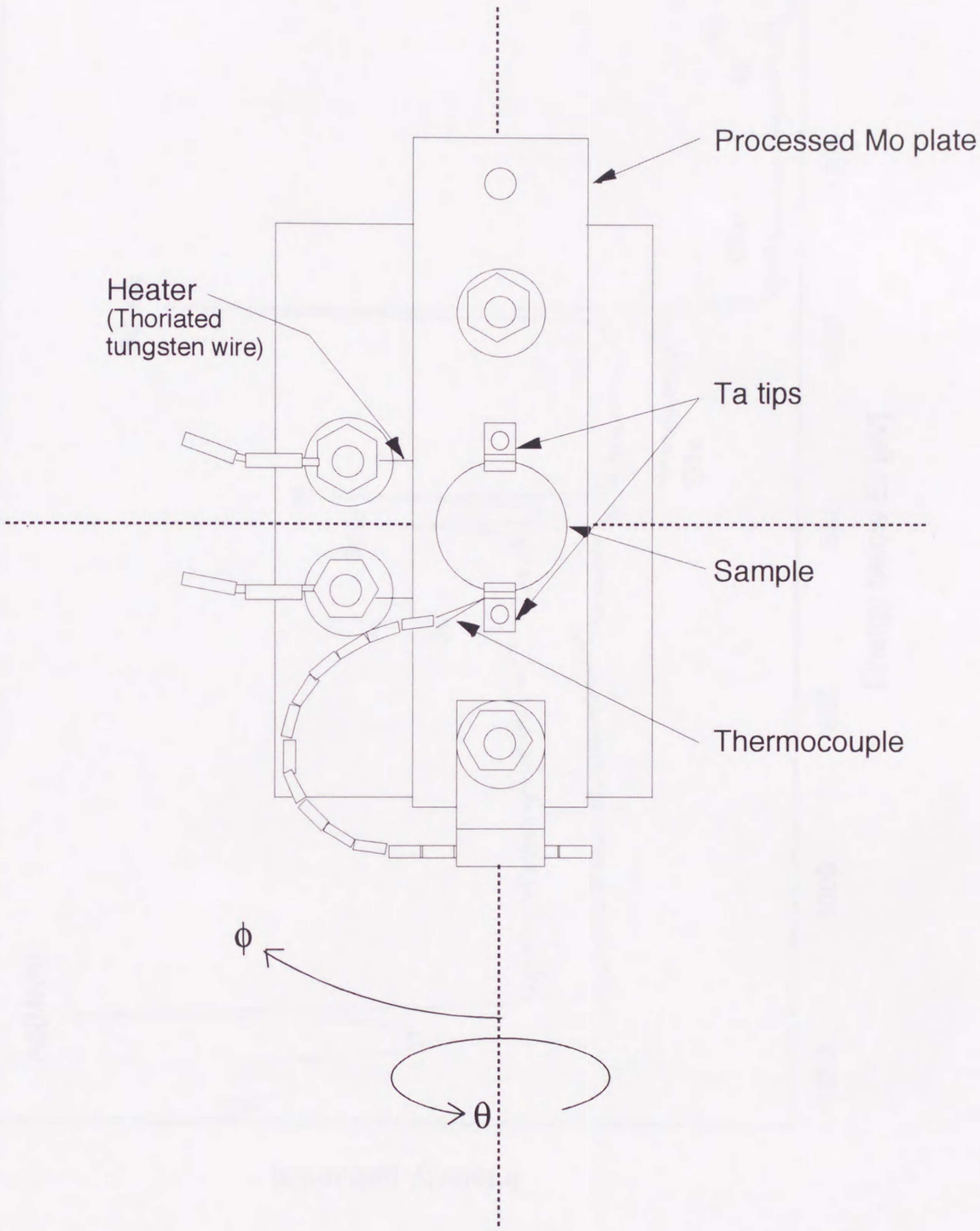

Figure 3-5. Sample holder. It is mounted on the rotatable table of manipulator.

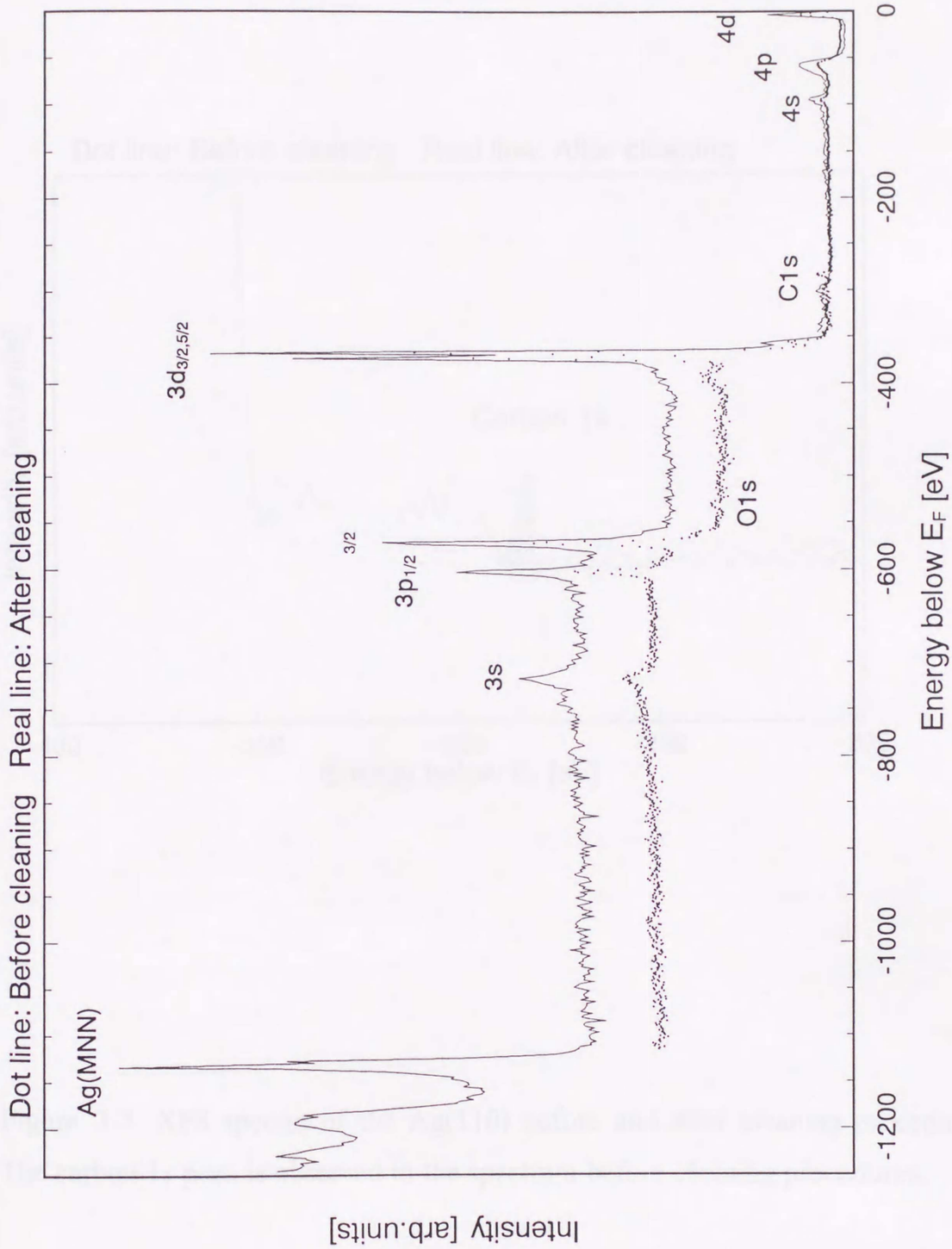

Figure 3-6. Wide scanning XPS spectra of the Ag(110) before and after cleaning procedures.

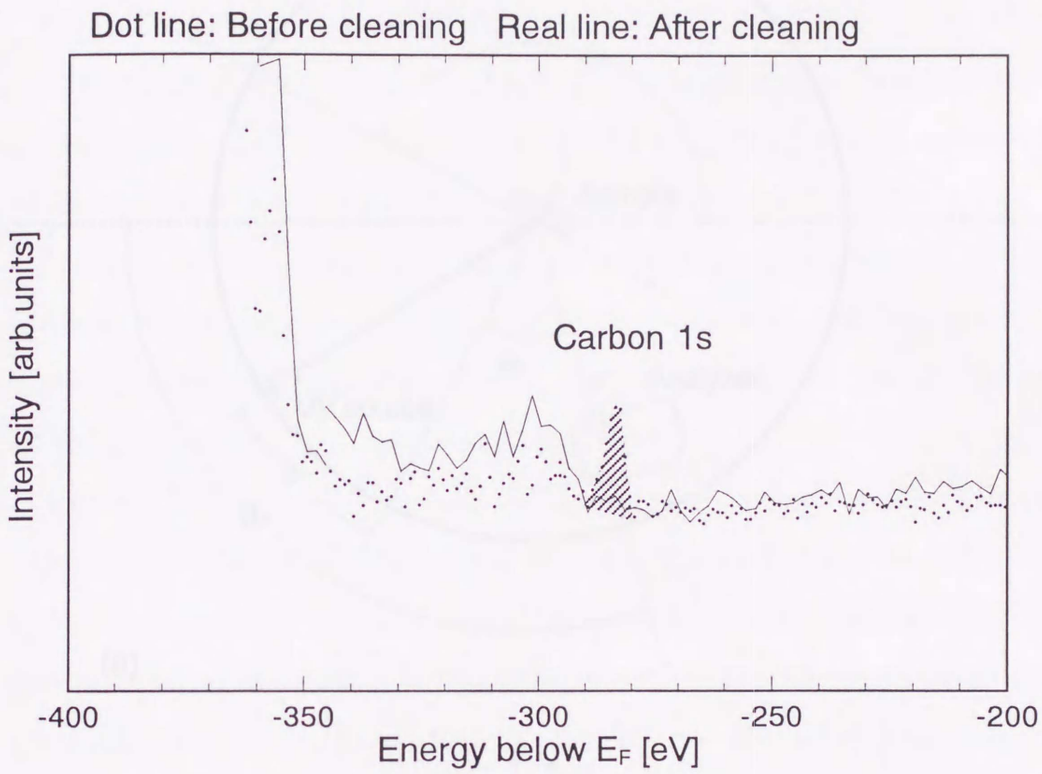

Figure 3-7. XPS spectra of the Ag(110) before and after cleaning procedures. The carbon 1*s* peak is observed in the spectrum before cleaning procedures.

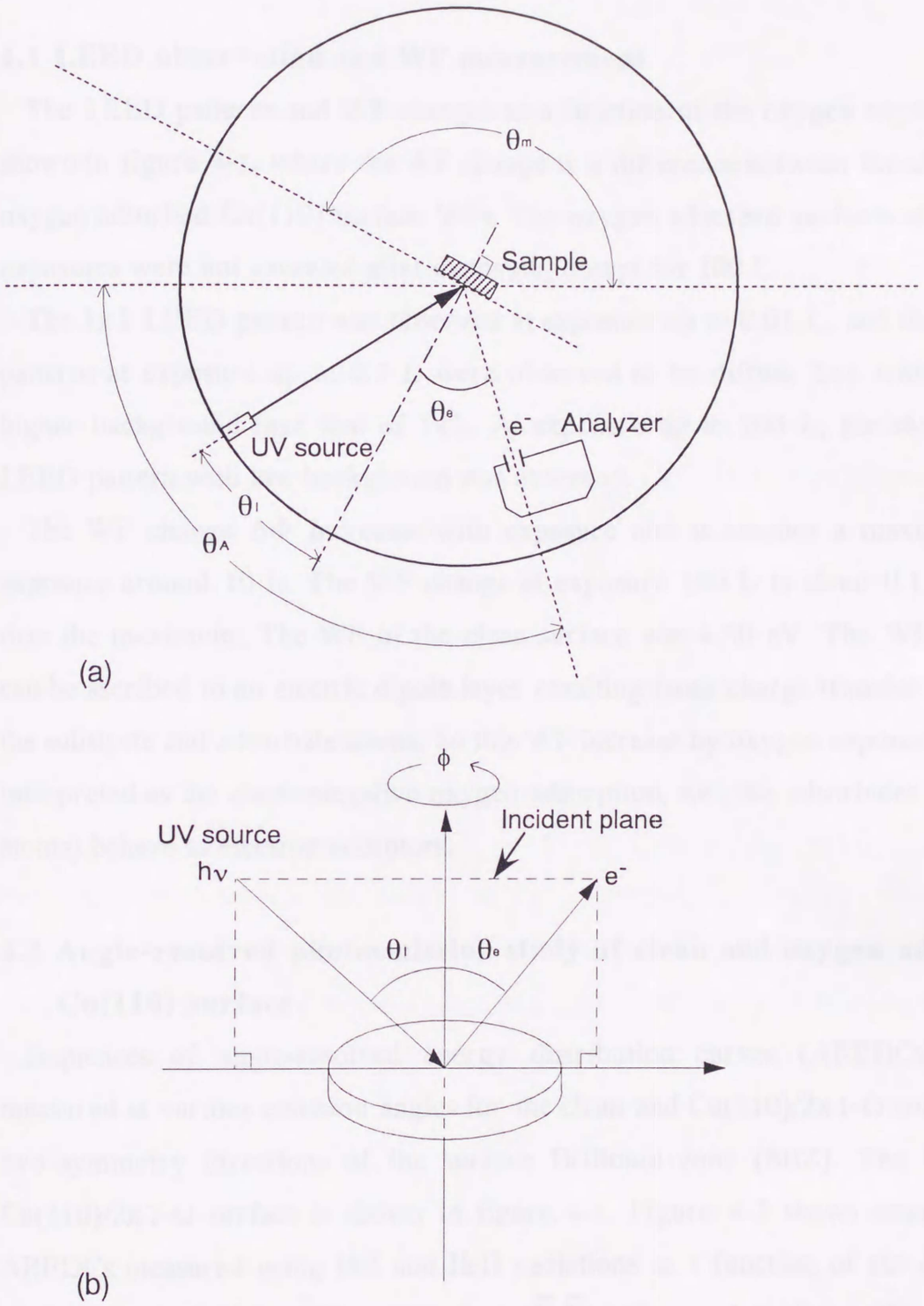

Figure 3-8. (a) Measuring geometry of the sample, UV source and analyzer. (b) Incident angle of the light and the emission angle of photoelectrons.

Chapter 4 Clean and oxygen adsorbed Cu(110) surface

4.1 LEED observation and WF measurement

The LEED patterns and WF changes as a function of the oxygen exposure are shown in figure 4-1, where the WF change is a difference between the clean and oxygen adsorbed Cu(110) surface WFs. The oxygen adsorbed surfaces at various exposures were not annealed after exposure, except for 100 L.

The 1x1 LEED pattern was observed at exposure up to 0.01 L, and the LEED patterns at exposure up to 0.5 L were observed to be diffuse 2x1 with a little higher background than that of 1x1. At exposure up to 100 L, the sharp 2x1 LEED pattern with low background was observed.

The WF change $\Delta\Phi$ increases with exposure and it reaches a maximum at exposure around 10 L. The WF change at exposure 100 L is about 0.1 eV less than the maximum. The WF of the clean surface was 4.50 eV. The WF change can be ascribed to an electric dipole layer resulting from charge transfer between the substrate and adsorbate atoms. So this WF increase by oxygen exposure can be interpreted as the electronegative oxygen adsorption, i.e., the adsorbates (oxygen atoms) behave as electron acceptors.

4.2 Angle-resolved photoemission study of clean and oxygen adsorbed Cu(110) surface

Sequences of angle-resolved energy distribution curves (AREDCs) were measured at various emission angles for the clean and Cu(110)/2x1-O surfaces in two symmetry directions of the surface Brillouin zone (SBZ). The SBZ of Cu(110)/2x1-O surface is shown in figure 4-5. Figure 4-2 shows examples of AREDCs measured using HeI and HeII radiations as a function of the emission angle θe, along the $<\bar{1}10>$ direction ($\bar{\Gamma}$-$\bar{X}$). Figure 4-3 shows the similar AREDCs along the <001> direction ($\bar{\Gamma}$-$\bar{Y}$). Solid curves in these figures indicate the AREDCs corresponding to of the Cu(110)/2x1-O surfaces, and dotted curves

indicate that of the clean Cu(110) surface. The shaded areas in those figures indicate the new features appeared in the Cu(110)/2x1-O spectra.

The features P and P* located at energy about -6 eV and about -1 eV are assigned to oxygen-induced bonding states and anti-bonding states, respectively. Here the oxygen-induced bonding and anti-bonding states mean the bonding and anti-bonding states of the oxygen and copper orbitals which contribute to the bonding. It was experimentally confirmed that these bonding states had O2*p* character [18-20]. From now on, they are abbreviated as p_x, p_y and p_z (or O-p_x, O-p_y and O-p_z) or oxygen-induced bonding and anti-bonding states. Along the $<\bar{1}10>$ direction ($\bar{\Gamma}$-$\bar{X}$) there is not practically any dispersion (± 0.1 eV). In contrast, along the <001> direction ($\bar{\Gamma}$-$\bar{Y}$) there are dispersed bands between -5.5 and -7.5 eV and one dispersed band around -1.3 eV. Only measurements along the <001> direction are discussed from now on.

Figure 4-4 shows the normal emission EDCs of the clean and Cu(110)/2x1-O surfaces, using HeI radiation polarized parallel or perpendicular to $<\bar{1}10>$ direction. As indicated in figure 4-4, the three features can be assigned to states with p_x, p_y and p_z symmetry from the polarization selection rules. The spectra were measured at three arrangements; (a) $\hat{A}$ parallel to $<\bar{1}10>$ and $\theta_I=25°$ (b) $\hat{A}$ perpendicular to $<\bar{1}10>$ and $\theta_I=25°$ (c) $\hat{A}$ perpendicular to $<\bar{1}10>$ and $\theta_I=65°$, where $\hat{A}$ is a polarization vector and the polarized radiation was irradiated in a yz mirror plane at incident angle θ_I (see Fig.2.5). Then the p_x symmetry features selectively appears at arrangement (a), in the same way, mainly p_y at (b) and p_z at (c).

Figure 4-5 shows the energy (k-E) dispersion of the oxygen induced features along the <001> direction. Measurements were performed using unpolarized and linearly polarized light. Symbolic marks denote: (•) hν=21.22 eV and hν=40.8 eV, unpolarized; (◇) hν=21.22 eV, p_x feature; (×) hν=21.22 eV, p_y feature; (□) hν=21.22 eV, p_z feature. In the figure, the *d*-band features appearing from -2 to -5 eV are neglected. The oxygen-induced bonding states between -5.5 and -7.5

eV were assigned to p_x, p_y and p_z features at several points using the selection rules. The p_y band disperses most widely from -5.9 eV at $\overline{\Gamma}$ to -7.7 eV at $\overline{Y}$. The anti-bonding partners of the -6 eV features are also shown at low energies around -1 eV. The dispersion curves show a periodicity with the substrate reciprocal lattice along <001>. This indicates that the bond of the Cu-O rows is predominantly along the <001> direction. Here, it is to be noted that the band order of the bonding states is p_x, p_y, p_z at $\overline{\Gamma}$, and is p_x, p_z, p_y at $\overline{Y}$. The p_y and p_z bands, thus, cross and hybridize at an intermediate point between $\overline{\Gamma}$ and $\overline{Y}$, as is clearly shown in the figure. This band-crossing was confirmed experimentally for the first time [33].

4.3 Simplified-LCAO calculation of Cu(110)/2x1-O surface

The simplified-LCAO calculation of Cu(110)/2x1-O surface was performed to compare with the experimental features described in chapter 4.2. Before calculating the Cu(110)/2x1-O surface, a calculation of clean surface was made. The LCAO parameters of Cu-Cu interactions were adopted from the literature [34]. Figure 4-6 shows a calculation of the clean surface including 5 substrates along the <001> direction ($\overline{\Gamma}$-$\overline{Y}$) with the experimental energy bands of the clean surface in a reduced scheme. A Cu *3d*-band width W of the calculation is in good agreement with that of the experiment. Then it was concluded that the energy bands were reproduced quantitatively by the present calculation. The Fermi level was adjusted so that both the *d*-band levels were in agreement.

Figure 4-7 shows the calculation of Cu(110)/2x1-O surface together with the experimental results. The LCAO parameters for the Cu-Cu interactions were also adopted from the literature [34]. The Cu-O interactions, $sP\sigma$, $pP\sigma$, $pP\pi$, $Pd\sigma$, $Pd\pi$, surface shift (ss) and the on-site energy of O orbitals E_{Op} given in table 2-2, were treated as adjustable parameters to fit the experimental results. The symbolic marks are same as in Fig.4-5. The open circles denote the calculated energy bands and each calculated band, which has dominantly p_x, p_y and p_z character, is shaded

for the purpose of easy recognition of the correspondence between the calculation and experiment.

Here it is useful to introduce a representation of the symmetry group for discussing about the band symmetries. The point group symmetry of the Cu(110)/2x1-O surface is C_{2v} in Schoenflies symbol (2mm in the international crystal class). So the bases (s, x, y, z, xy, yz, zx, x^2-y^2, $3z^2$-r^2) belong to four irreducible representations (A1, A2, B1, B2) as described in table 4-1 at $\overline{\Gamma}$, $\overline{X}$, $\overline{Y}$, $\overline{X'}$ and $\overline{Y'}$, where possible point group operations are:

E : Identity operation

C_2 : 180° rotation around the normal axis

σx : Reflection to the yz-plane

σy : Reflection to the zx-plane .

Table 4-1 : Irreducible representations

C_{2v}	Bases	E	C_2	σx	σy
A1	z, x^2-y^2, $3z^2$-r^2, s	1	1	1	1
A2	xy	1	1	-1	-1
B1	x, zx	1	-1	-1	1
B2	y, yz	1	-1	1	-1

As shown in table 4-1, O2p_x, p_y and p_z orbitals belong to the different irreducible representations at symmetry points. The number of possible point group operations on any intermediate points along the <001> or <$\bar{1}$10> direction, however, decreases to only two (E and σx or σy). As it decreases, the number of irreducible representations decreases to two (A and B). The irreducible representations along the <001> and <$\bar{1}$10> direction are shown in table 4-2.

Table 4-2

(a) Irreducible representations along the <001> direction ($\bar{\Gamma}$-$\bar{Y}$)

	Bases	E	σx	
A	s, y, z, yz x^2-y^2, $3z^2$-r^2	1	1	A1, B2
B	x, xy, zx	1	-1	A2, B1

(b) Irreducible representations along the <$\bar{1}$10> direction ($\bar{\Gamma}$-$\bar{X}$)

	Basis	E	σy	
A	s, x, z, zx x^2-y^2, $3z^2$-r^2	1	1	A1, B1
B	y, xy, yz	1	-1	A2, B2

The bands belonging to A1 and B2 at $\bar{\Gamma}$ and $\bar{Y}$ are compatible with each other on intermediate points along the <001> direction, because they belong to the same representation A. As same as this; A2 and B1 along <001>, A1 and B1 along <$\bar{1}$10> and A2 and B2 along <$\bar{1}$10>. The compatibility was confirmed experimentally as shown in Fig.4-7.

In Fig.4-7 again, as for calculated bands, B1 band at $\bar{\Gamma}$ with p_x symmetry, is connected to B1 band at $\bar{Y}$, in good agreement with the experiment. Between $\bar{\Gamma}$ and $\bar{Y}$, A1 band at $\bar{\Gamma}$ with p_z symmetry hybridizes with B2 band at $\bar{\Gamma}$ with p_y symmetry; between $\bar{\Gamma}$ and $\bar{Y}$, both bands belong to the same irreducible representation, and A1 at $\bar{\Gamma}$ is compatible to B2 at $\bar{Y}$. The present calculation, thus, can reproduce quite satisfactorily the band crossing as well as the band order found in the present experiment. The large dispersion of the O-$2p_y$ band is mainly ascribed to the interaction between the O(p_y) and Cu($d_{X^2-y^2}$) orbitals in the

surface, whose wavefunctions are directed to the <001> direction. The O-p_y feature can be explained by B2 band at $\overline{\Gamma}$ until about 1/4 of $\overline{\Gamma}$-$\overline{Y}$. From that point, however, A1 band strongly hybridizes with subsurface Cu-4s bands and the fitting is rather ambiguous. The parameters of the Cu-O interactions are listed in Table 4-3. They are nearly in the same magnitude as those adopted in the report by Tjeng et al. [21]

Figure 4-8 shows the deviations of the calculated bands when the parameter Pdσ is shifted $\pm$0.2 eV (~10%) from the definitive value given in table 4-3. The open circles and dots denote the results of the deviated and definitive calculations, respectively. The Pdσ is shifted by -0.2 eV in (a). B1 band shifts downward through $\overline{\Gamma}$-$\overline{Y}$. B2 band, on the other hand, shifts downward about twice the B1 at $\overline{Y}$, while it does not shift so much at $\overline{\Gamma}$. A1 band does not suffer the influence by the deviation so much than B1 and B2, simultaneously the Cu*4s* bands with which the p_z (A1) band hybridizes suffer the influence especially around $\overline{\Gamma}$. In (b) shifted +0.2 eV, the bands almost shift in the opposite direction. Thus the calculation is sensitive to a slight change in the parameter. This is one of examples for fitting procedures.

Table 4-3 : LCAO parameters of Cu(110)/2x 1-O surface

	(nn)	(nnn)	[eV]
[Cu-O two-center integrals]			
sPσ	0.30	0.100	
pPσ	1.98	0.659	
pPπ	-0.50	-0.167	
Pdσ	-2.00	-0.292	
Pdπ	0.70	0.102	
[Cu-Cu two-center integrals]			
ssσ	-1.02288	-0.01252	
spσ	1.57433	0.16613	
ppσ	2.67612	0.73322	
ppπ	0.26395	0.11511	
sdσ	-0.42273	-0.11592	
pdσ	-0.44749	-0.07293	
pdπ	0.23851	0.04367	
ddσ	-0.34912	-0.06136	
ddπ	0.24490	0.03279	
ddδ	-0.05551	-0.00039	
[On-site energies from E_F and Surface Shift (ss)]			
E_{Op} =	-3.9		
Surface shift (ss) = 0.7			
Ep =	9.81559		
Es =	2.21199		
Ed1 =	-3.52408		
Ed2 =	-3.54136		

(nn) and (nnn) denote a nearest-neighbor and a next-nearest-neighbor Slater-Koster two-center integrals, respectively. The letter s,p,d,P denote the Cu 4s,4p,3d and O2p orbitals, respectively. Notations of the on-site energies are same as in table 2-2.

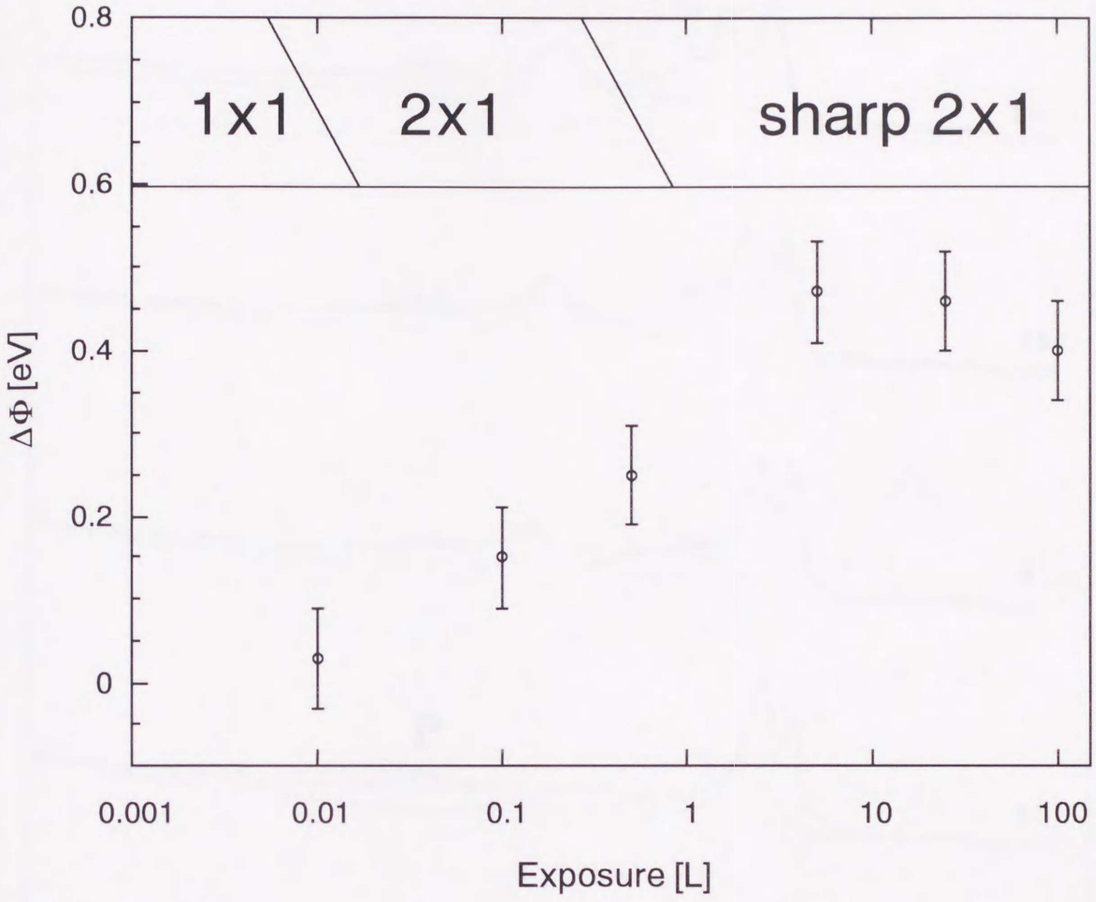

Figure 4-1. LEED patterns and the work function changes as a function of the oxygen exposure. The WF change is a difference between the clean and oxygen adsorbed Cu(110) surface WFs.

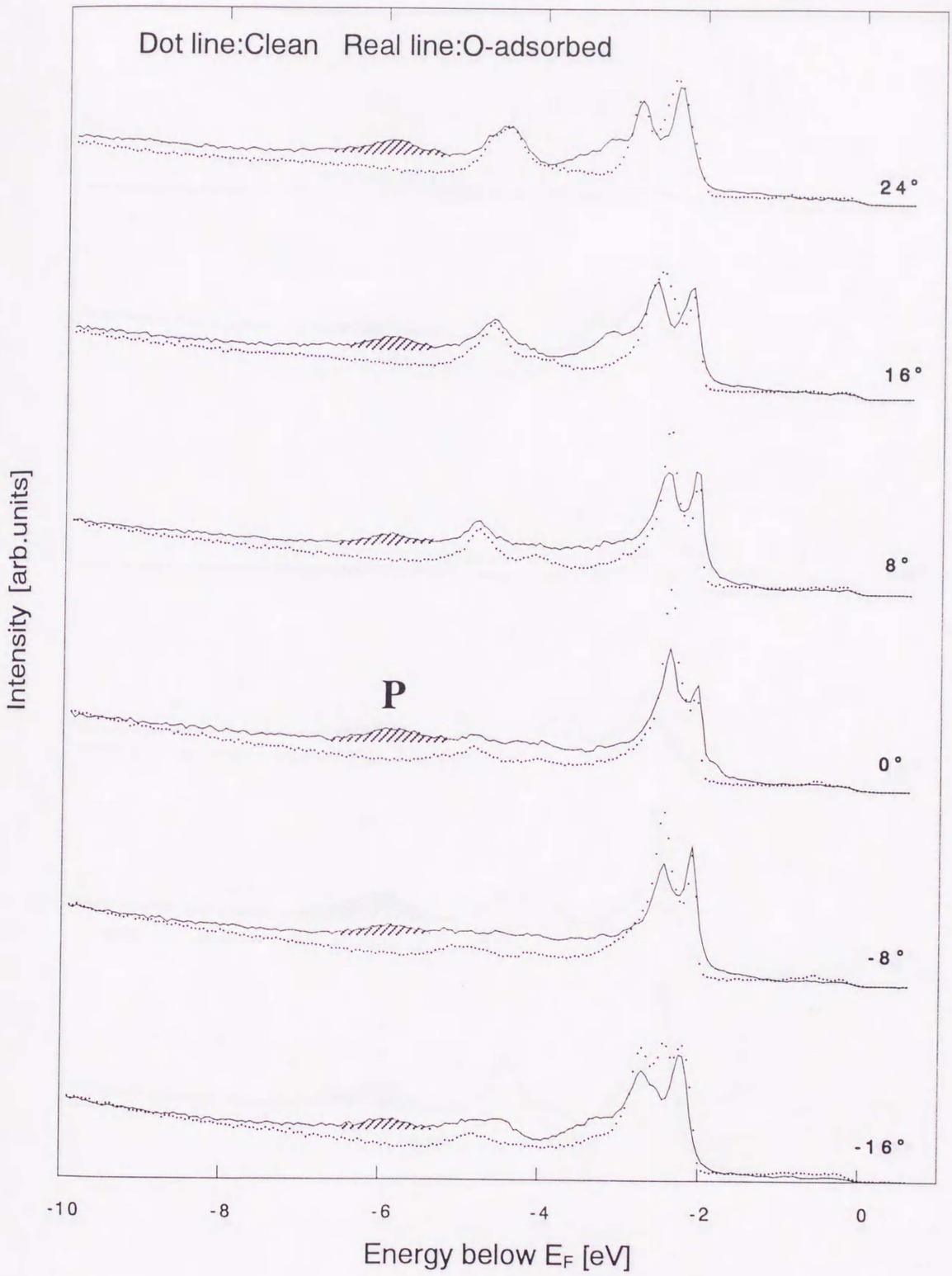

Figure 4-2(a). AREDCs measured using HeI radiation as a function of the emission angle θe (-16°~24°) along the <$\bar{1}$10> direction ($\bar{\Gamma}$-$\bar{X}$). The shaded areas indicate the O-induced states.

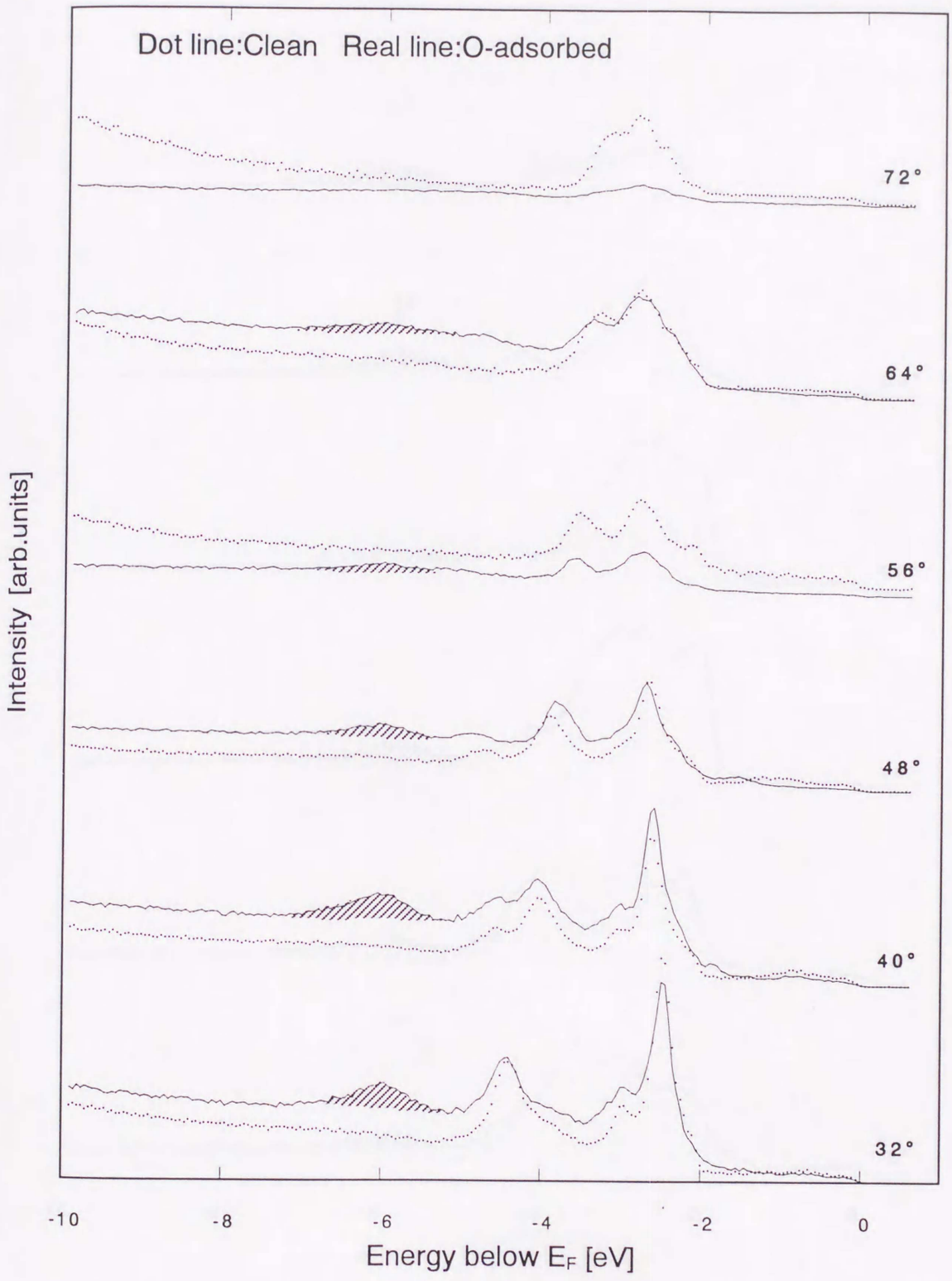

Figure 4-2(b). AREDCs measured using HeI radiation as a function of the emission angle θe (32°~72°) along the <$\bar{1}$10> direction ($\bar{\Gamma}$-$\bar{X}$).

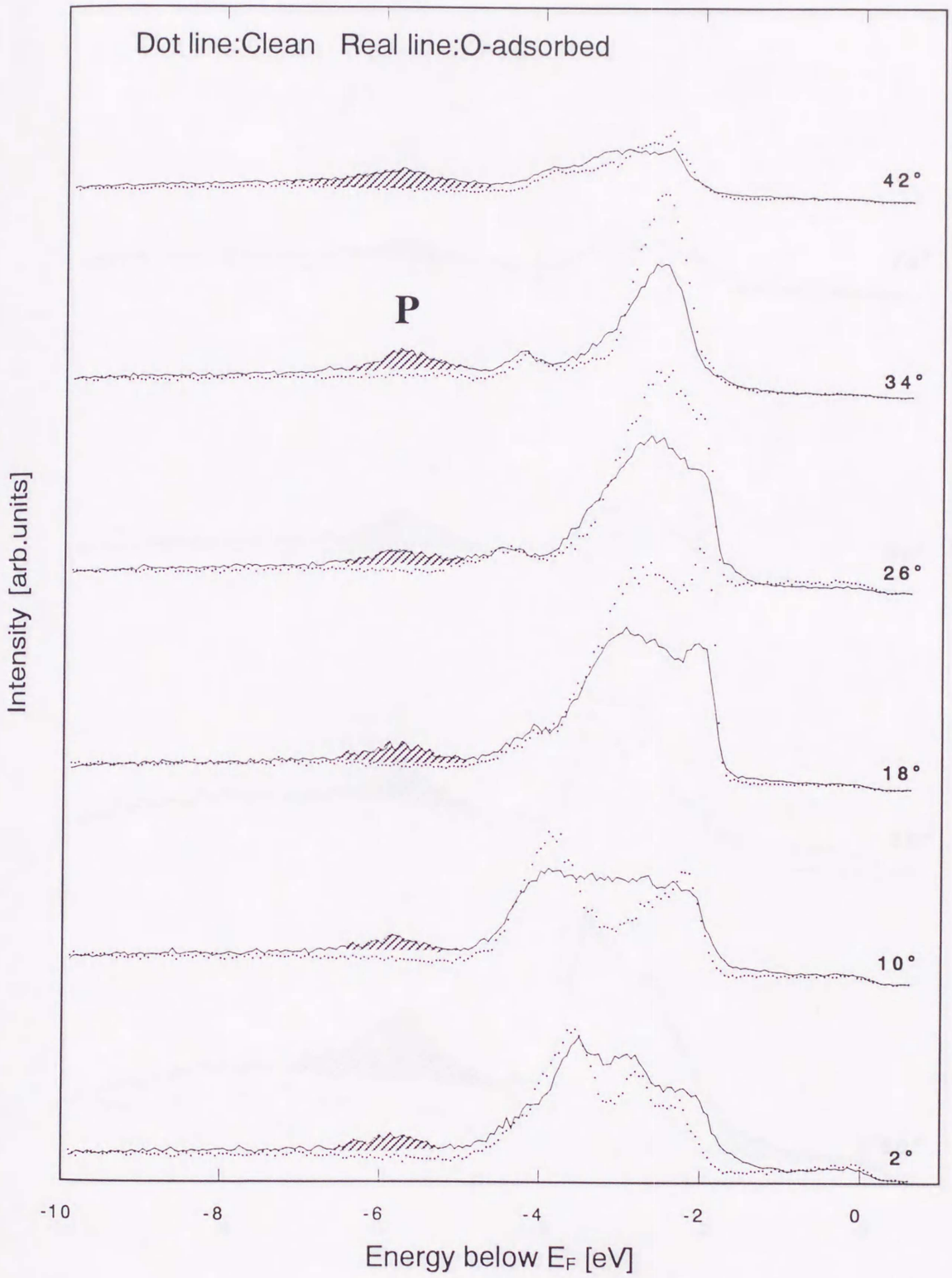

Figure 4-2(c). AREDCs measured using HeII radiation as a function of the emission angle θe (2°~42°) along the <$\bar{1}$10> direction ($\bar{\Gamma}$-$\bar{X}$).

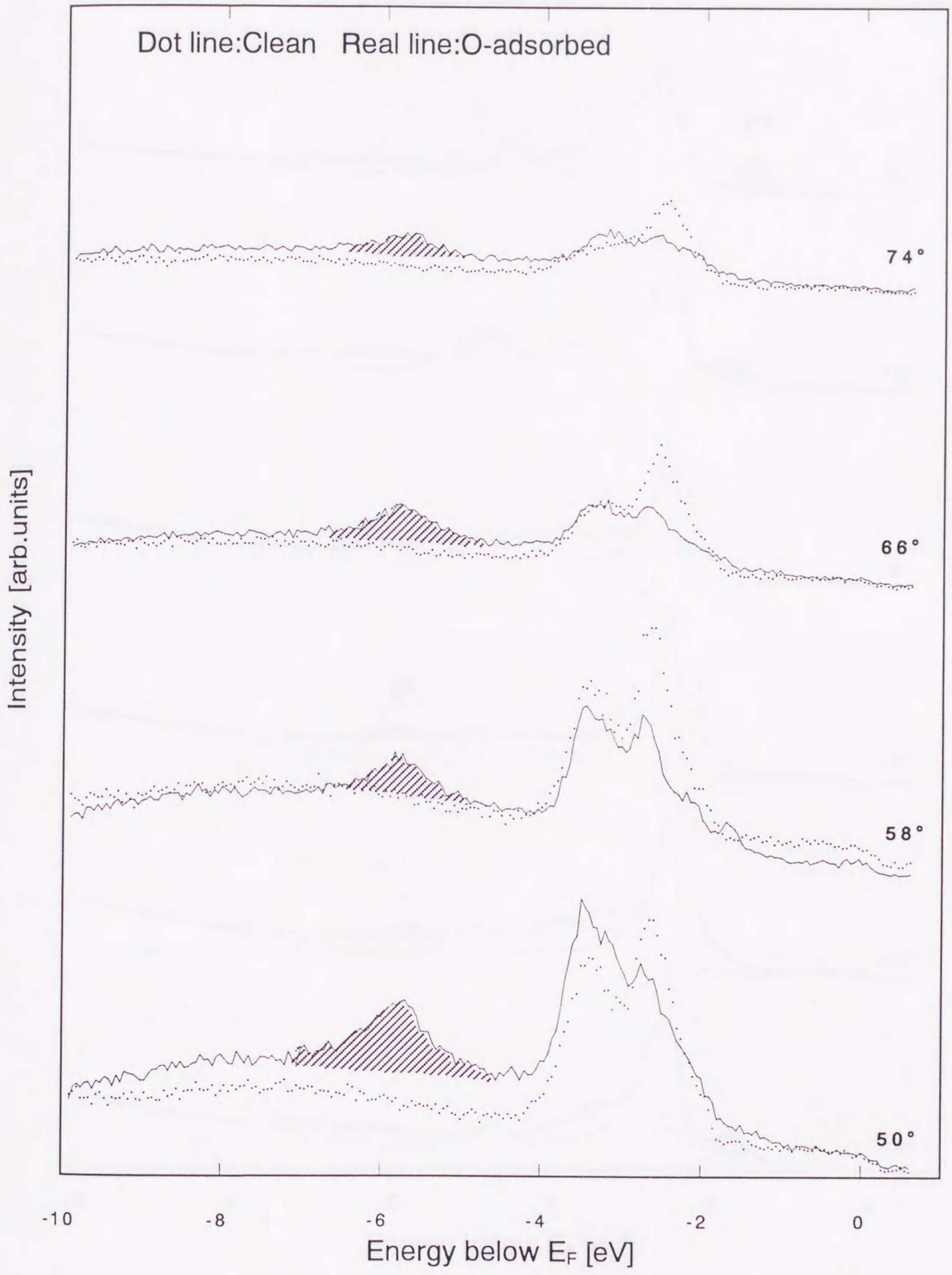

Figure 4-2(d). AREDCs measured using HeII radiation as a function of the emission angle θe (50°~74°) along the <$\bar{1}$10> direction ($\bar{\Gamma}$-$\bar{X}$).

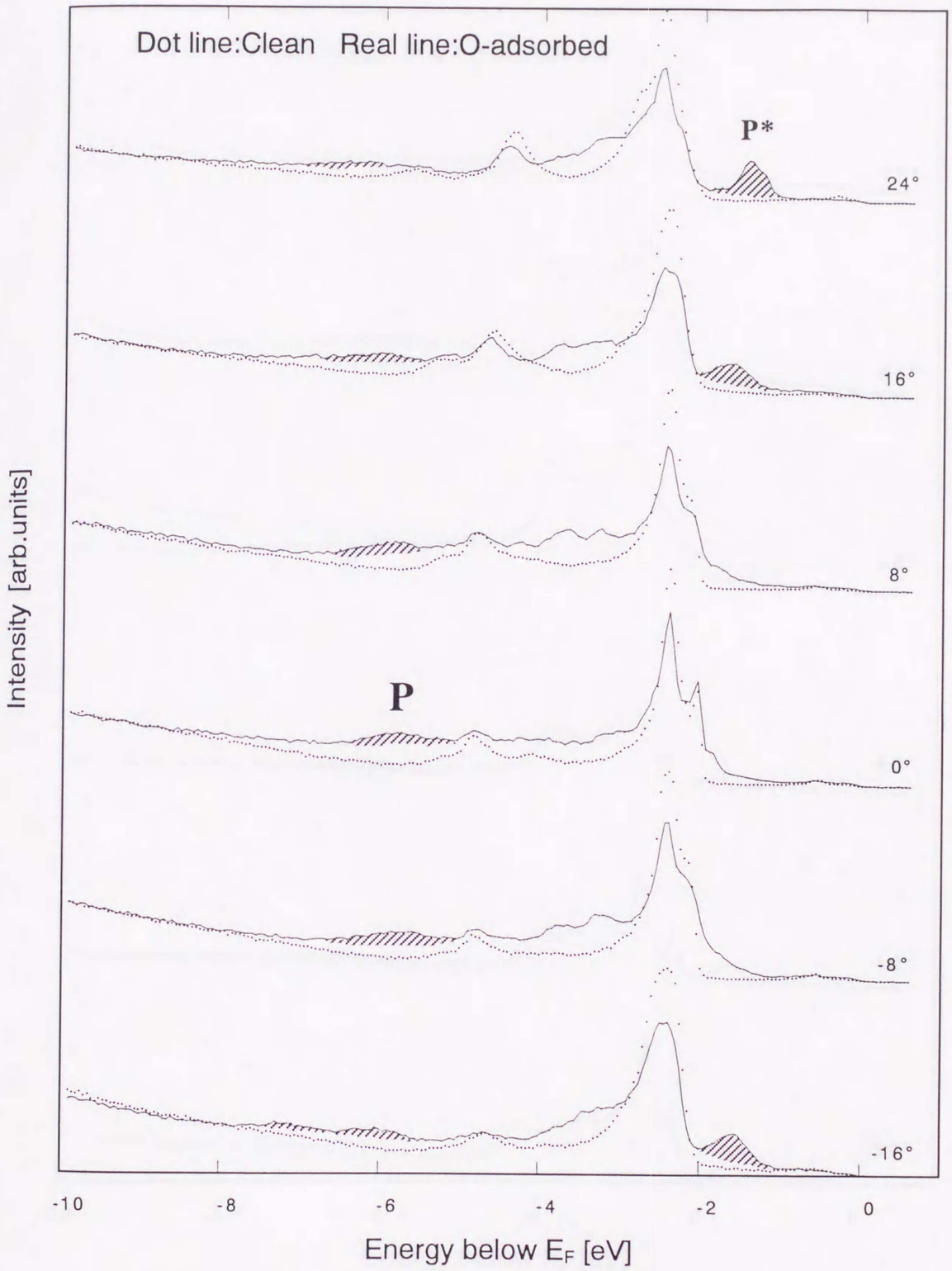

Figure 4-3(a). AREDCs measured using HeI radiation as a function of the emission angle θe (-16°~24°) along the <001> direction ($\bar{\Gamma}$-$\bar{Y}$). The shaded areas indicate the O-induced states.

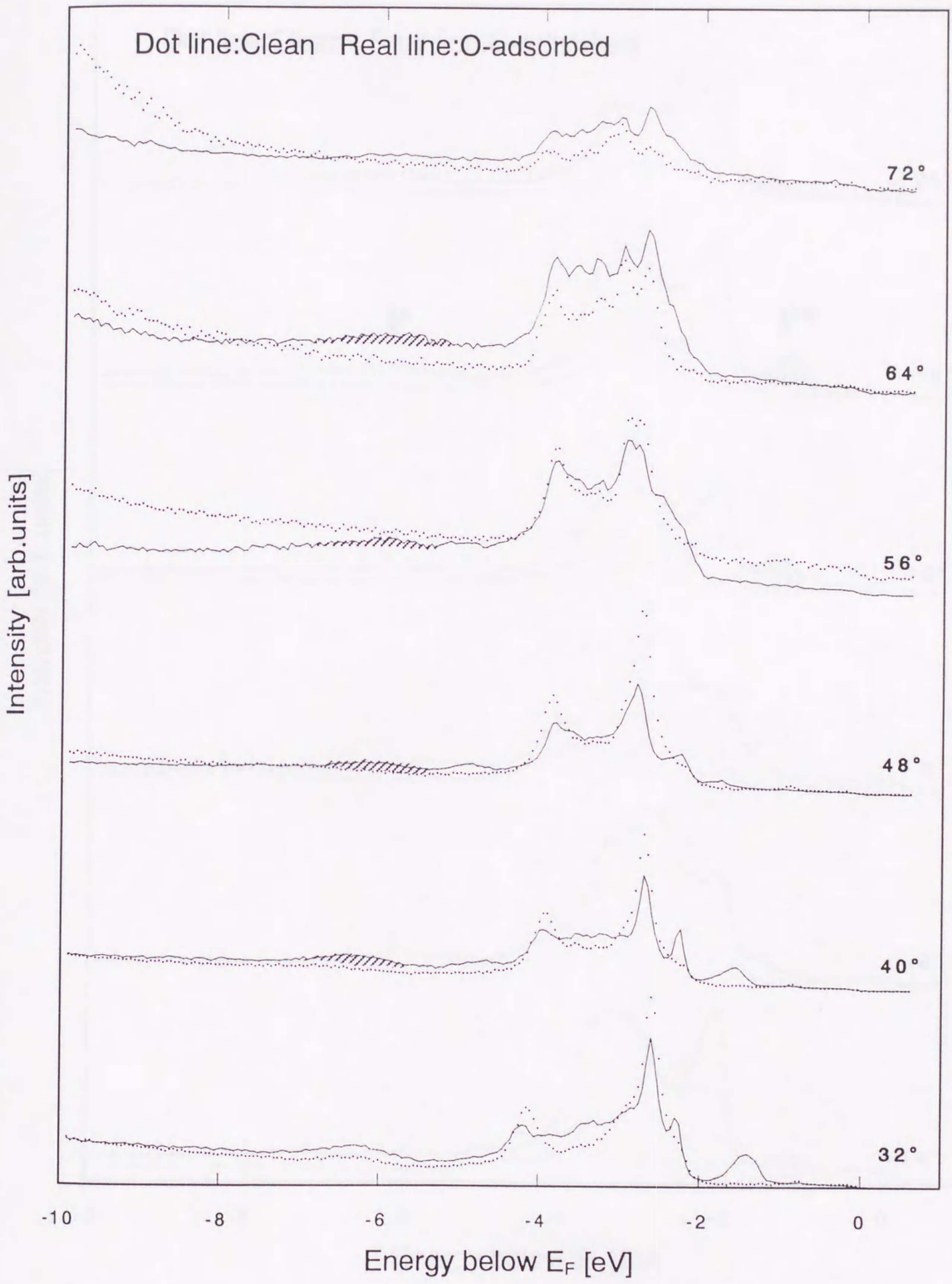

Figure 4-3(b). AREDCs measured using HeI radiation as a function of the emission angle θe (32°~72°) along the <001> direction ($\bar{\Gamma}$-$\bar{Y}$).

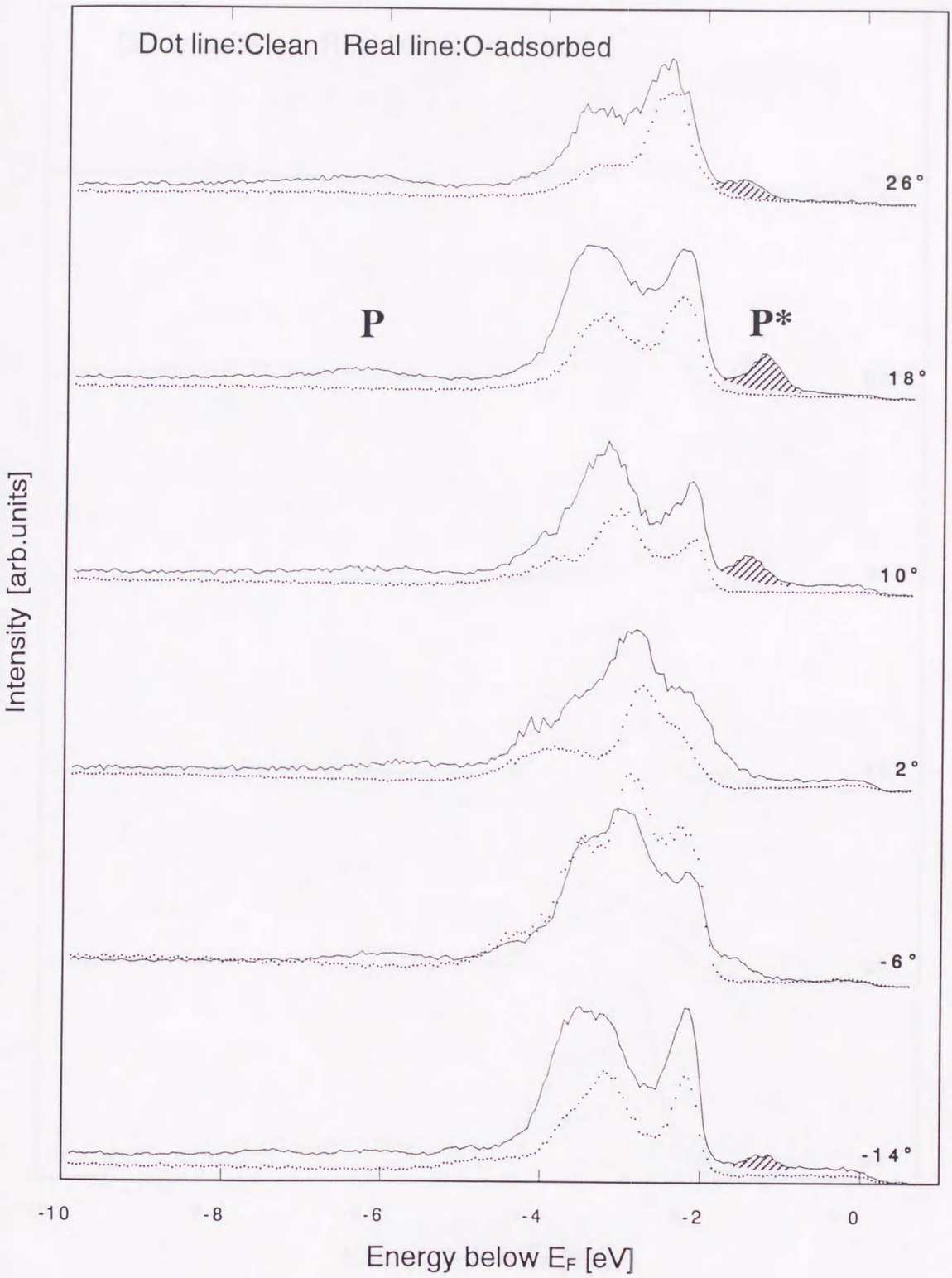

Figure 4-3(c). AREDCs measured using HeII radiation as a function of the emission angle θe (-14°~26°) along the <001> direction ($\bar{\Gamma}$-$\bar{Y}$).

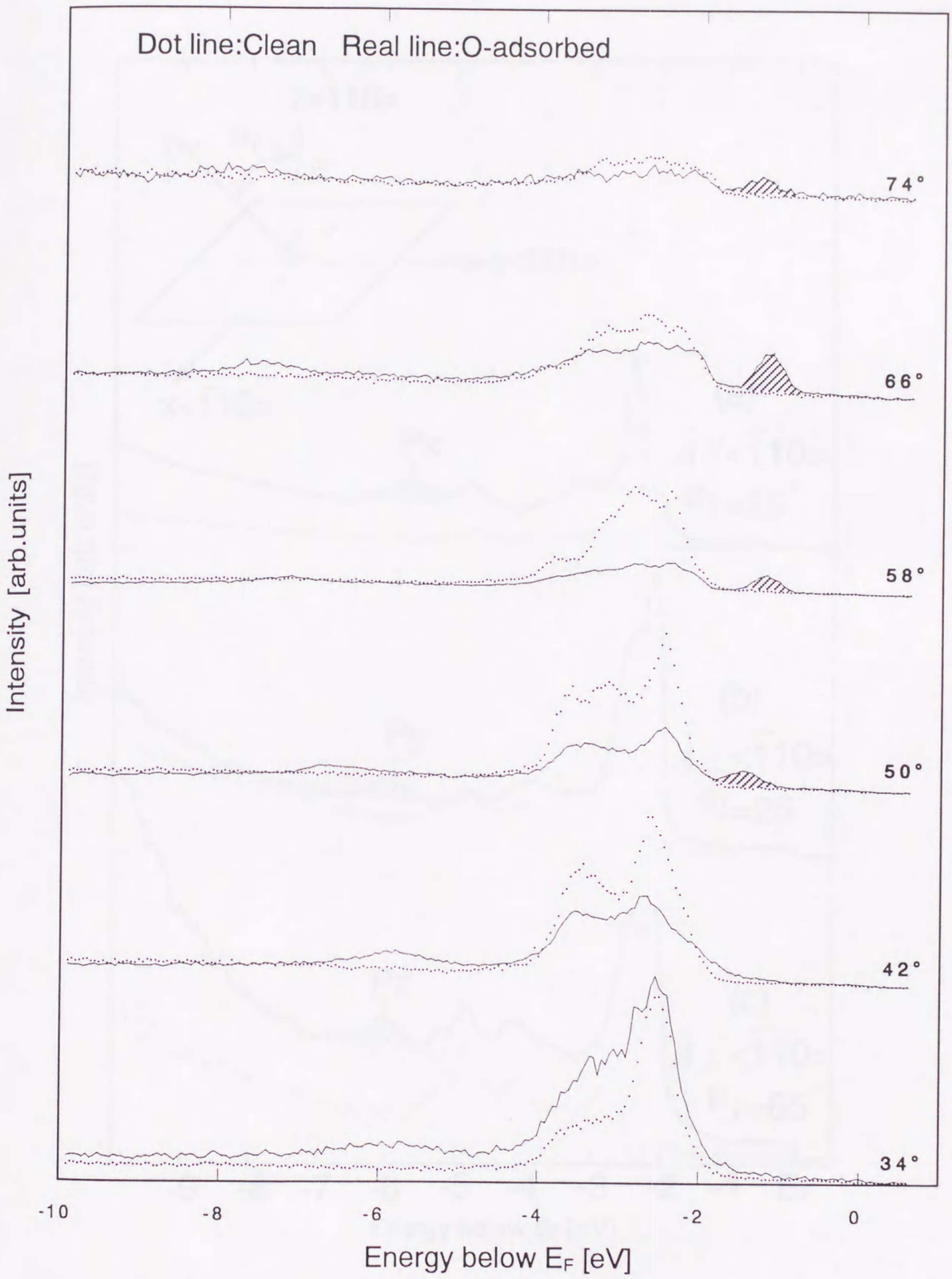

Figure 4-3(d). AREDCs measured using HeII radiation as a function of the emission angle θe (34°~74°) along the <001> direction ($\bar{\Gamma}$-$\bar{Y}$).

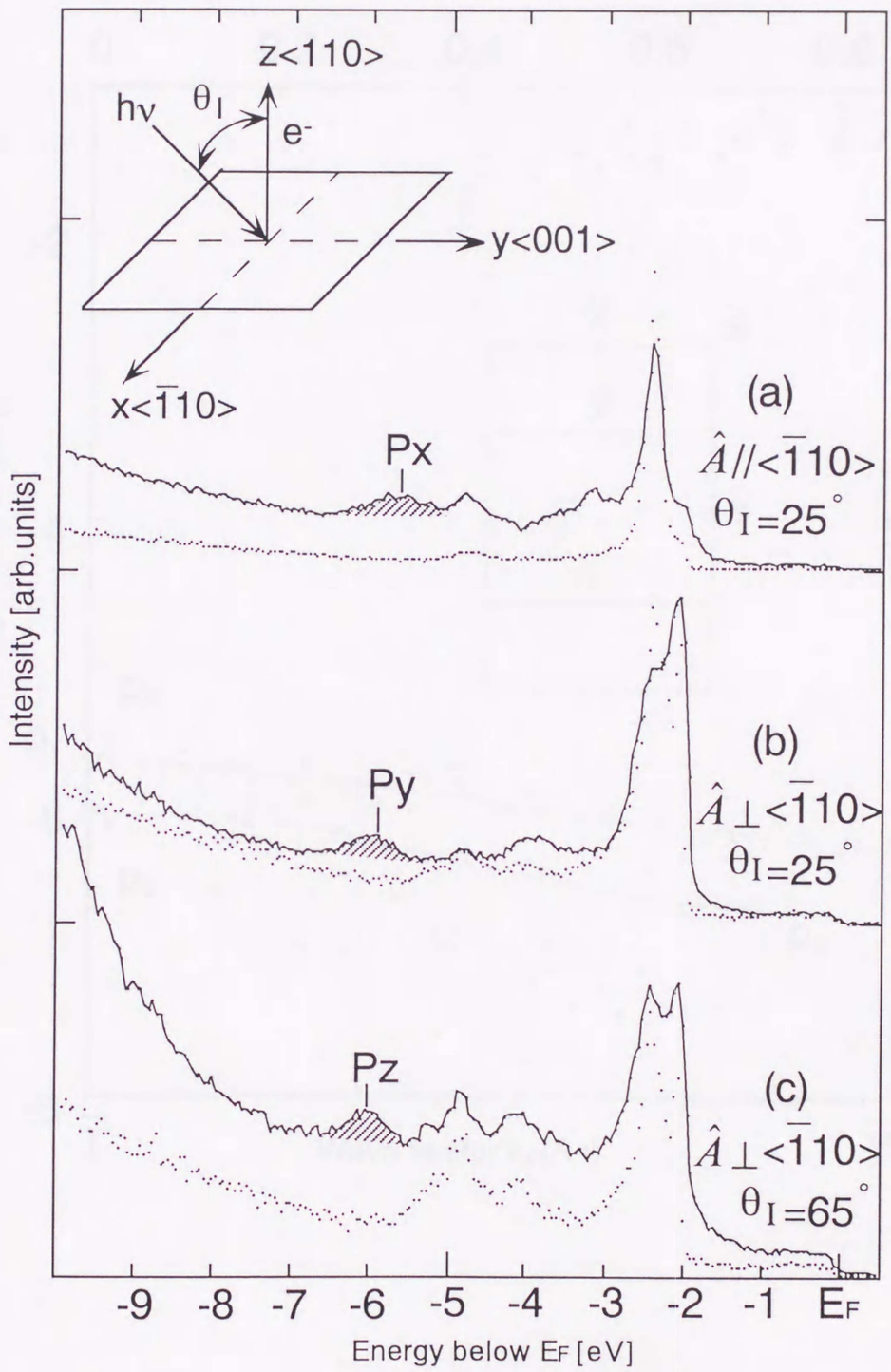

Figure 4-4. Normal emission EDCs of the clean and Cu(110)/2x1-O surfaces, using HeI radiation polarized parallel or perpendicular to <1̄10> direction: (a) $\hat{A}$ parallel to <1̄10> and θ_I=25° (b) $\hat{A}$ perpendicular to <1̄10> and θ_I=25° (c) $\hat{A}$ perpendicular to <1̄10> and θ_I=65°.

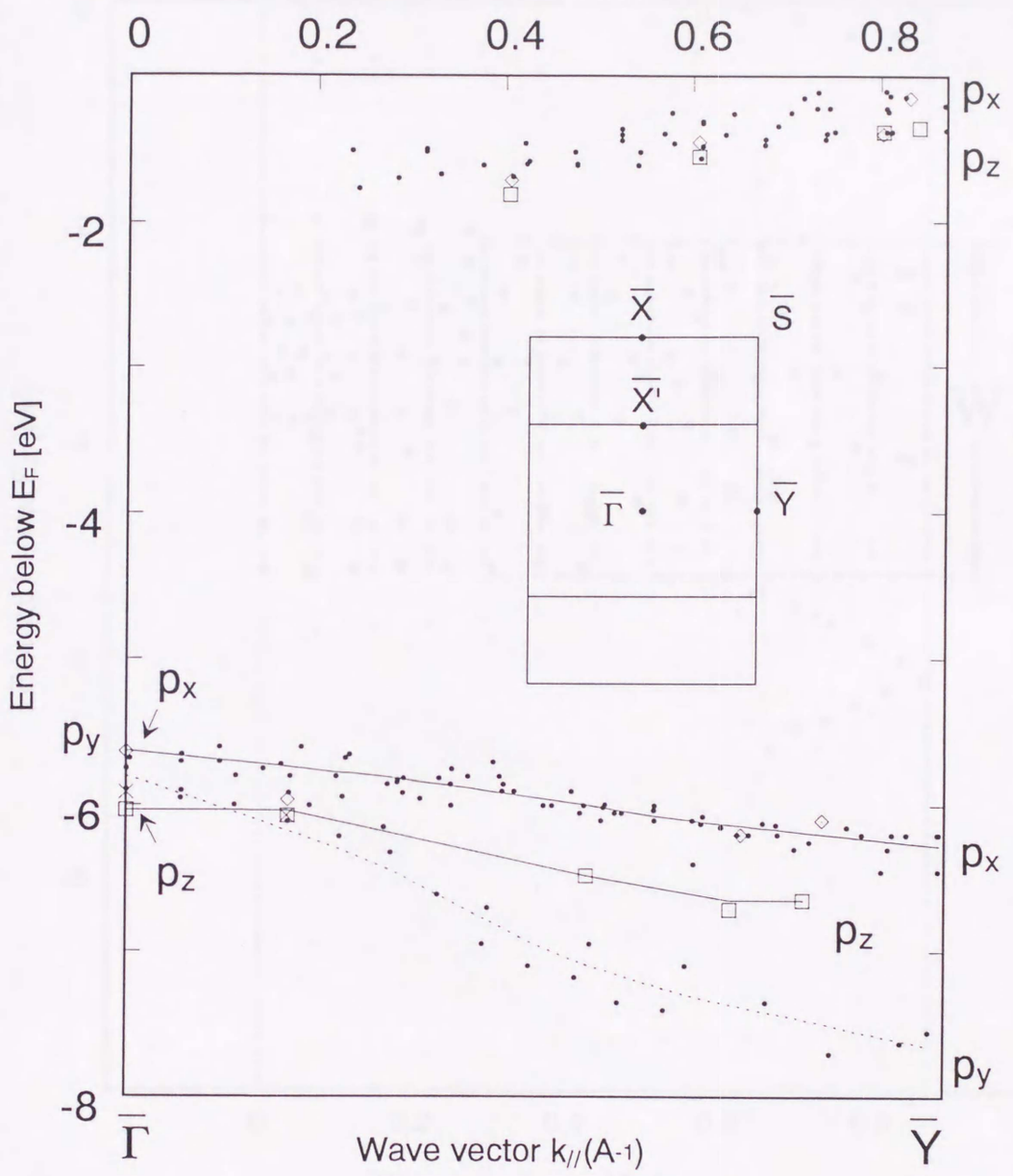

Figure 4-5. Energy dispersion along the <001> direction. Measurements were performed using unpolarized and linearly polarized HeI. Symbolic marks denote: (•) hν=21.22 eV and hν=40.8 eV, unpolarized; (◇) hν=21.22 eV, p_x feature; (×) hν=21.22 eV, p_y feature; (□) hν=21.22 eV, p_z feature.

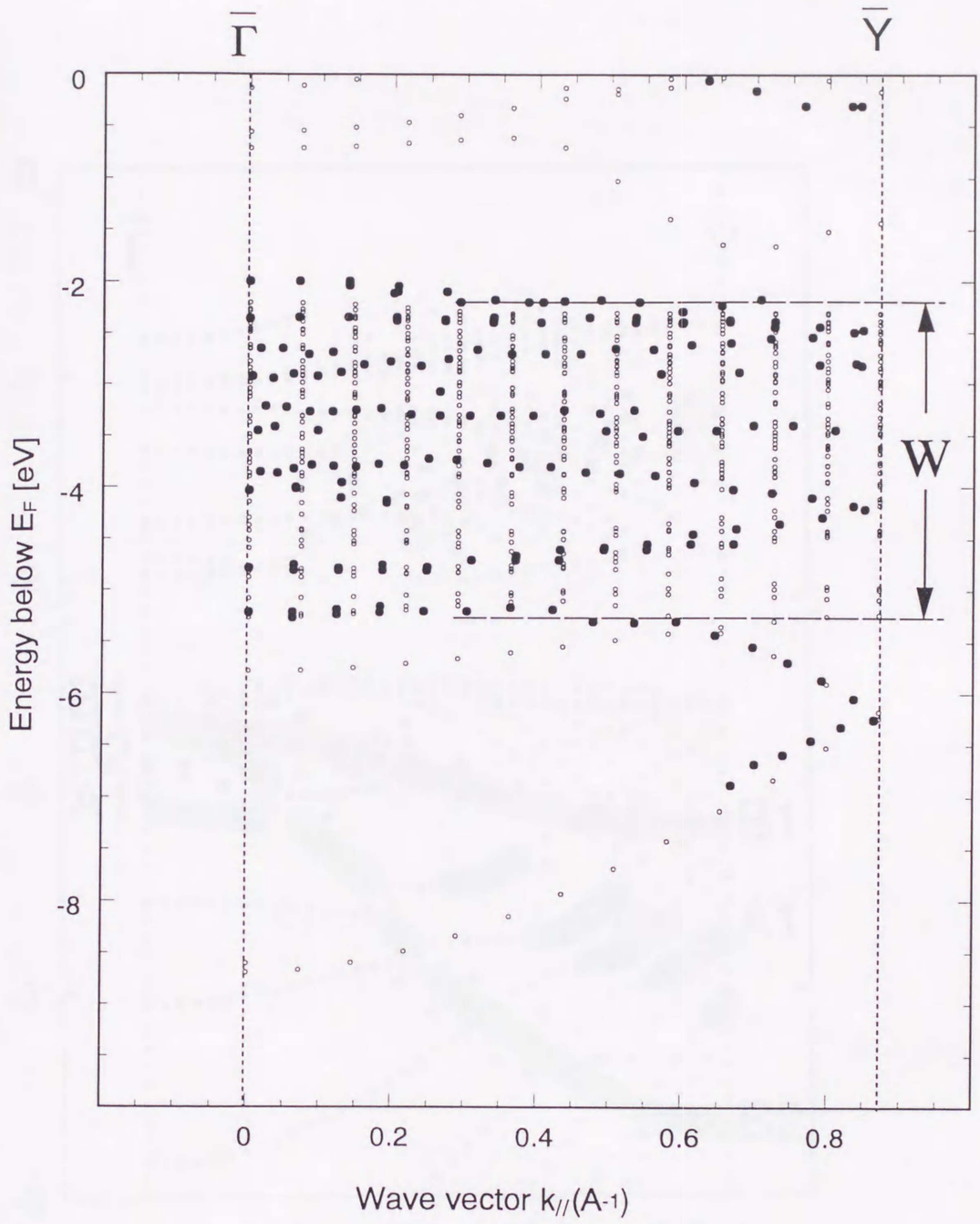

Figure 4-6. Calculation of the clean surface including 5 substrates along the <001> direction ($\bar{\Gamma}$-$\bar{Y}$) with the experimental energy bands of the clean surface in a reduced scheme. W, ● and ○ indicate the Cu *3d*-band width, the experimental results and the calculation results, respectively.

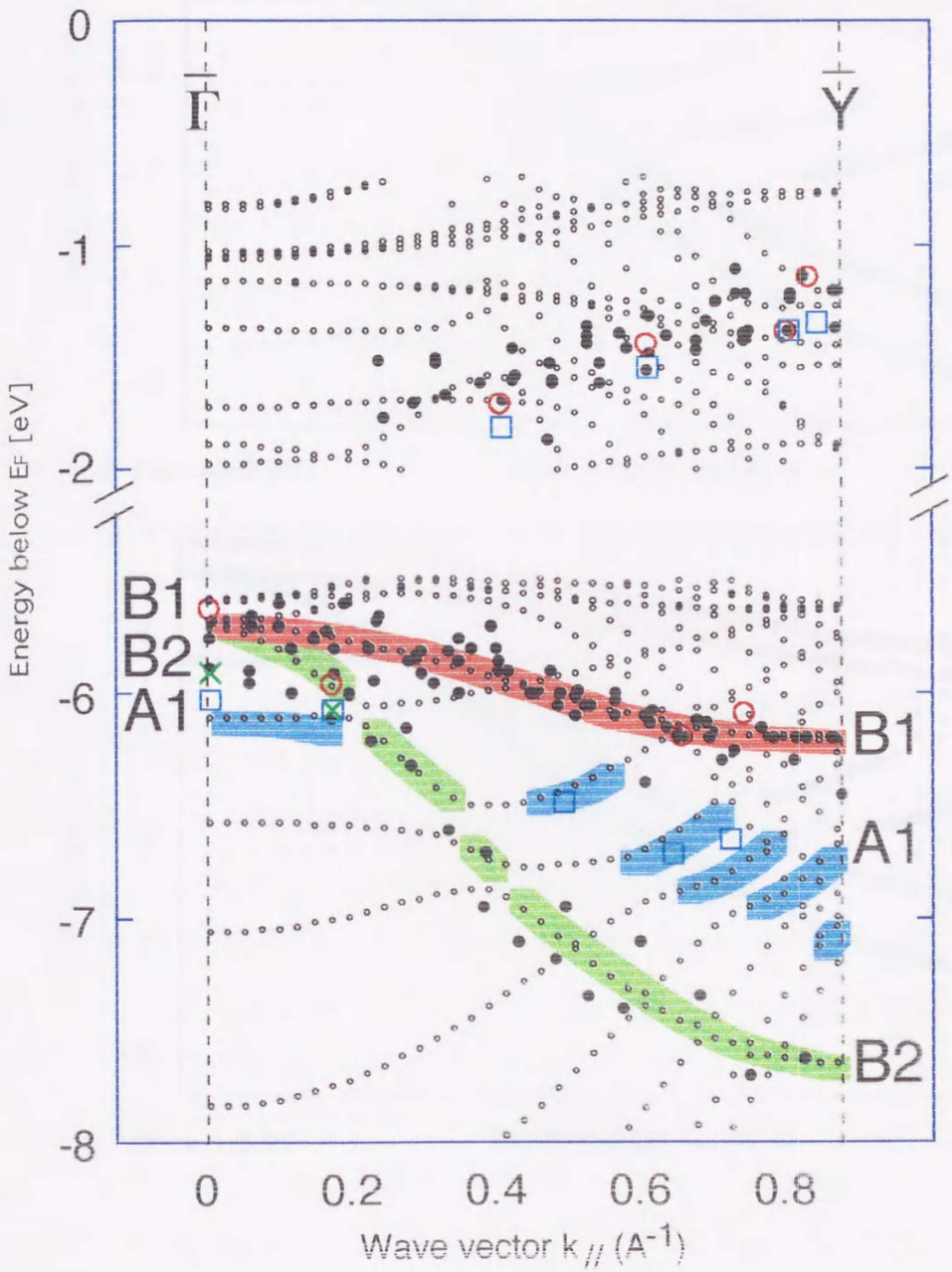

Figure 4-7. Plots of calculated energy bands along the <001> direction (denoted by open circles) compared with experimental points given in Fig.4-5. Each calculated band, p_x-band(B1), p_y-band(B2) and p_z-band(A1), is shaded for the purpose of easy recognition of the correspondence between calculated bands and experimental points. B2 band hybridizes with A1 band between $\bar{\Gamma}$ and $\bar{Y}$, and A1 band hybridizes with subsurface Cu*4s* bands around $\bar{Y}$.

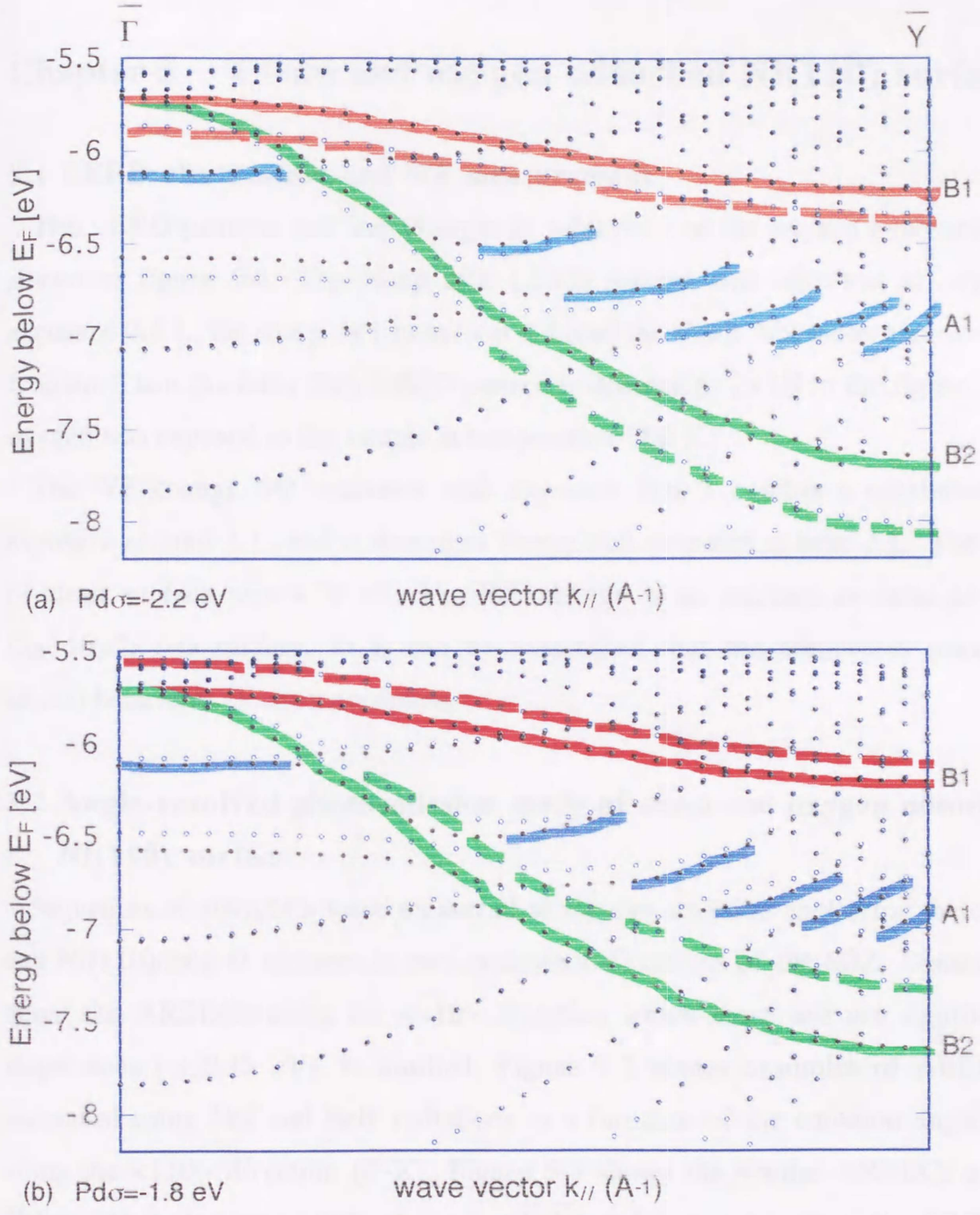

Figure 4-8. Energy bands by deviated parameters along the <001> direction ($\bar{\Gamma}$-$\bar{Y}$) in a reduced scheme. ● and ○ indicate the calculation bands of the definitive and deviated calculation, respectively.

Chapter 5 Clean and oxygen adsorbed Ni(110) surface

5.1 LEED observation and WF measurement

The LEED patterns and WF changes as a function of the oxygen exposure are shown in figure 5-1. The sharp 2x1 LEED pattern was observed at oxygen exposure 0.8 L, the sharp 3x1 pattern at 4 L and the sharp 2x1 pattern at over 10 L again. Then the latter 2x1 LEED pattern is denoted as 2x1H in the figure. The oxygen was exposed to the sample at temperature 700 K.

The WF change $\Delta\Phi$ increases with exposure and it reaches a maximum at exposure around 3 L, and it decreases slowly and saturated at over 3 L. The WF of clean surface was 4.76 eV. The WF change is an increase as same as the Cu(110)/2x1-O surface, so it can be considered that the adsorbates (oxygen atoms) behave as electron acceptors.

5.2 Angle-resolved photoemission study of clean and oxygen adsorbed Ni(110) surface

Sequences of AREDCs were measured at various emission angles for the clean and Ni(110)/2x1-O surfaces in two symmetry directions of the SBZ. Discussion about the AREDCs along the $<\bar{1}10>$ direction which there are not significant dispersions (± 0.15 eV), is omitted. Figure 5-2 shows examples of AREDCs measured using HeI and HeII radiations as a function of the emission angle θe, along the $<\bar{1}10>$ direction ($\bar{\Gamma}$-$\bar{X}$). Figure 5-3 shows the similar AREDCs using HeI and HeII along the <001> direction ($\bar{\Gamma}$-$\bar{Y}$). Solid curves indicate the AREDCs corresponding to of the Ni(110)/2x1-O surfaces, and dotted curves indicate that of the clean Ni(110) surface. The shaded areas in those figures indicate the new features appeared in the Ni(110)/2x1-O spectra. Because the features around -6 eV appeared by oxygen adsorption, and have a periodicity with the substrate reciprocal lattice, then they are assigned to oxygen-induced bonding states.

Figure 5-4 shows the normal emission EDCs of clean and Ni(110)/2x1-O

surfaces, using HeI radiation polarized parallel or perpendicular to <$\bar{1}$10> direction. As indicated in figure 5-4, the three features can be assigned to states with p_x, p_y and p_z symmetry from the polarization selection rule. The spectra were measured at three arrangements; (a) $\hat{A}$ parallel to <$\bar{1}$10> and θ_I=20° (b) $\hat{A}$ perpendicular to <$\bar{1}$10> and θ_I=20° (c) $\hat{A}$ perpendicular to <$\bar{1}$10> and θ_I=65° as shown in Fig.2.5. Then the p_x symmetry features were selectively appeared at arrangement (a), in the same way, mainly p_y at (b) and p_z at (c).

5.3 Simplified-LCAO calculation of Ni(110)/2x1,3x1-O surface

The simplified-LCAO calculation of Ni(110)/2x1-O surface was performed to compare with the experimental energy bands obtained from the features described in chapter 5.2. Figure 5-5 shows the calculation of Ni(110)/2x1-O surface together with the experimental results. The LCAO parameters for the Ni-Ni interactions were also adopted from the literature [34]. The Ni-O interactions, sPσ , pPσ , pPπ , Pdσ , Pdπ , surface shift and the on-site energy of O orbitals E_{Op} in table 2-2, were treated as adjustable parameters to fit the experimental results. The symbolic marks are same as in Fig.4-7. The open circles denote the calculated energy bands and each calculated band, which has dominantly p_x, p_y and p_z character, is shaded for the purpose of easy recognition of the correspondence between calculation and experiment. The states at energy less than -5 eV are ascribed to the Ni*3d* bands. The p_x, p_y and p_z states belong to B1, B2 and A1 irreducible representations of C_{2V} point group (see Chap.4.3), respectively. As similar as the case of Cu, B2 and A1 bands hybridize each other between $\bar{\Gamma}$ and $\bar{Y}$. The present calculation is satisfactory with such phenomena.

The energy band of Ni(110)/3x1-O surface obtained through the same procedure like of Ni(110)/2x1-O surface, is shown in figure 5-6 together with the simplified-LCAO calculation. The marks are same as in Fig.5-5. The p_x (B1) band shifts to the Fermi energy along the <001> direction ($\bar{\Gamma}$-$\bar{Y}$), and it has a dispersion of ~1 eV along the <$\bar{1}$10> direction ($\bar{\Gamma}$-$\bar{X}$) in contrast to no dispersion

of the Ni(110)/2x1-O surface energy band. The O-O interatomic length along the $<\bar{1}10>$ direction becomes shorter enough to bond each other than that of Ni(110)/2x1-O surface as indicated in figure 5-7. So new parameters PPσ and PPπ were added as adjustable parameters, where PPσ and PPπ are the O-O interactions. The present calculation can reproduce the p_x band dispersion which is characteristic only for the Ni(110)/3x1-O surface. Furthermore, the E_{Op} for the Ni(110)/3x1-O surface shifted close to the Fermi energy.

The calculation can reproduce the characteristic p_x band of Ni(110)/ 3x1-O surface. Modifications of the 2x1 to 3x1 surface are an addition of the O-O interaction and a revision of E_{Op}. The dispersion of ~1 eV along the $<\bar{1}10>$ direction is ascribed to the addition of O-O interaction. This is consistent with that there are only O-O interactions along the $<\bar{1}10>$ direction due to adjacent Ni-O chains as a new bonding of the Ni(110)/3x1-O surface compared with of the Ni(110)/2x1-O surface. The p_x band shift between $\bar{\Gamma}$ and $\bar{Y}$ is ascribed to the revision of E_{Op}. As the p_x band obtained by measurement shifts ~1 eV to E_F, E_{Op} shifts 0.3 eV to E_F.

Now suppose a bonding of two orbitals denoted by m and n located on adjacent atoms (at $\vec{R}_i$ and $\vec{R}_j$) in a same row along the <001> or $<\bar{1}10>$ direction. And assume there are only m and n orbitals for the simplification. The interaction of $\phi_m(\vec{R}_i)$ and $\phi_n(\vec{R}_j)$, where ϕ is an atomic function, is given by equation (2-23, 31 and 32):

$$H = \exp\left\{i \cdot \vec{k} \cdot (\vec{R}_j - \vec{R}_i)\right\} \cdot \begin{pmatrix} E_m & E_{mn} \\ E_{nm} & E_n \end{pmatrix} \quad , \qquad (6\text{-}3)$$

where E_m, E_n are the on-site energies (one-center integral) and $E_{mn}(= E_{nm})$ is the interaction (two-center integral). The relation: $H_{mn}=H_{nm}^*$ is obvious when $E_{mn}(= E_{nm})$ is real. Then this eingenvalues can be solved as, assuming $E_{mn} << E_m, E_n$:

$$E = E_m + \exp\left\{i \cdot \vec{k} \cdot (\vec{R}_i - \vec{R}_j)\right\} \cdot \frac{E_{mn}^2}{E_m - E_n} \quad ;$$

$$\text{or } E_n + \exp\left\{i \cdot \vec{k} \cdot (\vec{R}_i - \vec{R}_j)\right\} \cdot \frac{E_{mn}{}^2}{E_n - E_m} \quad , \qquad (6\text{-}4)$$

The term of exp. becomes 1 when $\vec{k}$ =0 (at $\overline{\Gamma}$) and -1 when $\vec{k}$ has a half length of the reciprocal lattice vector (at $\overline{X}$ or $\overline{Y}$). So the first term corresponds to an energy with respect to the bottom of the valence band, and the second term corresponds to a dispersion width.

This can represent the new dispersion of p_x band along the <$\overline{1}$10> direction ($\overline{\Gamma}$-$\overline{X}$), and the bands shift to E_F on the whole. Not only p_x (B1) band but p_y (B2) and p_z (A1) band shifts were observed. The parameters are listed in table 5-1.

5.4 High-exposed Ni(110)/2x1-O surface

The energy bands of the oxygen induced features of the high-exposed Ni(110)/2x1-O surface are shown in figure 5-8(a). The WF change at saturated area as in Fig.5-1 is almost equal to that of the low-exposed Ni(110)/2x1-O surface. This energy band is almost identical to that of the low-exposed Ni(110)/2x1-O surface (see Fig.5-8(b)). Figure 5-9 shows the O*1s* XPS EDC of the high-exposed Ni(110)/2x1-O surface together with those of the low-exposed Ni(110)/2x1-O and Ni(110)/3x1-O surfaces. The EDC of the high-exposed Ni(110)/2x1-O surface is in good agreement with that of the low-exposed Ni(110)/2x1-O surface. This indicates the oxygen coverages of the high and low-exposed Ni(110)/2x1-O surfaces are the same, i.e. 1/2 ML. And the oxygen coverage of the Ni(110)/3x1-O surface is 2/3 ML. Then these indicate the continued oxygen exposure brings a reconstruction like 2x1 → 3x1 → 2x1H with the oxygen coverage 1/2 → 2/3 → 1/2 ML, respectively. This coverage conversion of 2/3 → 1/2 ML may be explained by two possibilities, i.e., the penetration into the bulk or the desorption from the surface. The former is questionable. The subsurface oxygen should be detected because the mean free path of the photoelectrons from O*1s* is about 12 Å corresponding to about 10 substrate layers. The latter may be plausible because the Ni(110)/3x1-O surface is more unstable than the Ni(110)/2x1-O surface [35]. However, it may need more studying to reveal the origin for example; whether the 2x1H → 3x1 transition is observed with more oxygen exposure, to determine the structure of 2x1H by XRD, STM and so on, and to observe the surface of the 3x1 → 2x1H transition process with the oxygen exposure by STM.

Table 5-1 : LCAO parameters of Ni(110)/2x1-O and 3x1-O surfaces

	(nn)	(nnn)	[eV]
[Ni-O and O-O two-center integrals]			
sPσ	1.50	0.30	
pPσ	3.25	0.65	
pPπ	-0.50	-0.10	
Pdσ	-2.80	-0.28	
Pdπ	1.20	0.12	
PPσ	0.50		
PPπ	-0.125		
[Ni-Ni two-center integrals]			
ssσ	-1.2959	-0.0088	
spσ	1.9052	0.1961	
ppσ	2.9633	0.8463	
ppπ	0.2259	0.0928	
sdσ	-0.5279	-0.1381	
pdσ	-0.5987	-0.1377	
pdπ	0.3234	0.0694	
ddσ	-0.5050	-0.0886	
ddπ	0.3577	0.0468	
ddδ	-0.0816	-0.0037	
[On-site energies from E_F and Surface Shift (ss)]			
E_{Op} =	-3.3 for 2x1-O, -3.0 for 3x1-O		
Surface shift (ss) =	1.5		
Ep =	12.7491		
Es =	6.6182		
Ed1 =	-1.4715		
Ed2 =	-1.5144		

(nn) and (nnn) denote a nearest-neighbor and a next-nearest-neighbor Slater- Koster two-center integrals, respectively. The letter s,p,d,P denote the Ni *4s,4p,3d* and O*2p* orbitals, respectively. Notations of the on-site energies are same as in table 2-2.

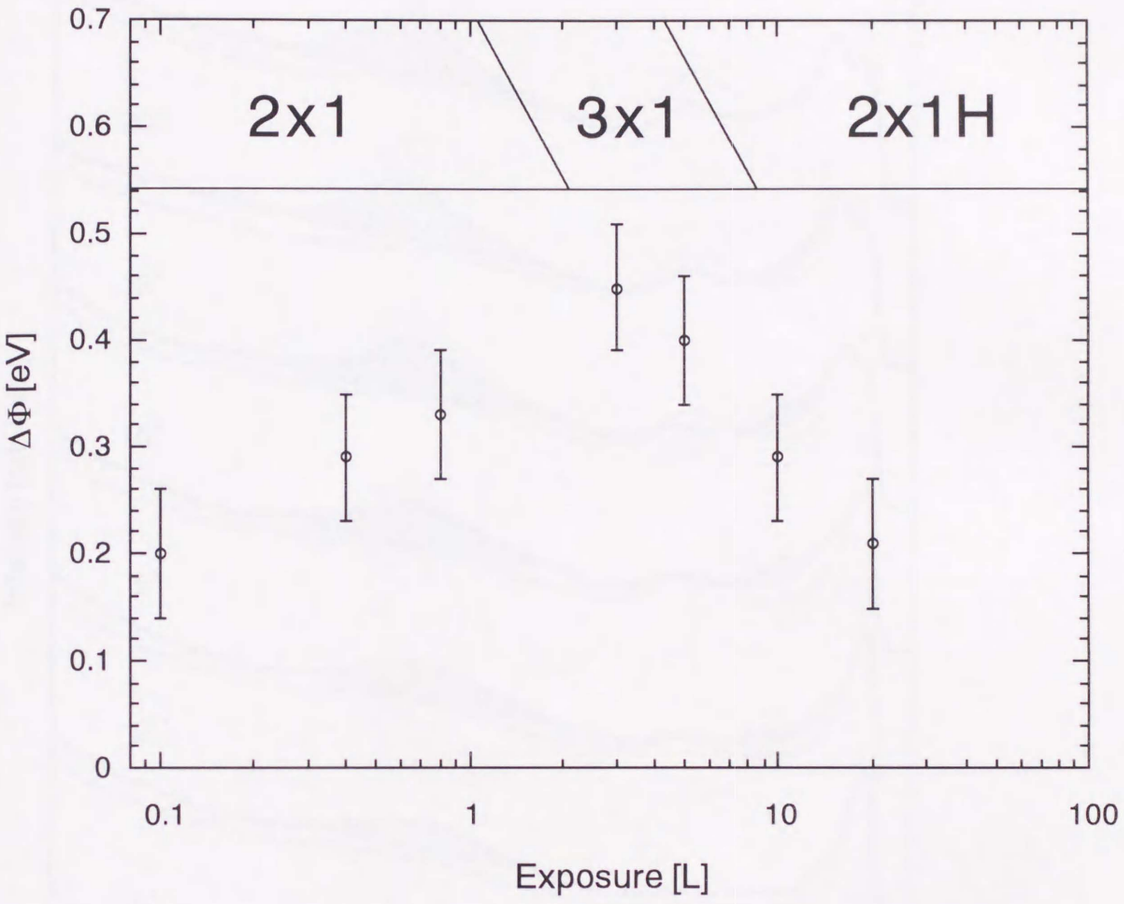

Figure 5-1. LEED patterns and the work function changes as a function of the oxygen exposure. The WF change is a difference between the clean and oxygen adsorbed Ni(110) surface WFs.

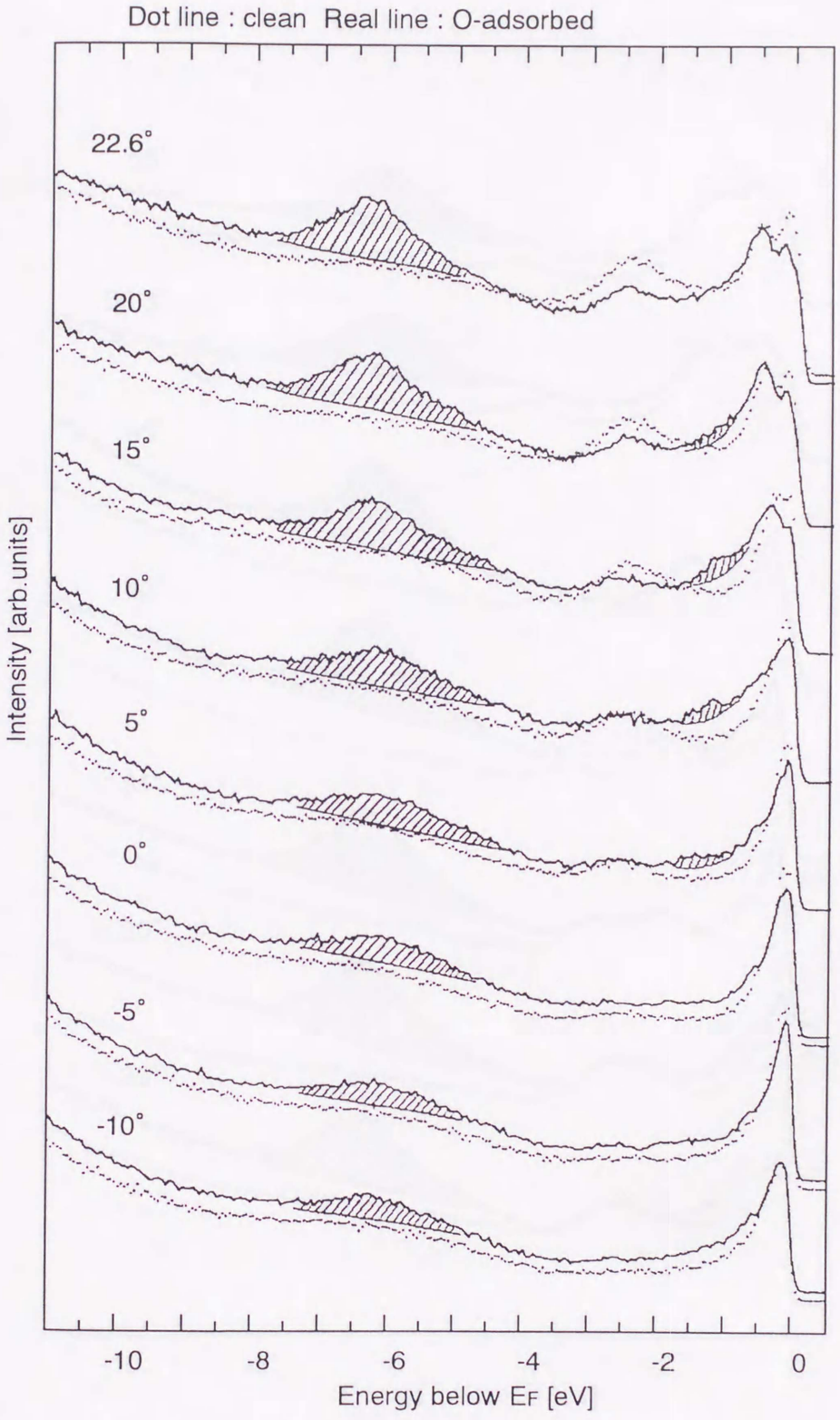

Figure 5-2(a). AREDCs measured using HeI radiation as a function of the emission angle θe (-10°~22.6°) along the <$\bar{1}$10> direction ($\bar{\Gamma}$-$\bar{X}$). The shaded areas indicate the O-induced states.

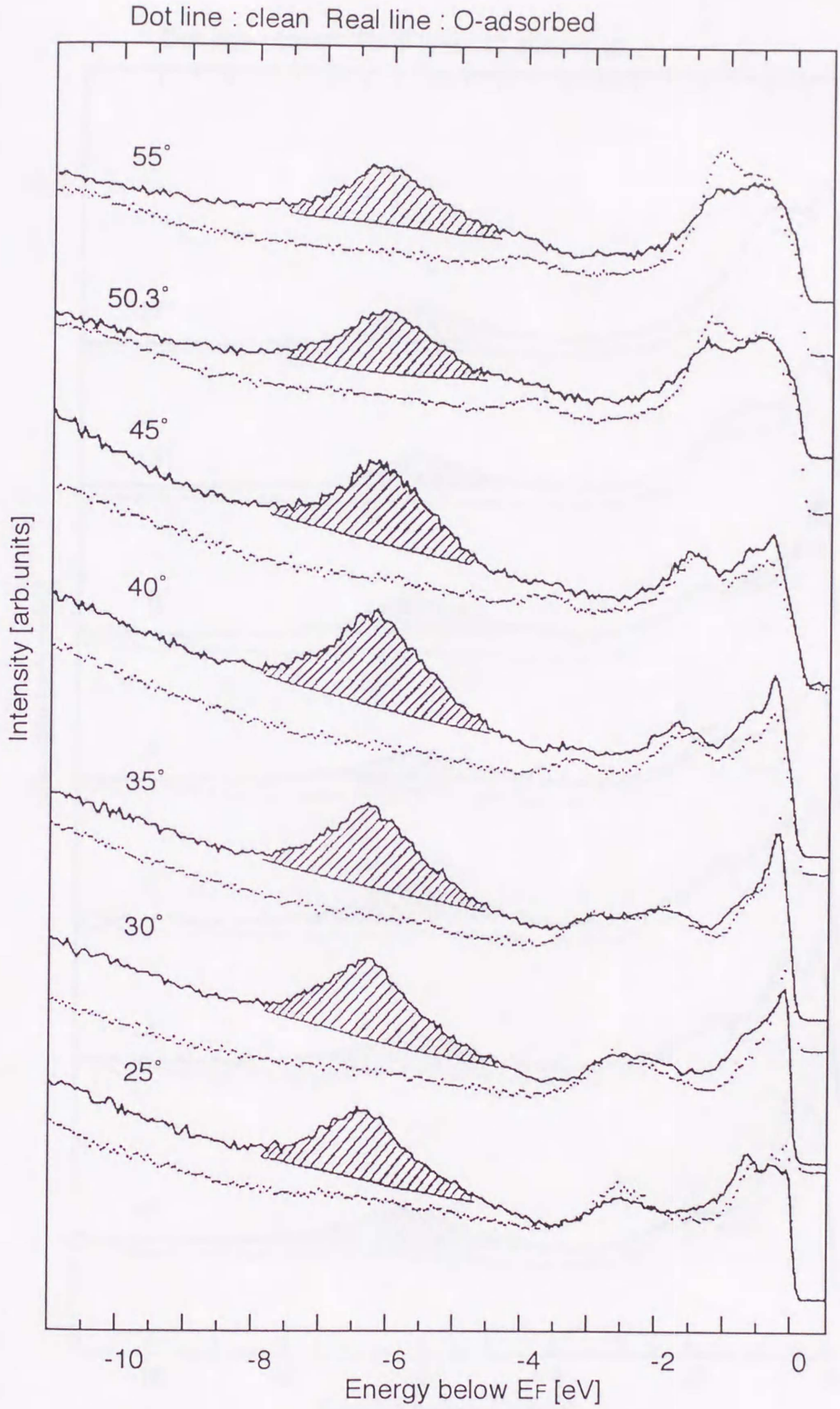

Figure 5-2(b). AREDCs measured using HeI radiation as a function of the emission angle θe (25°~55°) along the <$\bar{1}$10> direction ($\bar{\Gamma}$-$\bar{X}$). The shaded areas indicate the O-induced states.

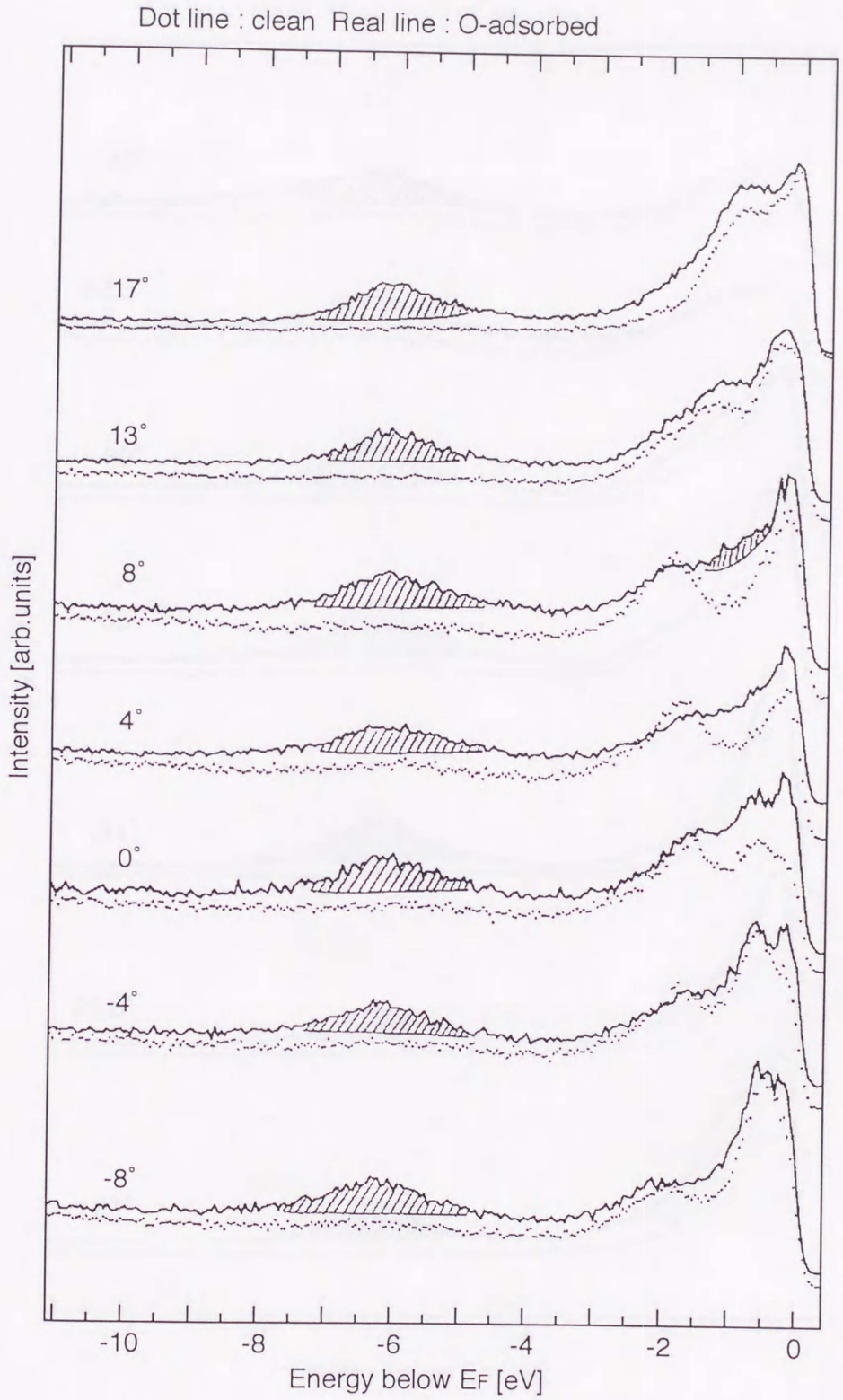

Figure 5-2(c). AREDCs measured using HeII radiation as a function of the emission angle θe (-8°~17°) along the $<\bar{1}10>$ direction ($\bar{\Gamma}$-$\bar{X}$).

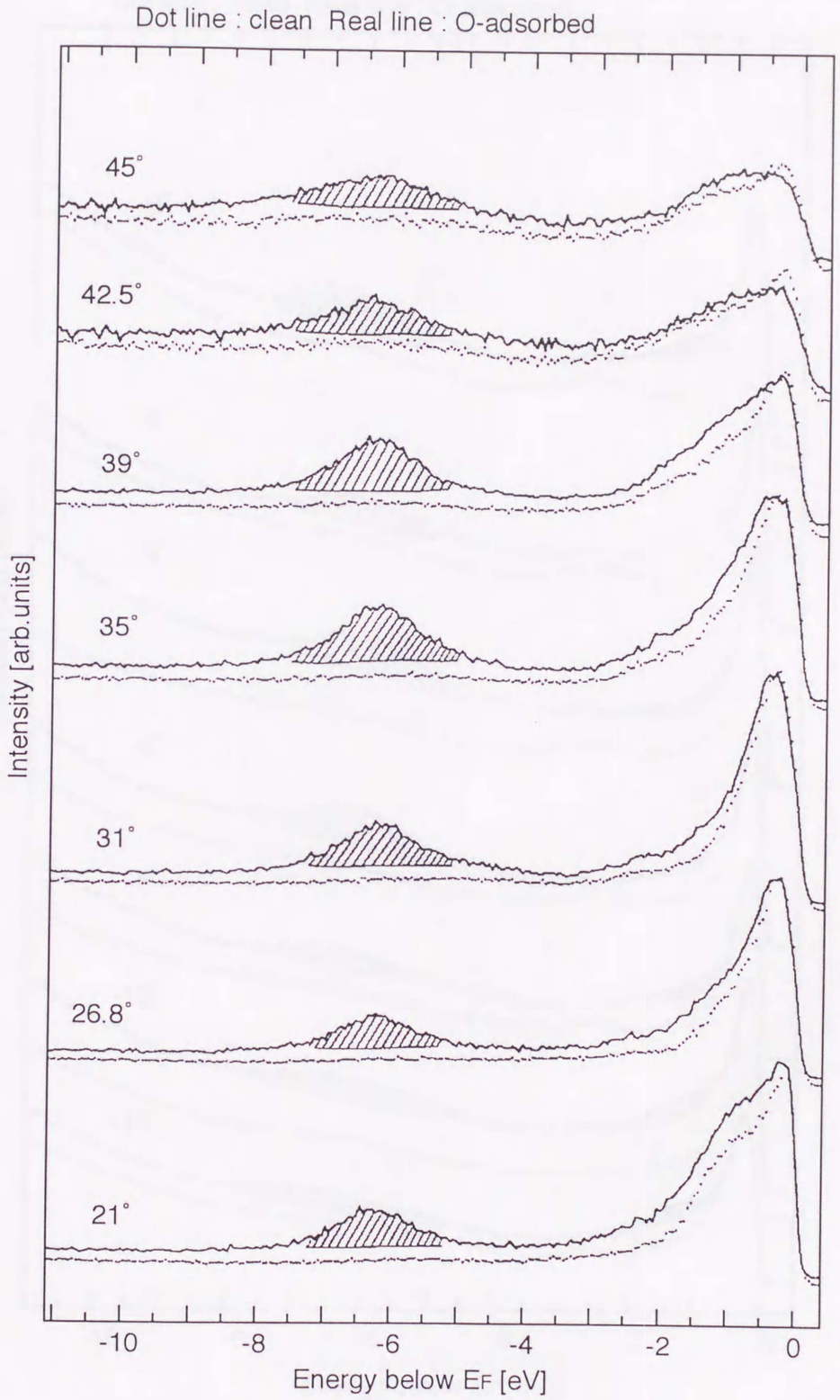

Figure 5-2(d). AREDCs measured using HeII radiation as a function of the emission angle θe (21°~45°) along the $<\bar{1}10>$ direction ($\bar{\Gamma}$-$\bar{X}$).

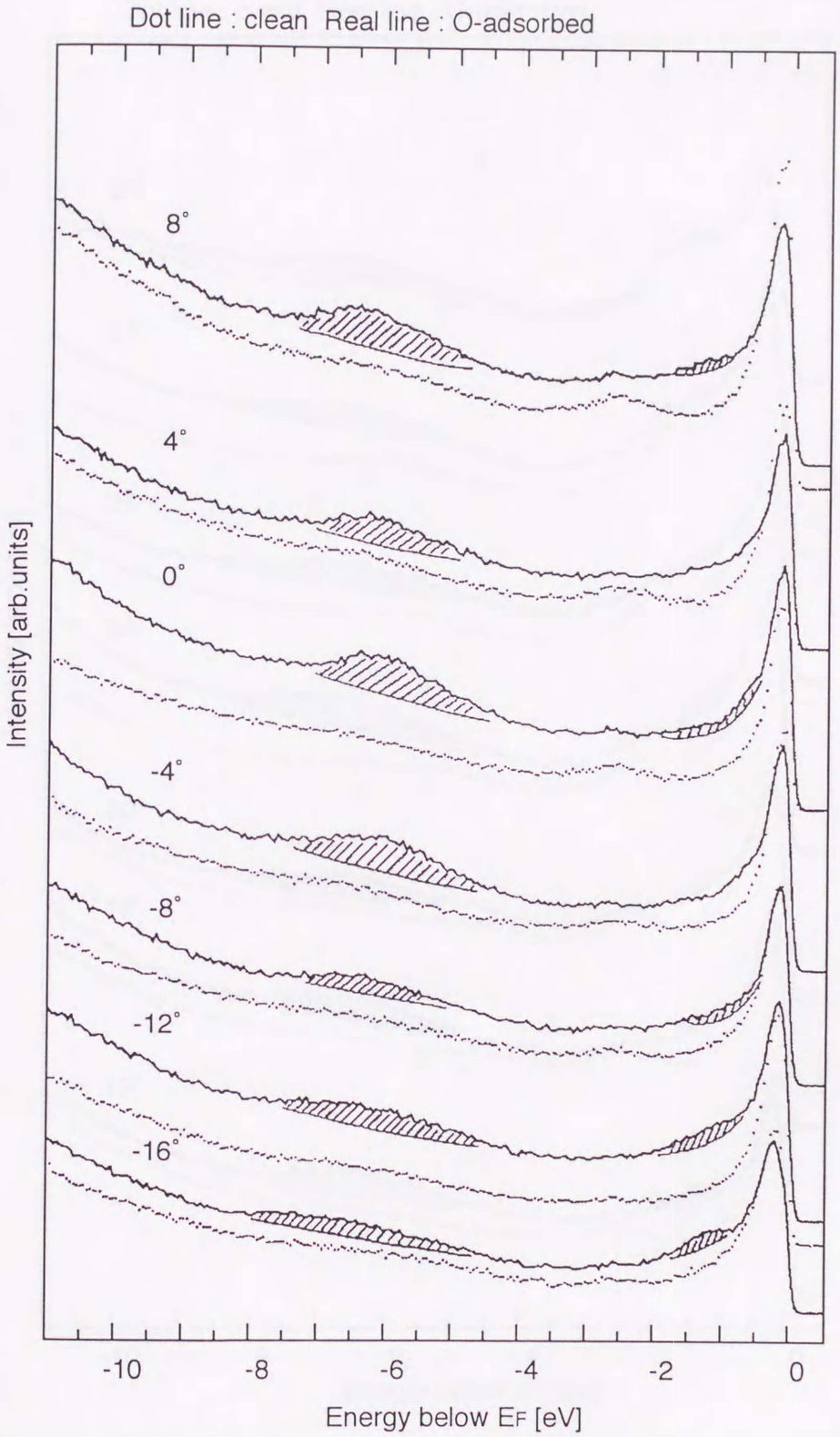

Figure 5-3(a). AREDCs measured using HeI radiation as a function of the emission angle θe (-16°~8°) along the <001> direction ($\overline{\Gamma}$-$\overline{Y}$). The shaded areas indicate the O-induced states.

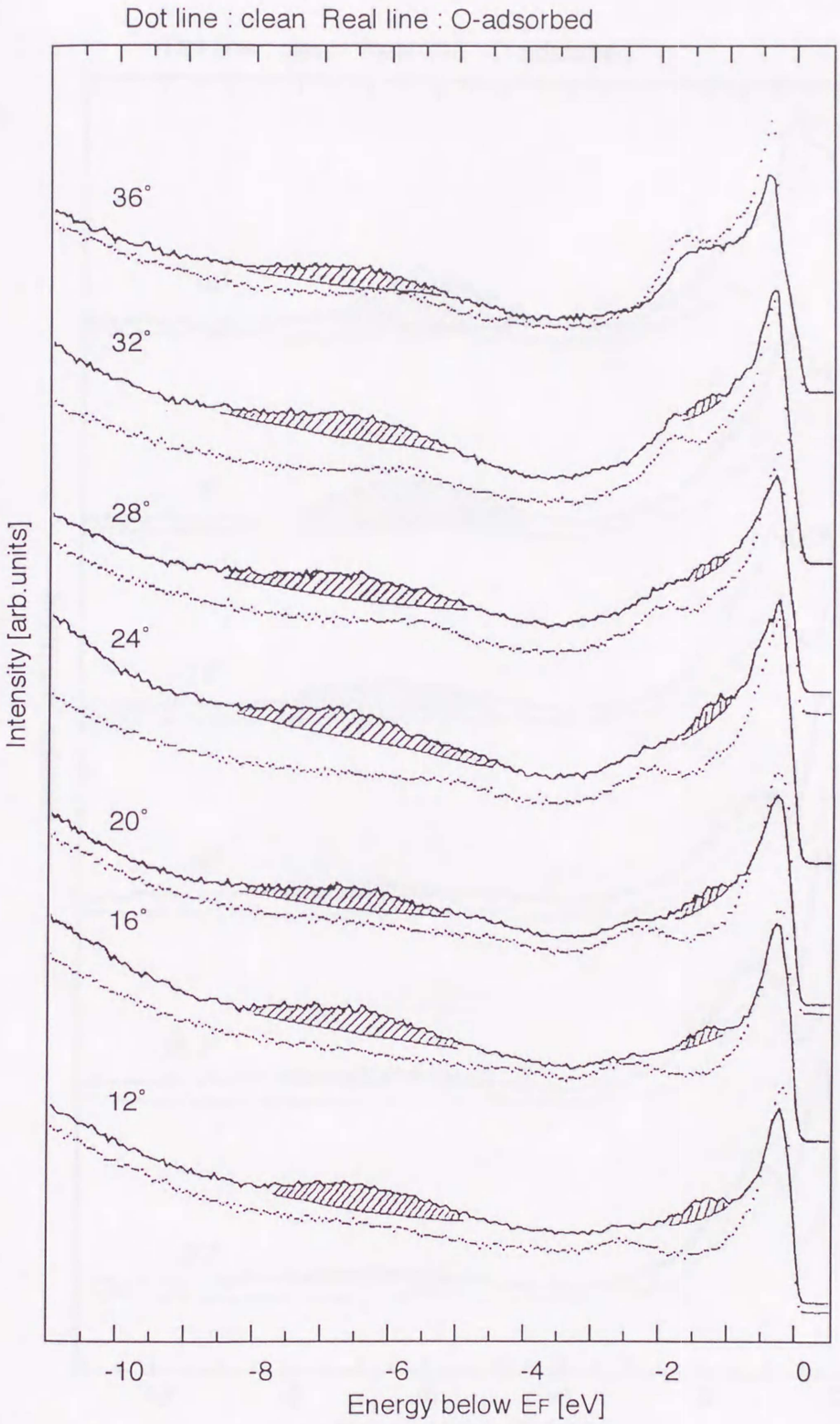

Figure 5-3(b). AREDCs measured using HeI radiation as a function of the emission angle θe (12°~36°) along the <001> direction ($\bar{\Gamma}$-$\bar{Y}$).

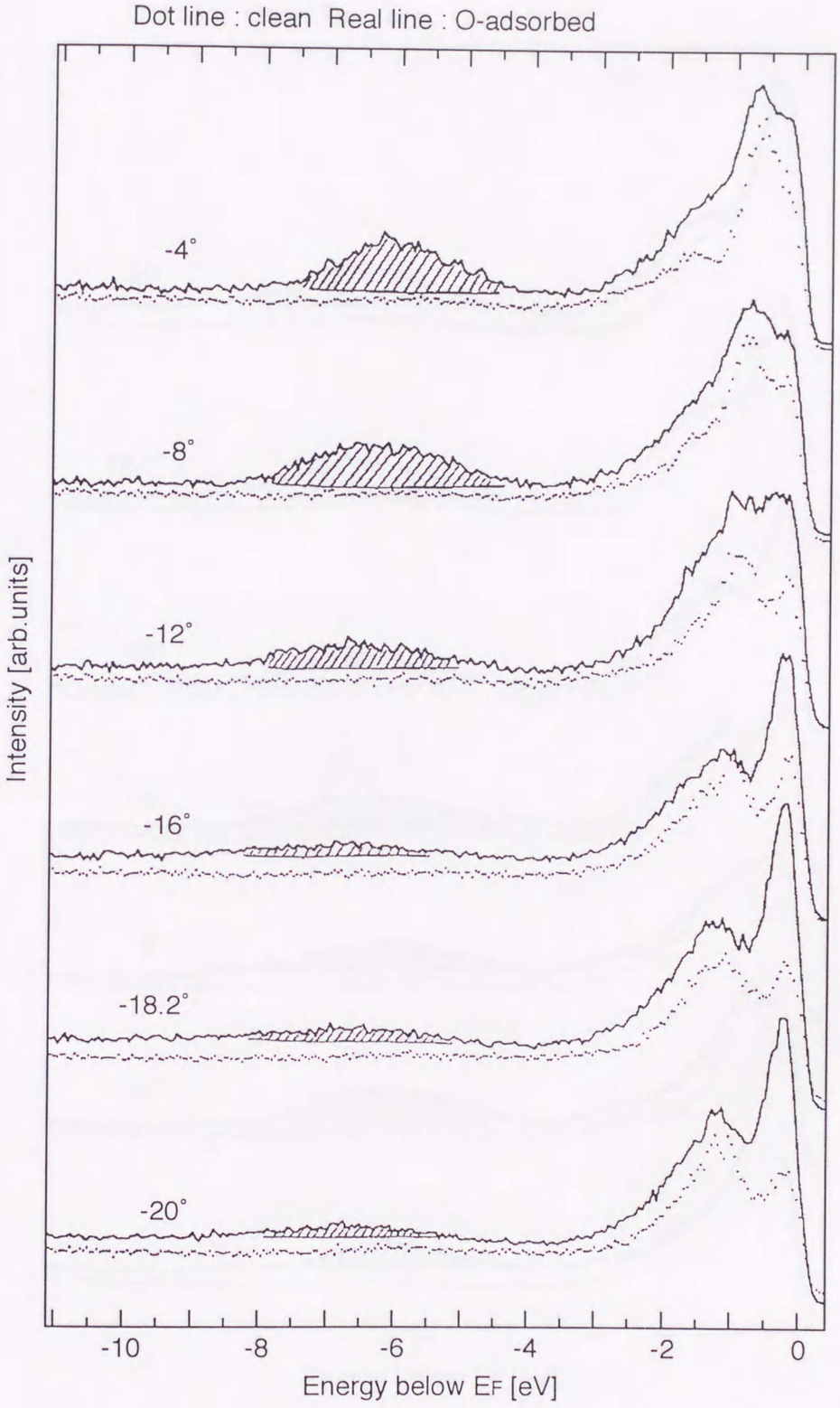

Figure 5-3(c). AREDCs measured using HeII radiation as a function of the emission angle θe (-20°~-4°) along the <001> direction ($\overline{\Gamma}$-$\overline{Y}$).

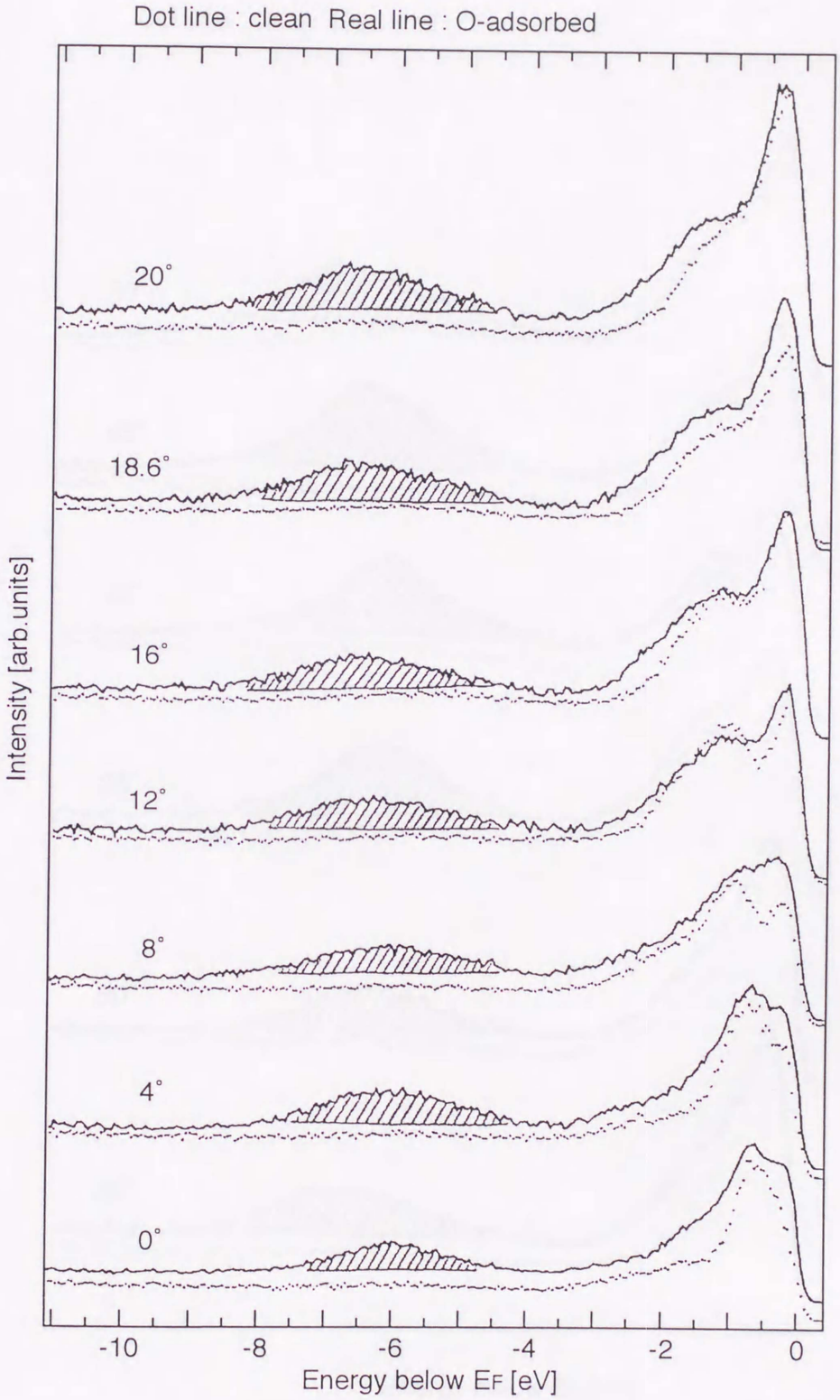

Figure 5-3(d). AREDCs measured using HeII radiation as a function of the emission angle θe (0°~20°) along the <001> direction ($\bar{\Gamma}$-$\bar{Y}$).

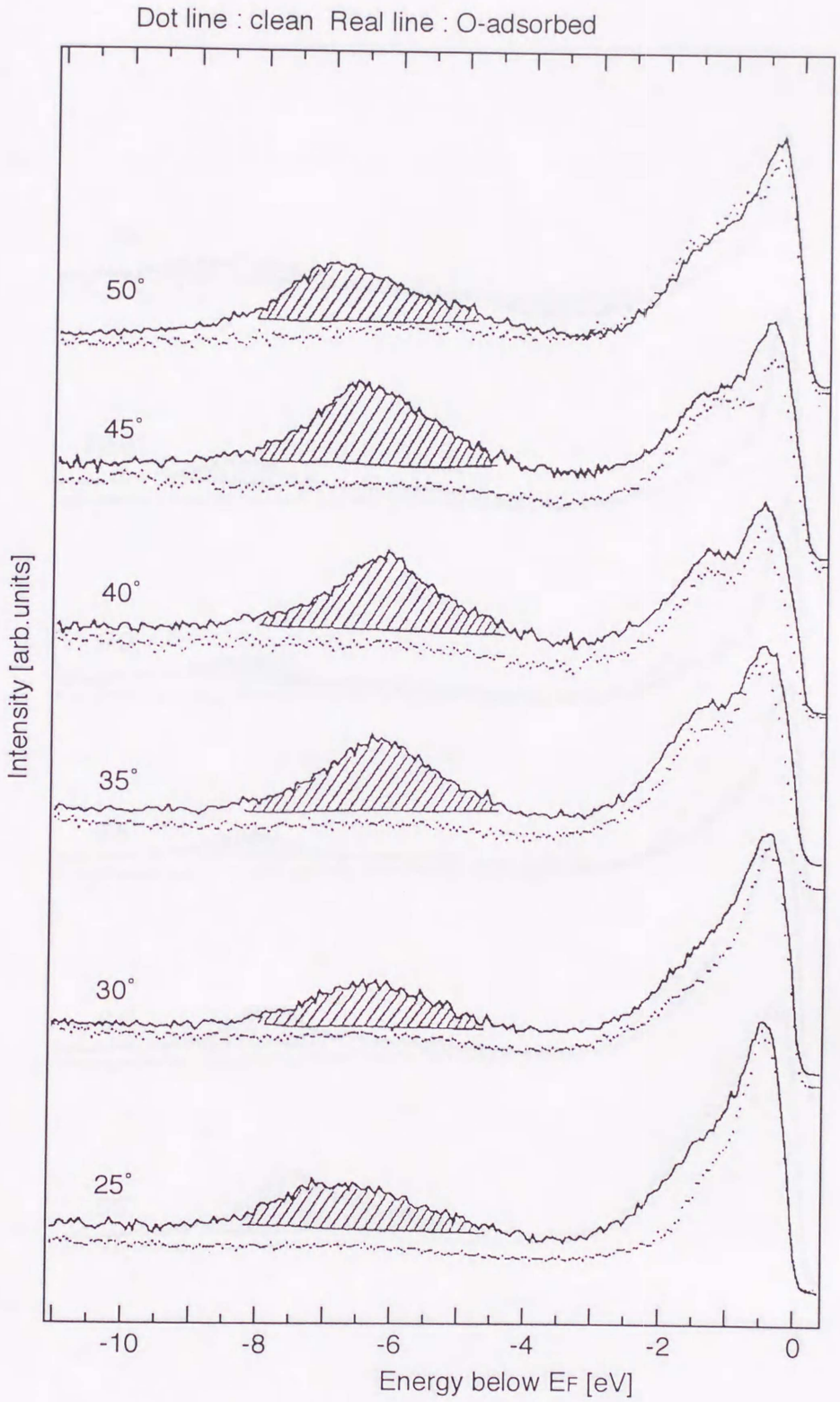

Figure 5-3(e). AREDCs measured using HeII radiation as a function of the emission angle θe (25°~50°) along the <001> direction ($\bar{\Gamma}$-$\bar{Y}$).

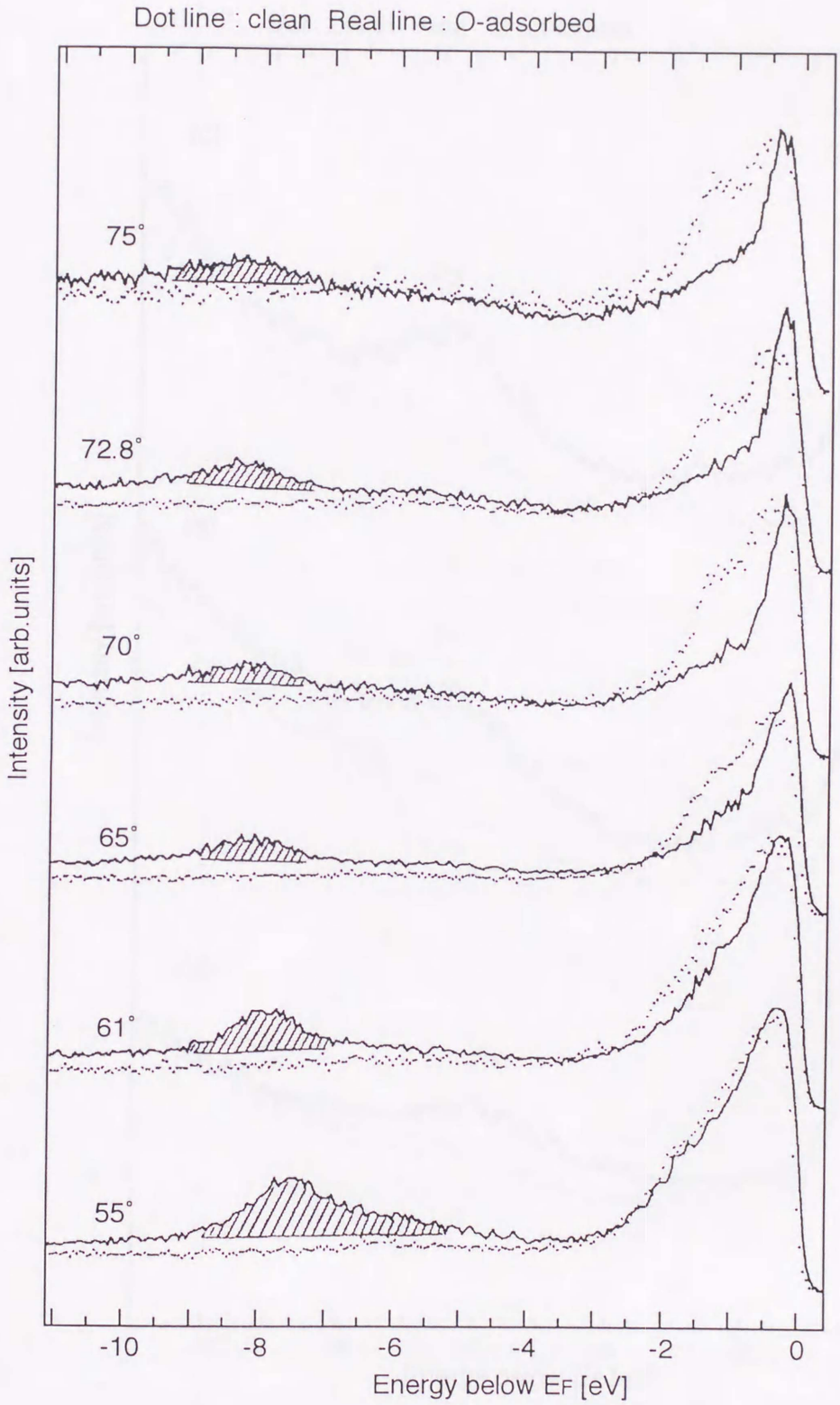

Figure 5-3(f). AREDCs measured using HeII radiation as a function of the emission angle θe (55°~75°) along the <001> direction ($\bar{\Gamma}$-$\bar{Y}$).

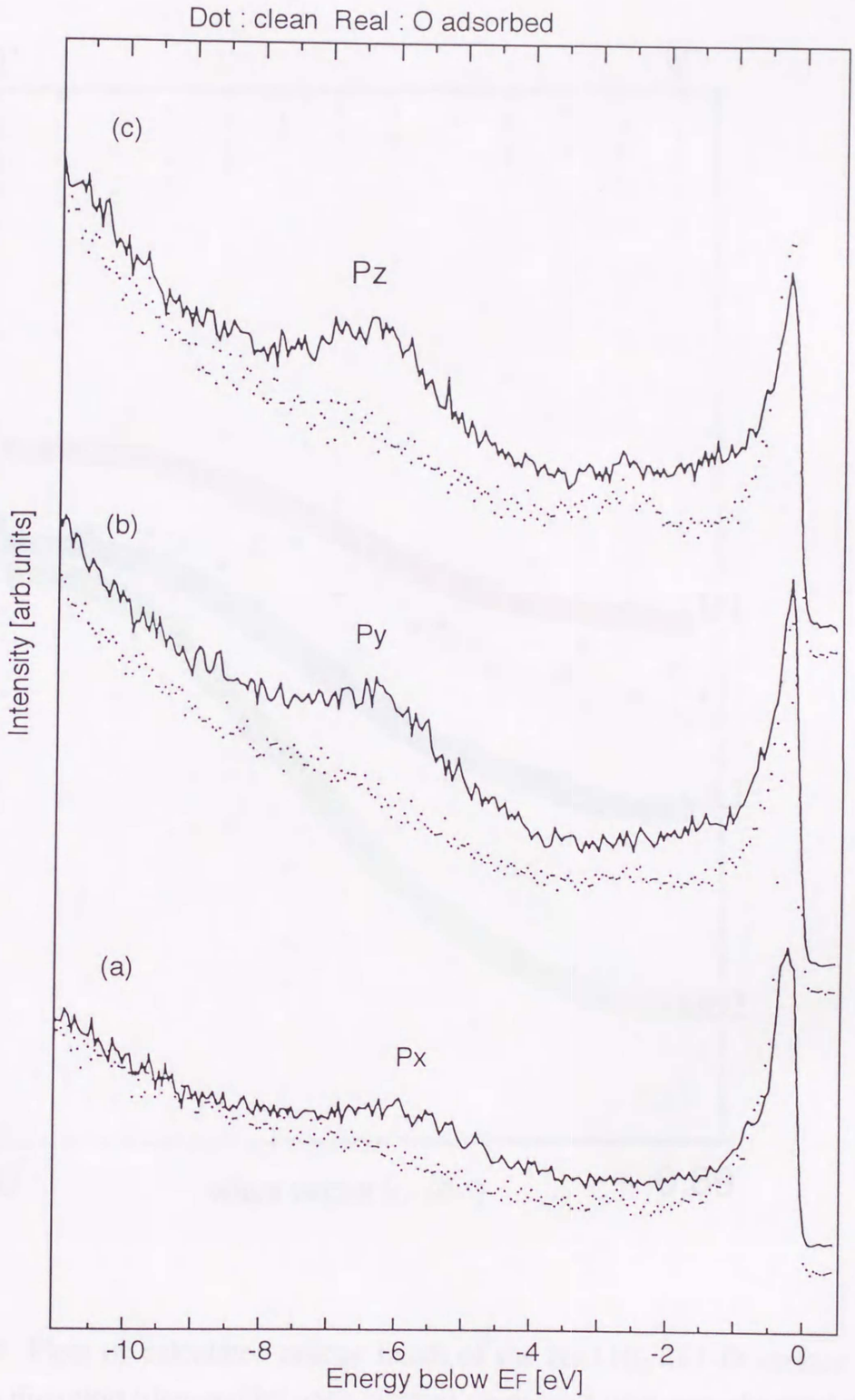

Figure 5-4. EDCs of Ni(110)/2x1-O surface measured using linearly polarized HeI radiation at $\bar{\Gamma}$; (a) $\hat{A}$ parallel to $<\bar{1}10>$ and θ_l=20°, p_x (b) $\hat{A}$ perpendicular to $<\bar{1}10>$ and θ_l=20°,p_y (c) $\hat{A}$ perpendicular to $<\bar{1}10>$ and θ_l=65°,p_z.

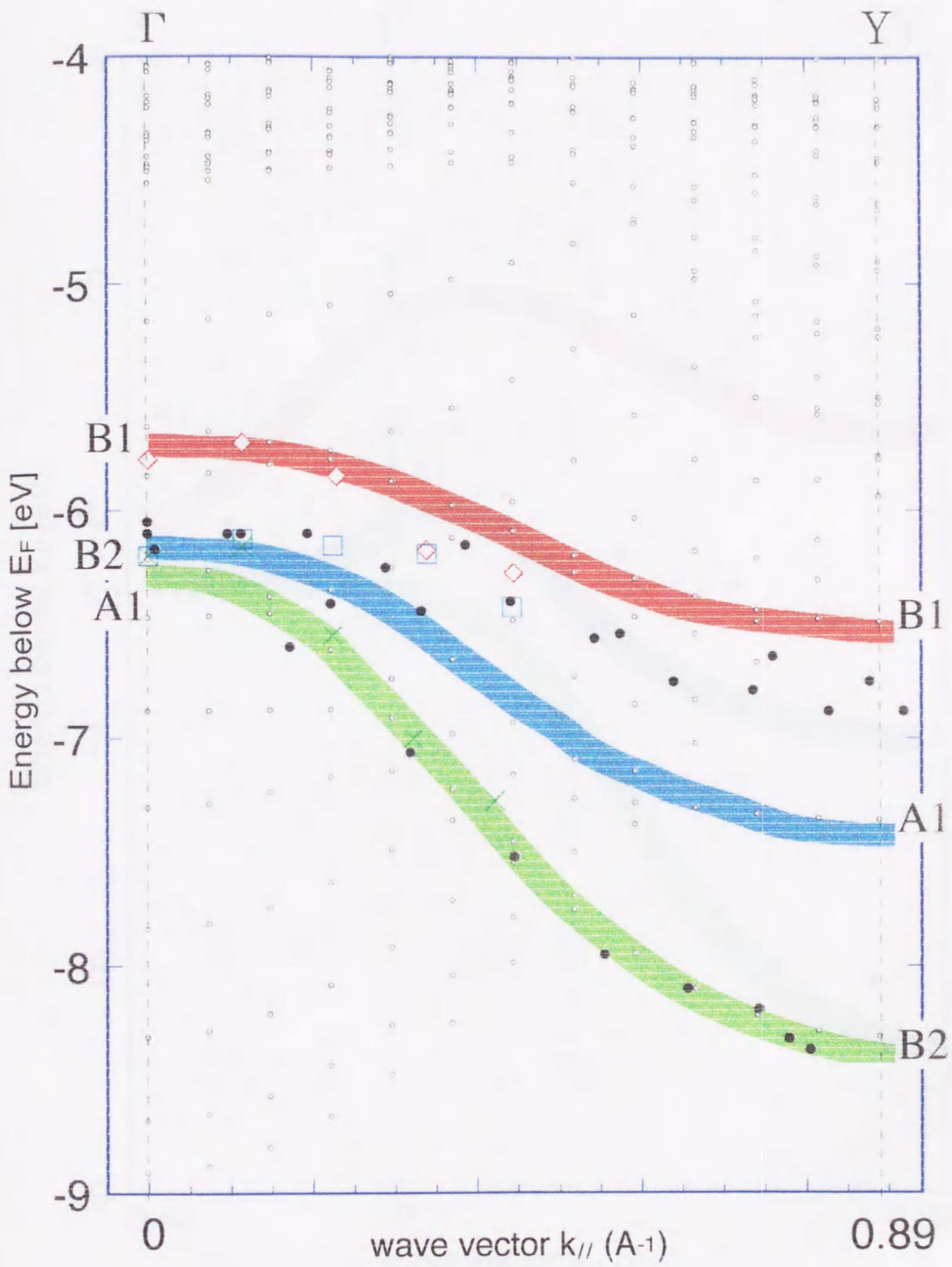

Figure 5-5. Plots of calculated energy bands of the Ni(110)/2x1-O surface along the <001> direction (denoted by open circles) compared with experimental points. Each calculated band, p_x-band(B1), p_y-band(B2) and p_z-band(A1), is shaded for the purpose of easy recognition of the correspondence between calculated bands and experimental points. Marks are same as in Fig.4-7.

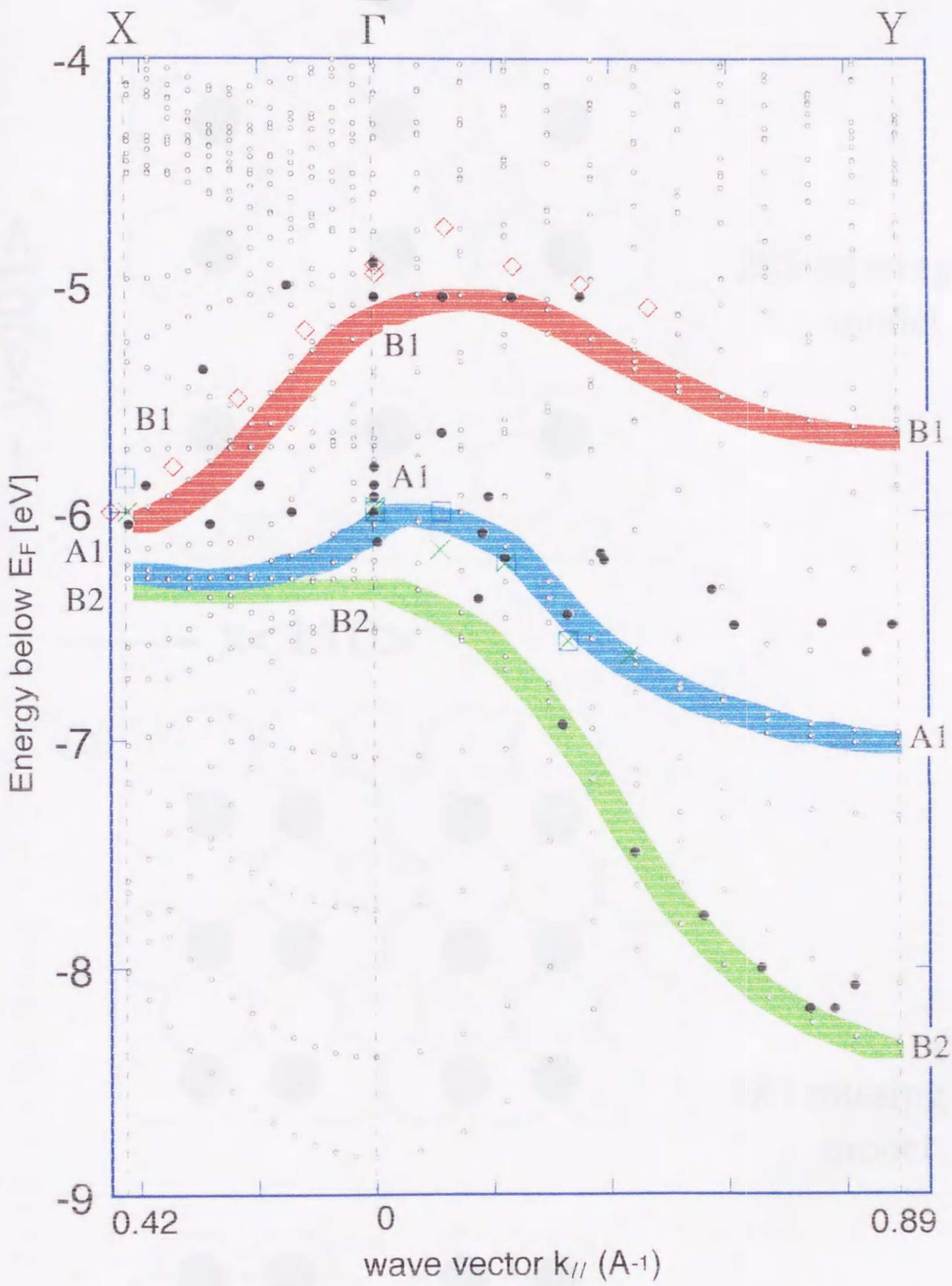

Figure 5-6. Plots of calculated energy bands of the Ni(110)/3x1-O surface along the <001> and <$\bar{1}$10> direction compared with experimental points. Marks are same as in Fig.4-7.

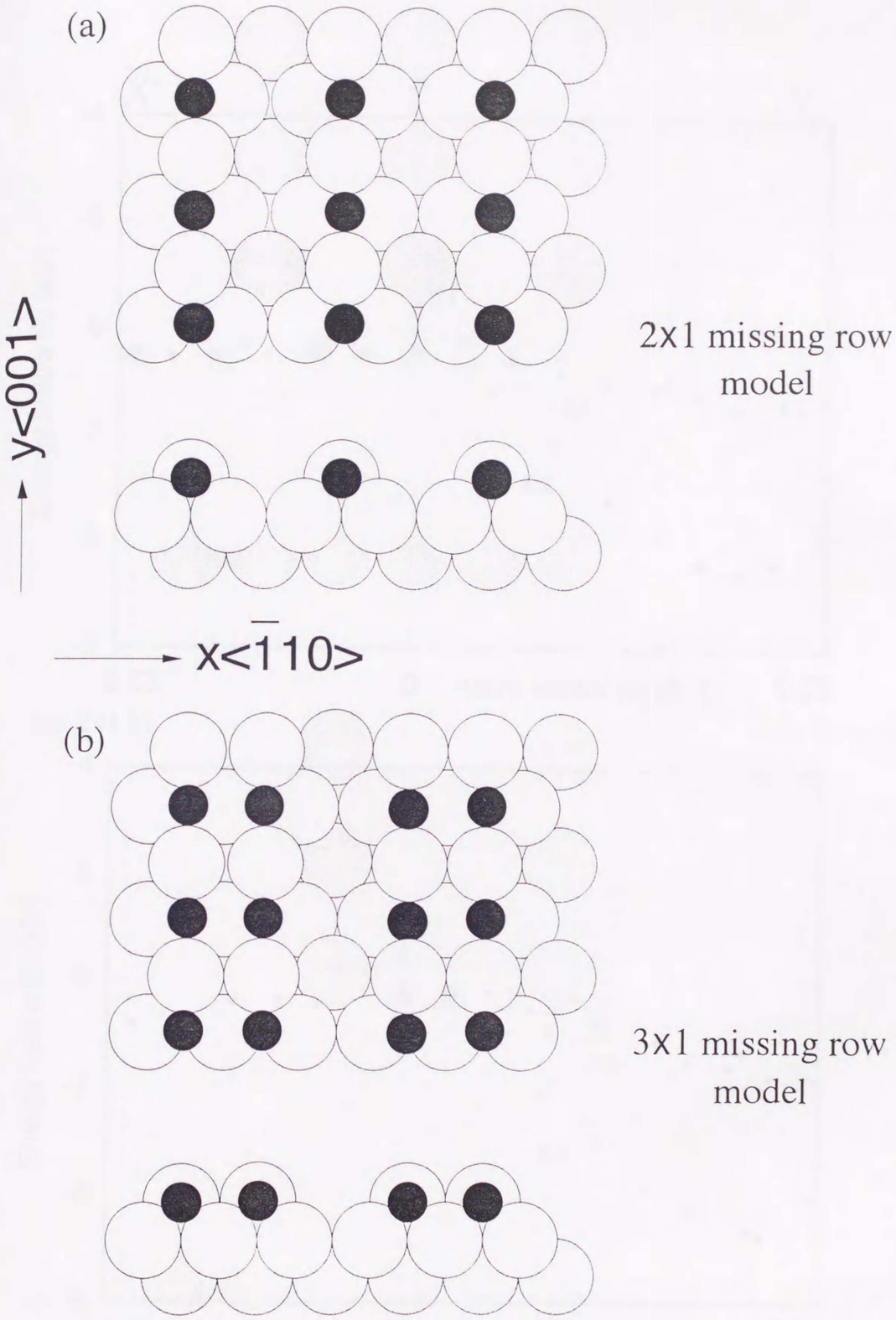

Figure 5-7. Missing row models of oxygen adsorbed Ni(110) surfaces. (a). 2x1-O model. (b). 3x1-O model.

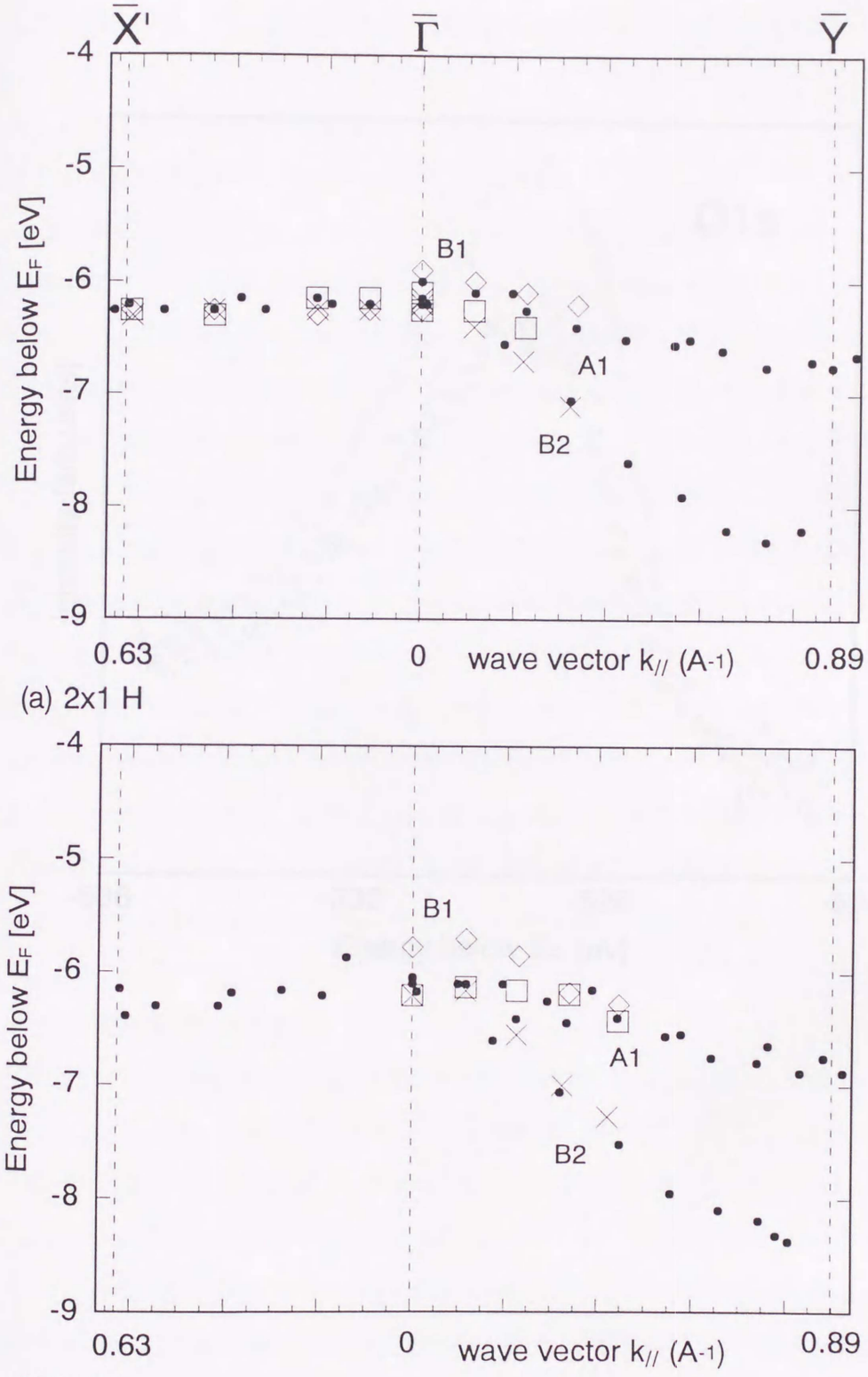

Figure 5-8. Energy bands of the oxygen induced features of (a) the high-exposed and (b) low-exposed Ni(110)/2X1-O surfaces.

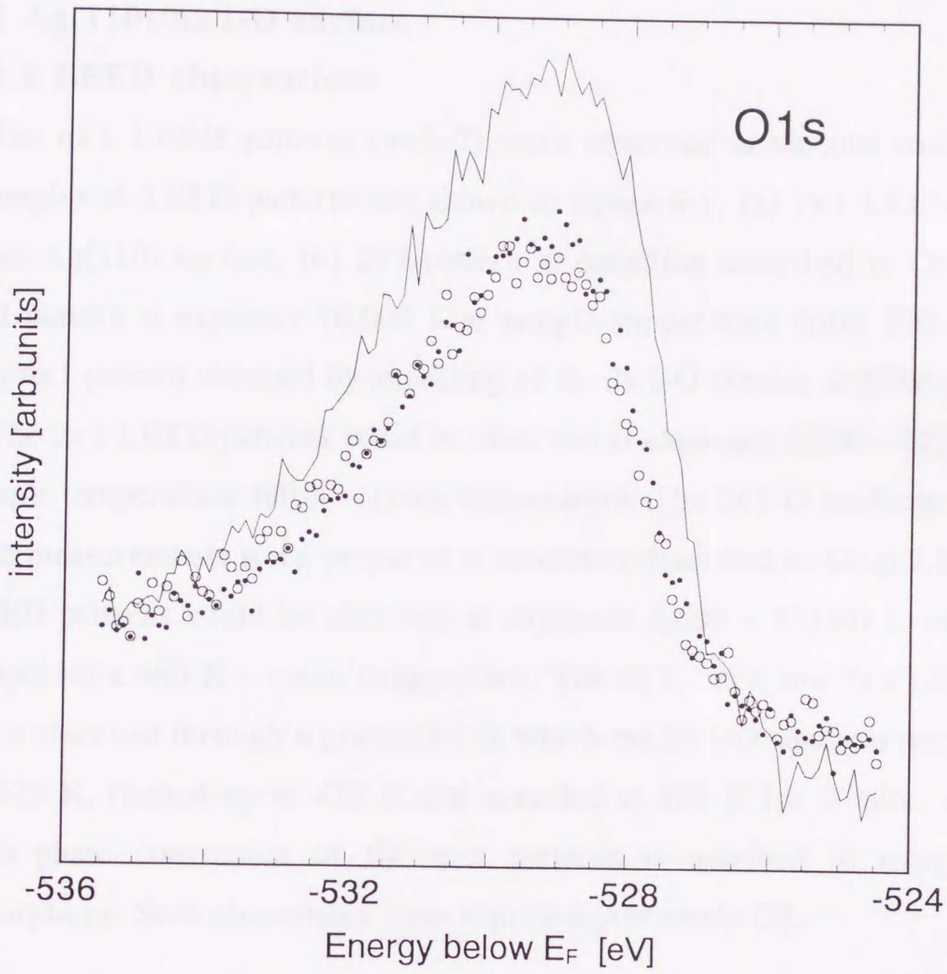

Figure 5-9. O*1s* XPS EDC of the high-exposed Ni(110)/2x1-O surface (●), compared with those of the low-exposed Ni(110)/2x1-O (○) and Ni(110)/3x1-O (real line) surfaces.

Chapter 6 Clean and oxygen adsorbed Ag(110) surface

6.1 Ag(110)/nx1-O surface

6.1.1 LEED observations

The nx1 LEED patterns (n=1~7) were observed at various conditions. The examples of LEED patterns are shown in figure 6-1; (a) 1x1 LEED pattern for clean Ag(110) surface, (b) 2x1 pattern at condition described in Chap.3.2.5, (c) 3x1 pattern at exposure 10,000 L at sample temperature from 370 K to 350 K, (d) 4x1 pattern obtained by annealing of the 3x1-O surface at 373K for 2 min.

The 2x1 LEED patterns could be observed at exposure 4,500 ~ 22,500 L and at sample temperature 480 K ~ room temperature. The 2x1-O surfaces for UPS and XPS measurements were prepared at condition described in Chap.3.2.5. The 3x1 LEED patterns could be observed at exposure 3,600 ~ 15,000 L and at sample temperature 480 K ~ room temperature. The 4x1, 6x1 and 7x1 LEED patterns were observed through a procedure in which the 2x1-O surfaces were flashed up to 425 K, flashed up to 472 K and annealed at 472 K for 2 min., respectively. This phase conversion of the spot patterns is ascribed to oxygen thermal desorptions. Such phenomena were reported previously [2].

6.1.2 Work functions

The WF changes of Ag(110)/2x1-O and 3x1-O surfaces were measured and shown in figure 6-2; $\Delta\Phi$ = 0.74 $\pm$0.09 eV for 2x1-O and 0.60 $\pm$0.07 eV for 3x1-O. The WF of clean surface was 4.45 eV. The points with error bars indicate the present results and the solid curve indicates WF changes which Engelhardt et al. [2] obtained. But values of exposure of their study are not in agreement with that of the present experiment because they obtained the nx1-O surfaces at room temperature. So their values are multiplied by a factor to correspond with each other.

The WF change is an increase as same as the Cu(110)/2x1-O surface, so it can

be considered that the adsorbates (oxygen atoms) behave as electron acceptors.

6.1.3 Oxygen coverage

It is generally assumed that the oxygen coverage of the Ag(110)/2x1-O is 0.5 ML [2,36-38]. In the present study, the oxygen coverage of the Ag(110)/2x1-O surface was quantitatively investigated from XPS measurements. The procedure follows a theoretical consideration by C.S.Fadley et al. [39].

Suppose there is an overlayer on a clean surface. Here assume the overlayer to be thin enough so that the substrate XPS signal does not suffer attenuation.

Peak intensity $N_S(\theta)$ from substrate is (the index $S_{(ubstrate)}$ means S-subshell),

$$N_S(\theta) = I_0 \cdot \Omega_0(E_{kin}) \cdot A_0(E_{kin}) \cdot D_0(E_{kin}) \cdot \rho \cdot (d\sigma_S / d\Omega) \cdot \Lambda_e(E_S) \quad ,$$

where I_0 is an incident flux, $\Omega_0(E_{kin})$ is an effective solid angle of E_{kin} which is a kinetic energy of photoelectron, $A_0(E_{kin})$ is an effective specimen area, $D_0(E_{kin})$ is a detection efficiency, ρ is a mean density of substrate atoms in which peak S originates in cm^{-3}, $d\sigma_S / d\Omega$ is an S-subshell differential cross-section, θ is the emission angle shown in figure 6-3 and $\Lambda_e(E_S)$ is an attenuation length in the substrate. E_S is an energy with respect to the bottom of valence band, in another expression $E_S = E_{kin} + V_0$, where V_0 is an inner potential as shown in figure 6-4.

Peak intensity $N_A(\theta)$ from overlayer is (the index $A_{(dsorbate)}$ means A-subshell),

$$N_A(\theta) = I_0 \cdot \Omega_0(E_{kin'}) \cdot A_0(E_{kin'}) \cdot D_0(E_{kin'}) \cdot s' \cdot (d\sigma_A / d\Omega) \cdot (\cos\theta)^{-1} \quad ,$$

where $d\sigma_A / d\Omega$ is an A-subshell differential cross-section, s' is a mean surface density of atoms in which peak A originates in cm^{-2} and $E_A = E_{kin'} + V_0$.

Then overlayer/substrate ratio is,

$$\frac{N_A(\theta)}{N_S(\theta)} = \frac{I_0 \cdot \Omega_0(E_{kin'}) \cdot A_0(E_{kin'}) \cdot D_0(E_{kin'}) \cdot s' \cdot (d\sigma_A / d\Omega)}{I_0 \cdot \Omega_0(E_{kin}) \cdot A_0(E_{kin}) \cdot D_0(E_{kin}) \cdot (d\sigma_S / d\Omega) \cdot \Lambda_e(E_S) \cdot \cos\theta \cdot s / d}$$

$$= \frac{s'}{s} \cdot \frac{\Omega_0(E_{kin'}) \cdot A_0(E_{kin'}) \cdot D_0(E_{kin'}) \cdot (d\sigma_A / d\Omega) \cdot d}{\Omega_0(E_{kin}) \cdot A_0(E_{kin}) \cdot D_0(E_{kin}) \cdot (d\sigma_S / d\Omega) \cdot \Lambda_e(E_S) \cdot \cos\theta} \quad ,$$

where s is a mean surface density of atoms in which peak S originates in cm^{-2} and

d is a mean separation between layers of density s in the substrate ($d = s/\rho$). And s'/s is a monolayer (adsorbates) coverage of the atomic species in which peak A originates. Here it is reasonably approximated that $\Omega_0(E_{kin'}) = \Omega_0(E_{kin})$, $A_0(E_{kin'}) = A_0(E_{kin})$ and $D_0(E_{kin'}) = D_0(E_{kin})$. It is also reasonable that $d\sigma_S/d\Omega$ and $d\sigma_A/d\Omega$ are replaced with σ_S and σ_A, respectively.

Then an adsorbate coverage can be described:

$$\frac{s'}{s} = \frac{N_A(\theta)}{N_S(\theta)} \cdot \frac{\sigma_S \cdot \Lambda_e(E_S) \cdot \cos\theta}{\sigma_A \cdot d} \quad . \tag{6-1}$$

These expressions are useful at very low exposures to adsorbates ($s'/s \leq 1$) for estimation of the fractional monolayer coverage from observed peak intensities.

In this experiment $AlK\alpha$ (1486.6 eV) characteristic line was used and the Ag$3d$ and O$1s$ peaks were selected as reference peaks due to their high cross-sections.

The other constants:

d = 1.445 Å

$\sigma_{(Ag3d)}$ = 0.2474 Mb [40]

$\sigma_{(O1s)}$ = 0.04 Mb [40]

$\Lambda_e(E_S)$ = 13.1 Å ; is given by an empirical formula $\cong 15.0\sqrt{E_S/1482}$.

Figure 6-5 shows the example of the XPS EDC of Ag(110)/2x1-O surface at incident angle 0° and emission angle 75°. The areas of peaks subtracted the background correspond to $N(75°)$ in equation (6-1). Then Oxygen coverage of Ag(2x1)-O surface $\theta_{(2x1)}$ could be estimated. The overestimation resulting from the photoelectrons from the oxygen atoms adsorbed on the sample holder, was deducted. The measurements were performed at two measurement arrangements; incident angle 0° and emission angle 75°, incident angle 25° and emission angle 50° for the purpose of averaging the anisotropies [41] due to diffraction effect, and totally made four times.

The average $\theta_{(2x1)}$ was estimated:

$\theta_{(2x1)}$ = 0.47 ML ,(1 ML = 8.46×10^{14} per cm^2) .

The degrees of the experimental anisotropies of Ag$3d$ peak intensities depending

on azimuth ϕ at emission angle 77° and 62° has been reported [41]:

$(I_{max} - I_{min}) / I_{max} = 0.40$, 0.51 , respectively.

where I_{max} and I_{min} are the maximum and minimum intensities as a function of azimuth. The present results should contain this uncertainty. However, this estimation is consistent with the established reports [2,36-38], so this estimation including such approximations can be reliable.

6.1.4 Angle-resolved photoemission study of clean and Ag(110)/2x1-O surface

The surface prepared by the cleaning procedure was checked as described in Chap.3.2.4. In addition, the *s-p* surface state [42] observed only for the clean Ag(110) surface was confirmed. Figure 6-8 shows the EDC of clean Ag(110) surface at θe = 20° (around $\overline{Y}$) with that of Ag(110)/1x2-O surface for reference. The *s-p* surface feature could be observed in the EDC of clean surface and it was not observed in the EDC of Ag(110)/1x2-O surface. This is in good agreement with the report [42], so this suggests the surface prepared in the present experiment to be well cleaned. Observation of the *s-p* surface state is, therefore, one of the evidences for the Ag(110) surface cleanliness.

Sequences of AREDCs were measured at various emission angles for the clean and Ag(110)/2x1-O surfaces along the <001> direction ($\overline{\Gamma}$-$\overline{Y}$) and along the <$\bar{1}$10> direction ($\overline{\Gamma}$-$\overline{X}$). Figure 6-6 shows examples of AREDCs measured using HeI radiation as a function of the emission angle θe along the <$\bar{1}$10> direction ($\overline{\Gamma}$-$\overline{X}$). Figure 6-7 shows the similar AREDCs along the <001> direction ($\overline{\Gamma}$-$\overline{Y}$). Solid curves indicate the AREDCs corresponding to of the Ag(110)/2x1-O surfaces, and dotted curves indicate that of the clean Ag(110) surface in those figures. The shaded areas in those figures indicate the new features appeared in the Ag(110)/2x1-O spectra. These features around -3 eV are assigned to oxygen-induced anti-bonding states. A schematic energy diagram of Ag*4d*-O*2p* bonding is shown in figure 6-9. The on-site energy of O*2p* (E_{Op}) is estimated at

energy -3.0 ~ -4.0 eV from calculations of Cu(110)/2x1-O and Ni(110)/2x1-O surfaces. Then the E_{Op} is located about 1.5 eV above the Ag*4d* bands (~-5 eV). This means that the oxygen-induced anti-bonding states should be located above -3.0 ~ -4.0 eV and the oxygen-induced bonding states should be located below Ag*4d* bands. This means that the oxygen-induced anti-bonding states have the oxygen character. This is consistent with the previous report [26] concerning the feature found around -3 eV.

Figure 6-10 shows the example of the EDCs of clean and Ag(110)/2x1-O surface at $\overline{Y}$ point ($\theta e = 22^\circ$) and figure 6-11 shows the AREDCs of Ag(110)/2x1-O surfaces, using HeI radiation polarized parallel or perpendicular to $<\bar{1}10>$ direction. As indicated in those figures, the states with p_y and p_z symmetry can be assigned from the polarization selection rules. The states with p_x symmetry were not assigned except at $\overline{\Gamma}$ point. The spectra were measured at three arrangements; (a) $\hat{A}$ parallel to $<\bar{1}10>$ and $\theta_I=20^\circ$ (b) $\hat{A}$ perpendicular to $<\bar{1}10>$ and $\theta_I=20^\circ$ (c) $\hat{A}$ perpendicular to $<\bar{1}10>$ and $\theta_I=70^\circ$ as shown in Fig.2.5. Then the p_x symmetry features were selectively appeared at arrangement (a), in the same way, mainly p_y at (b) and p_z at (c).

Figure 6-12 shows energy (k-E) dispersion along the <001> and $<\bar{1}10>$ direction. Measurements were performed using unpolarized and linearly polarized light. Symbolic marks for Ag(110)/2x1-O surface denote: (•) hν=21.22 eV and hν=40.8 eV, unpolarized; (◇) hν=21.22 eV, p_x feature; (×) hν=21.22 eV, p_y feature; (□) hν=21.22 eV, p_z feature; and for clean surface: small (□) hν=21.22 eV, unpolarized. In the figure, the Ag4*d*-bands are observed at -3.8 ~ -7.3 eV. Along the <001> direction ($\overline{\Gamma}$-$\overline{Y}$), the bands at -1.5 ~ -3.0 eV have a periodicity of the surface reciprocal lattice and they are assigned to p_y and p_z bands. Along the $<\bar{1}10>$ direction ($\overline{\Gamma}$-$\overline{X}$), the bands at -3.0 eV is assigned to p_x band and there is not practically any dispersion (± 0.1 eV). Although features were observed at around -2.4 eV, their characters could not be assigned.

6.1.5 Simplified-LCAO calculation of Ag(110)/2x1-O surface

The simplified-LCAO calculation of Ag(110)/2x1-O surface was performed to compare with the features described in chapter 6.1.4. Before calculating the Ag(110)/2x1-O surface, a calculation of clean surface was made where the LCAO parameters of Ag-Ag interactions were adopted from the literature [34]. The error in the Ag*4d* bands width *W* between the calculation and the experiment at $\overline{\Gamma}$ was within ±0.3 % (±0.01 eV), corresponding to 1/10 the energy resolution of this system. The Fermi level of the calculation was decided so that both the *d*-band levels were in agreement.

Figure 6-13 shows the calculation of Ag(110)/2x1-O surface with the experimental results. The LCAO parameters for the Ag-Ag interactions were also adopted from the literature [34]. The Ag-O interactions, sPσ , pPσ , pPπ , Pdσ , Pdπ , surface shift and the on-site energy of O orbitals E_{Op} given in table 2-2, were treated as adjustable parameters to fit the experimental results. The symbolic marks are same as in Fig.4-5. The open circles denote the calculated energy bands and each calculated band, which has dominantly p_x, p_y and p_z character, is shaded for the purpose of easy recognition of the correspondence between calculation and experiment. They belong to B1, B2 and A1 irreducible representation, respectively. Along the <001> direction ($\overline{\Gamma}$-$\overline{Y}$), the A1 band with p_z symmetry disperses from at -2.7 eV at $\overline{\Gamma}$ to at -1.4 eV at $\overline{Y}$. The B2 band with p_y symmetry disperses from at -3.0 eV at $\overline{\Gamma}$ to at -1.4 eV at $\overline{Y}$. The present calculation reproduces such features. The O2p_x, p_y and p_z orbitals are mainly bound with Ag4d_{zx} and 4$d_{3z^2-r^2}$, Ag5p_y and 4d_{yz}, and Ag4d_{zx} and 4$d_{x^2-y^2}$, respectively. These wavefunctions of Ag atoms are directed parallel to the p_x, p_y and p_z, respectively. The parameters are listed in table 6-1.

When comparing the parameters of Cu, Ni and Ag, for example the σ-bonding of O2*p*-Metal*4 or 5p* orbital; pPσ is 3.25 eV for Ni, 1.98 eV for Cu, 1.40 eV for Ag, thus they have a relation that,

$pP\sigma(Ni) > pP\sigma(Cu) > pP\sigma(Ag)$. (6-2)

The other sets of parameters with some exceptions have the same tendency as for their absolute values. In contrast to this, the lattice constants of them are,

$a(Ni) < a(Cu) < a(Ag)$.

Then the nearest neighbor interatomic lengths between the oxygen and substrate atoms have the same tendency. Each absolute value of the parameter set, i.e., each intensity of interaction becomes smaller with their interatomic lengths. The interaction is related to the overlap of the orbitals located on the oxygen and substrate atoms in general. This means that the degree of overlap, i.e., the absolute value of parameter becomes small when the interatomic length increases. So the tendency like equation (6-2) is reasonable.

Table 6-1 : LCAO parameters of Ag(110)/2x1-O surface

	(nn)	(nnn)	[eV]
[Ag-O two-center integrals]			
sPσ	1.00	0.333	
pPσ	1.40	0.466	
pPπ	-2.00	-0.666	
Pdσ	-1.40	-0.204	
Pdπ	1.00	0.146	
[Ag-Ag two-center integrals]			
ssσ	-0.8954	0.0195	
spσ	1.3308	0.0742	
ppσ	2.1432	0.5403	
ppπ	0.0883	0.0590	
sdσ	-0.4231	-0.0629	
pdσ	-0.5313	-0.0088	
pdπ	0.2067	0.0234	
ddσ	-0.4287	-0.0384	
ddπ	0.2391	0.0233	
ddδ	-0.0457	-0.0052	
[On-site energies from E_F and Surface Shift (ss)]			
E_{Op} =	-2.88		
Surface shift (ss) = 0			
Es =	2.8124		
Ep =	8.9533		
Ed1 =	-4.8134		
Ed2 =	-4.8465		

(nn) and (nnn) denote a nearest-neighbor and a next-nearest-neighbor Slater-Koster two-center integrals, respectively. The letter s,p,d,P denote the Ag 5s,5p,4d and O2p orbitals, respectively. Notations of the on-site energies are the same as in table 2-2.

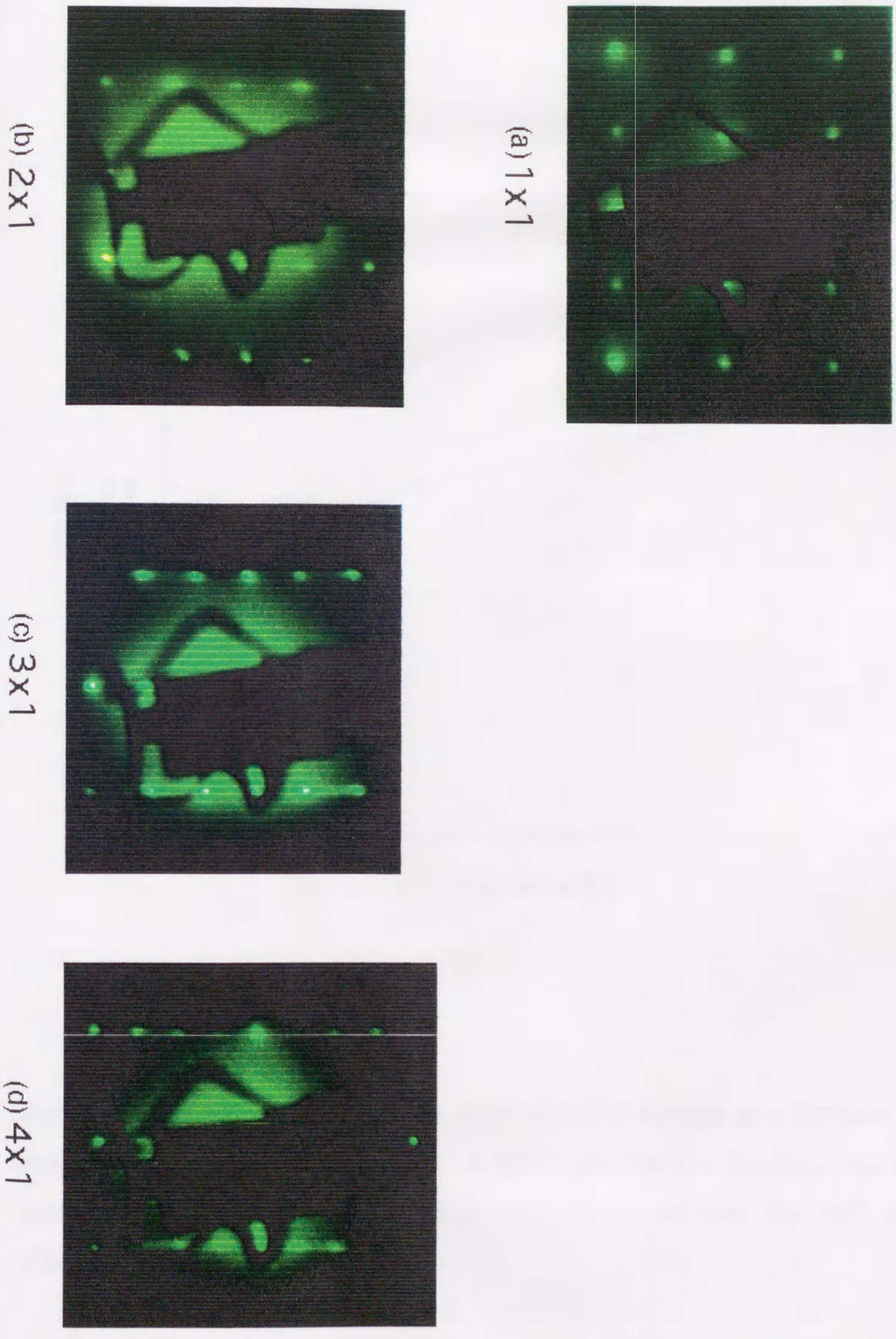

Figure 6-1. LEED patterns for the oxygen adsorbed Ag(110) surfaces: (a)1x2, (b)2x1, (c)3x1, (d)4x1.

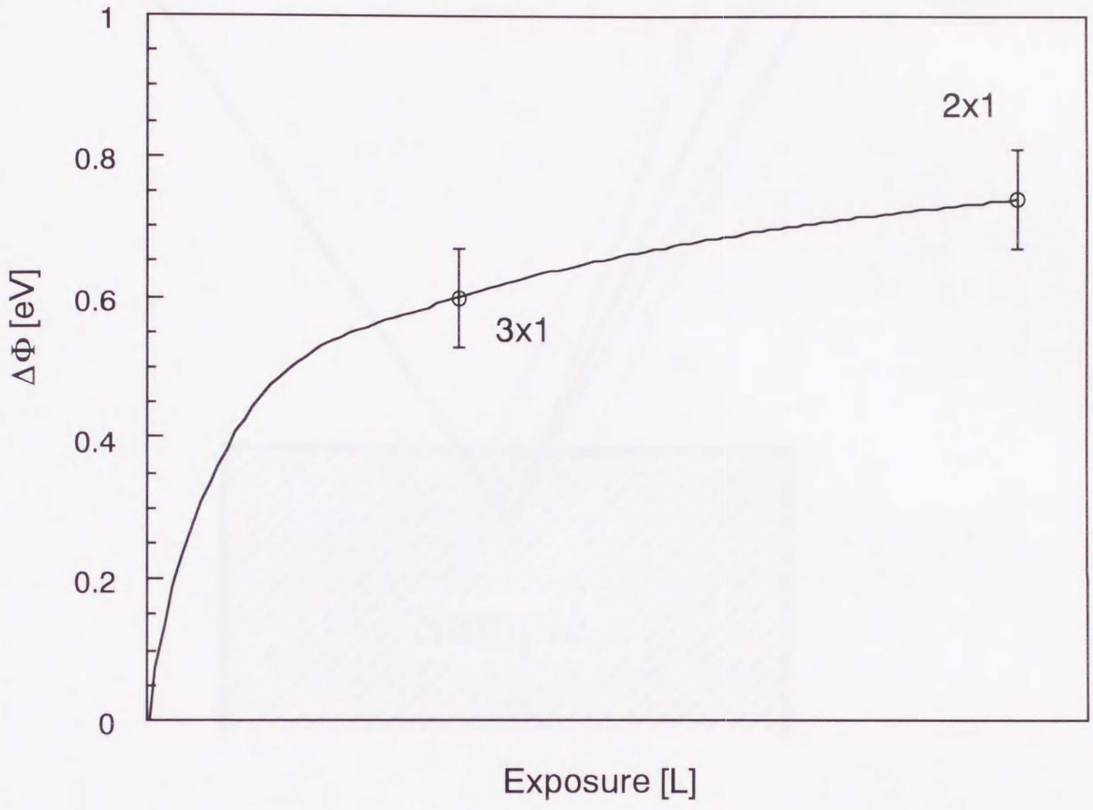

Figure 6-2. LEED patterns and the work function changes as a function of the oxygen exposure. The WF change is a difference between the clean and oxygen adsorbed Ag(110) surface WFs. The solid curve indicates the WF changes obtained by Engelhardt et al. [2]

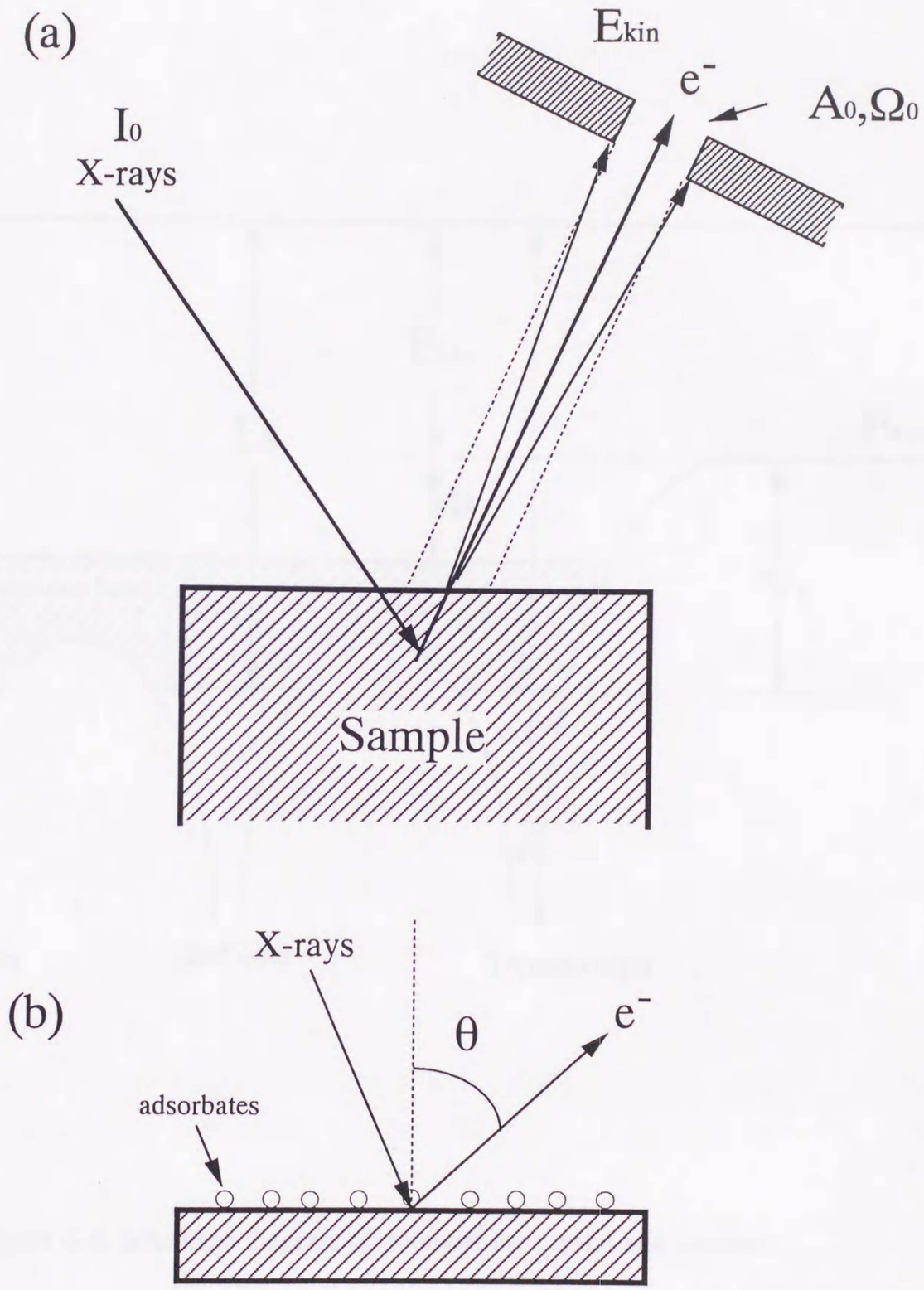

Figure 6-3. Idealized spectrometer geometry for calculating photoelectron peak intensities from solid specimen.

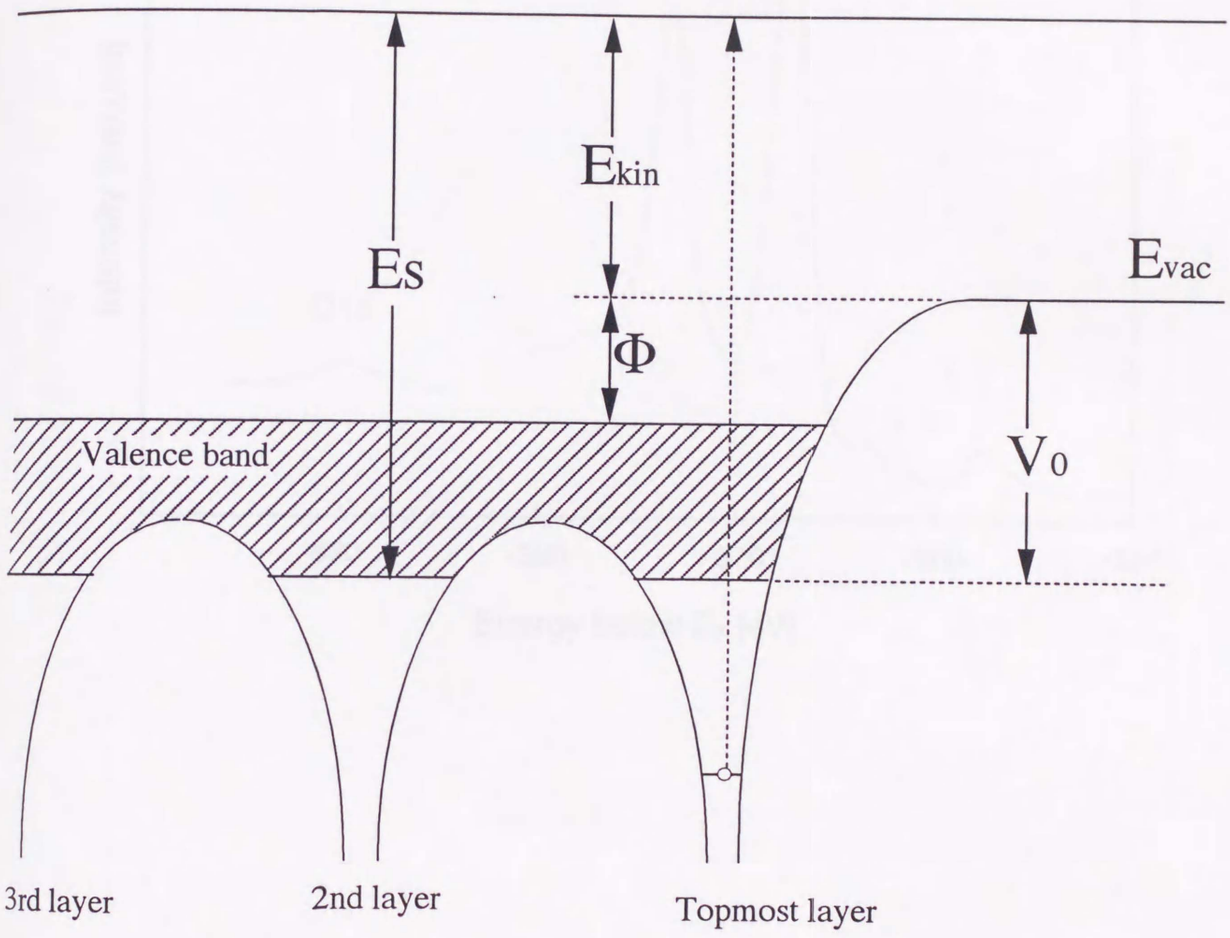

Figure 6-4. Schematic diagram of potential for crystal and vacuum.

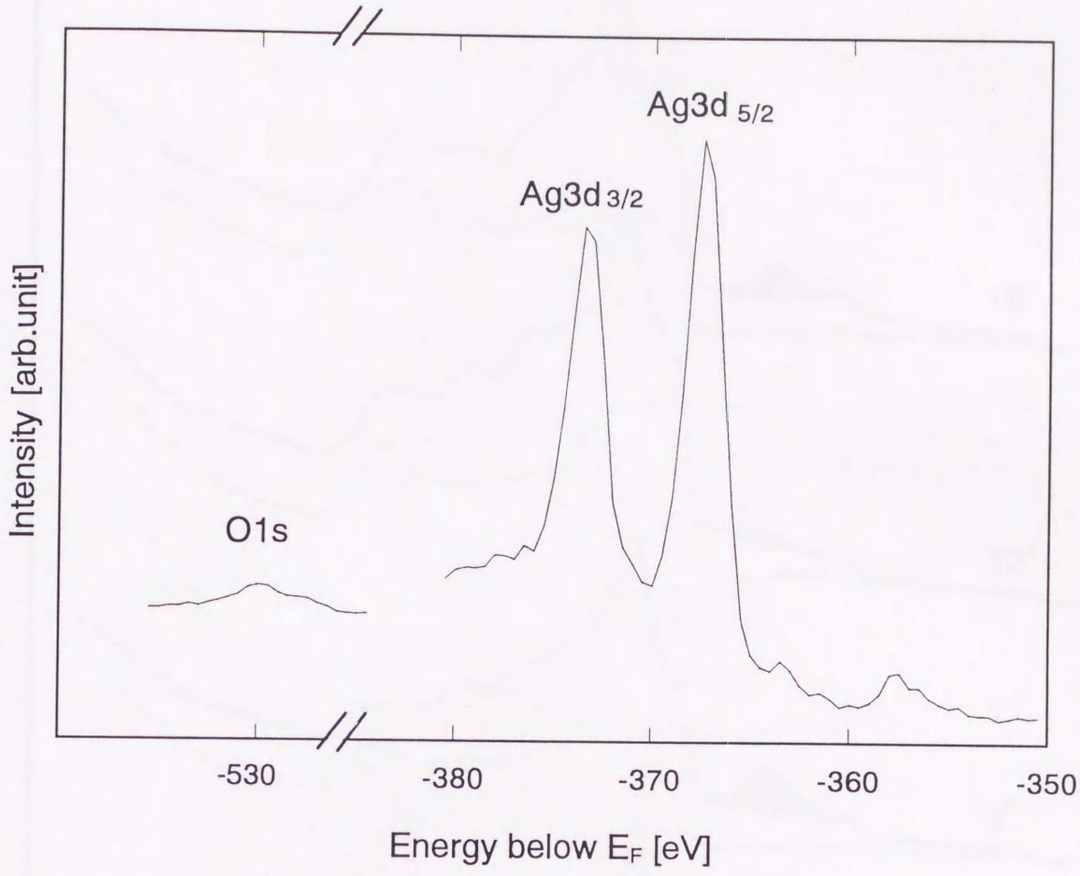

Figure 6-5. XPS EDC of Ag(110)/2x1-O surface; incident angle 0°, emission angle 75°.

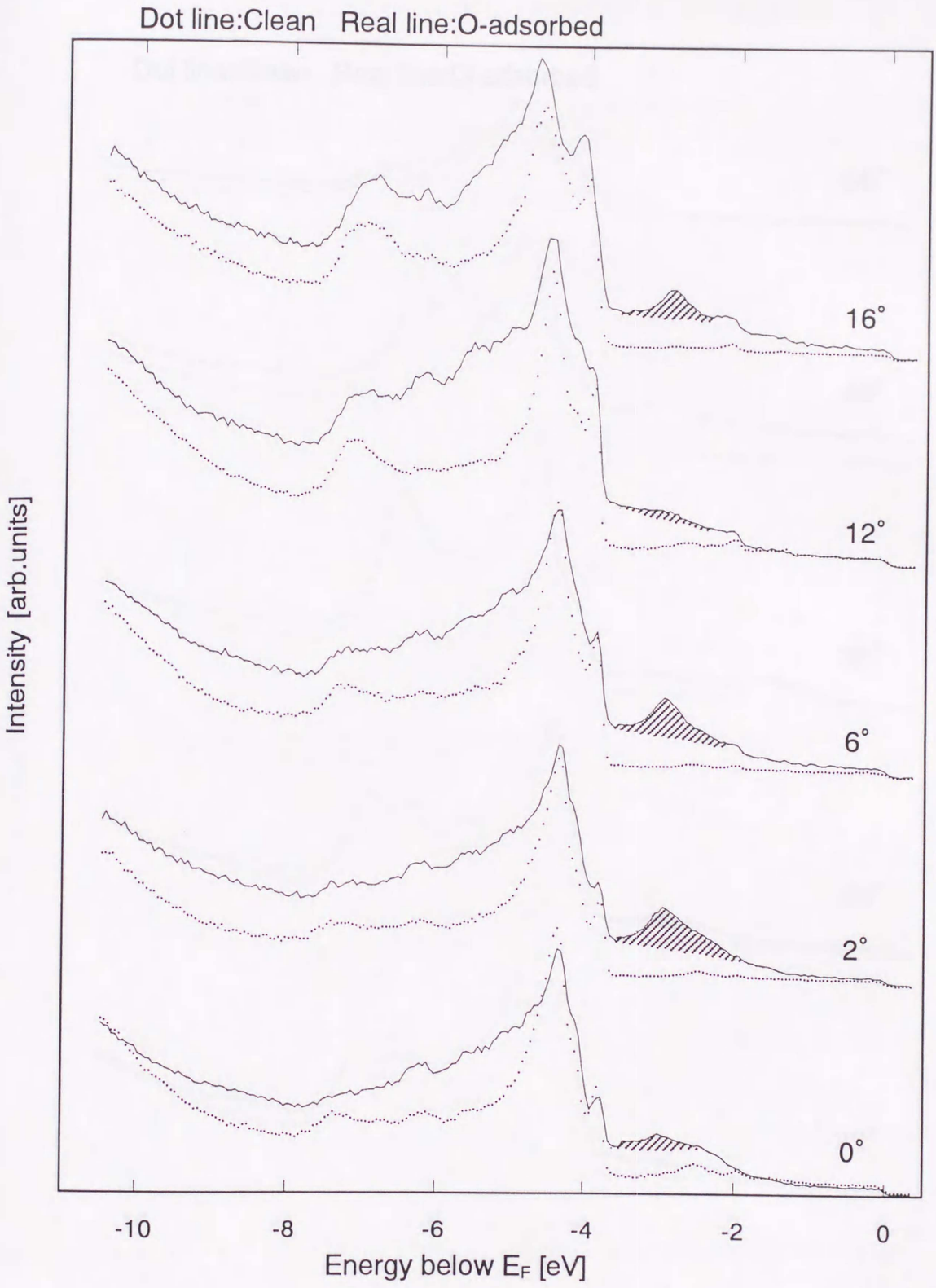

Figure 6-6(a). AREDCs measured using HeI radiation as a function of the emission angle θe (0°~16°) along the <$\bar{1}$10> direction ($\bar{\Gamma}$-$\bar{X}$). The shaded areas indicate the O-induced states.

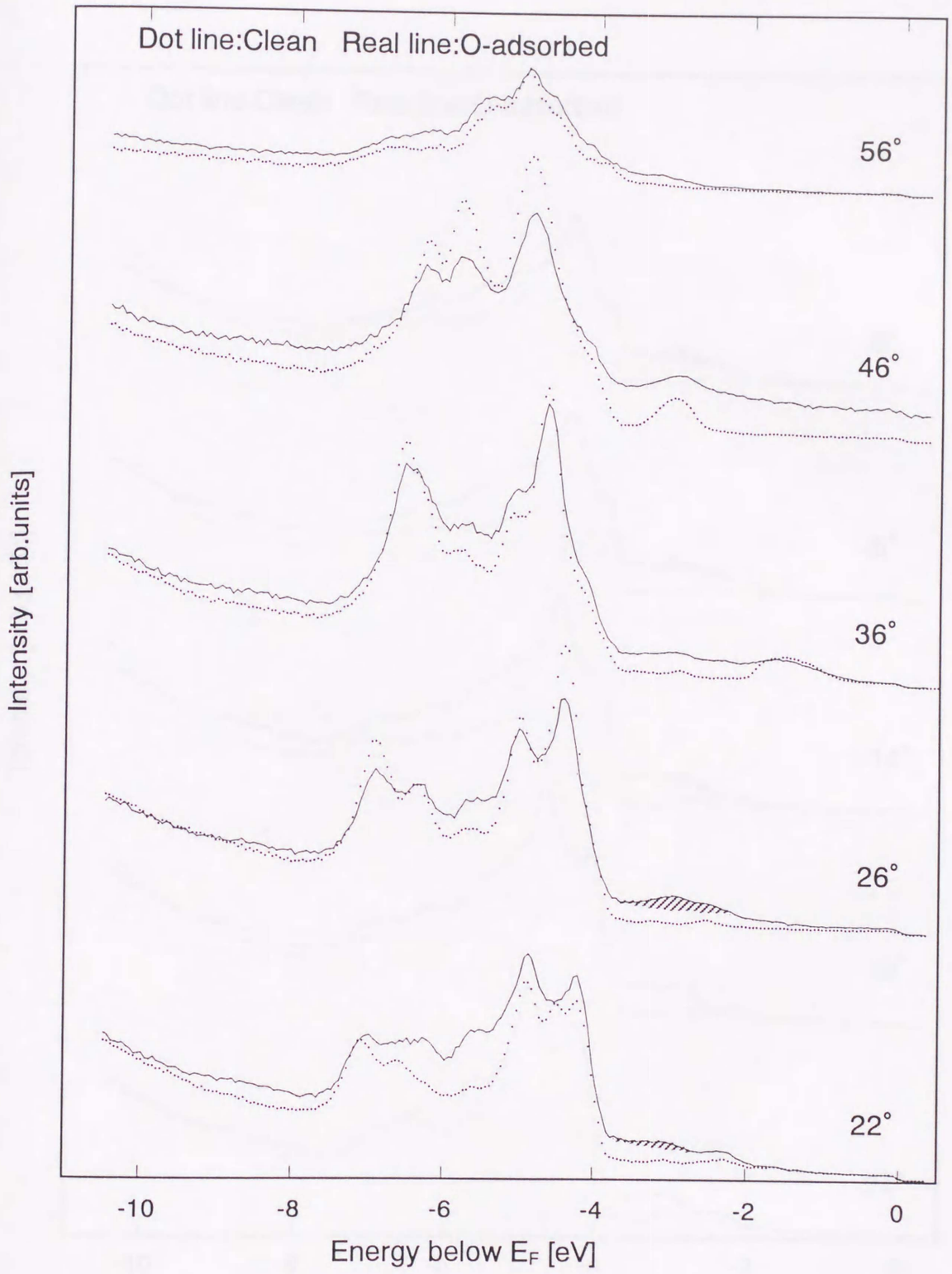

Figure 6-6(b). AREDCs measured using HeI radiation as a function of the emission angle θe (22°~56°) along the <$\bar{1}$10> direction ($\bar{\Gamma}$-$\bar{X}$).

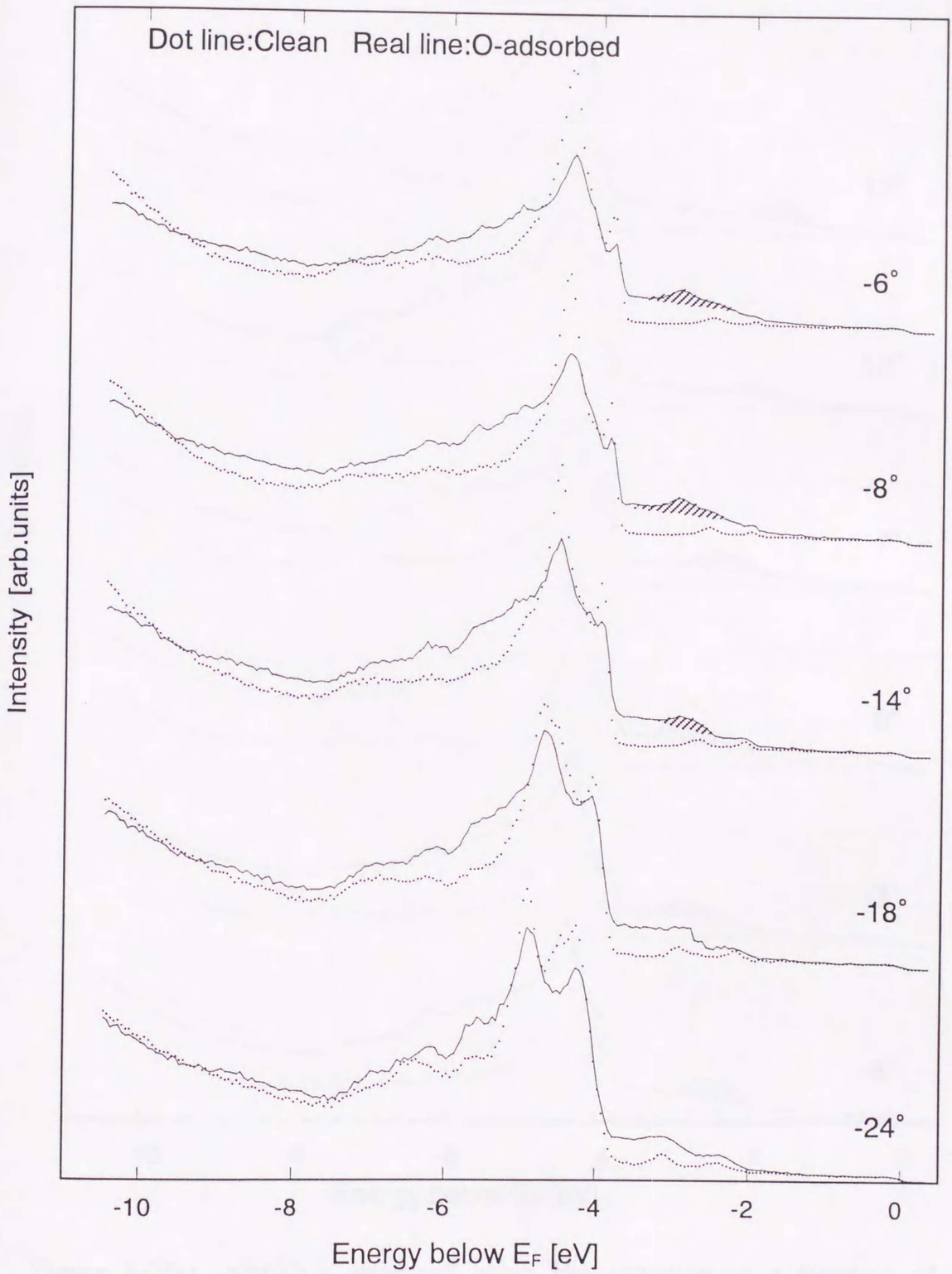

Figure 6-6(c). AREDCs measured using HeII radiation as a function of the emission angle θe (-6°~-24°) along the <$\bar{1}$10> direction ($\bar{\Gamma}$-$\bar{X}$).

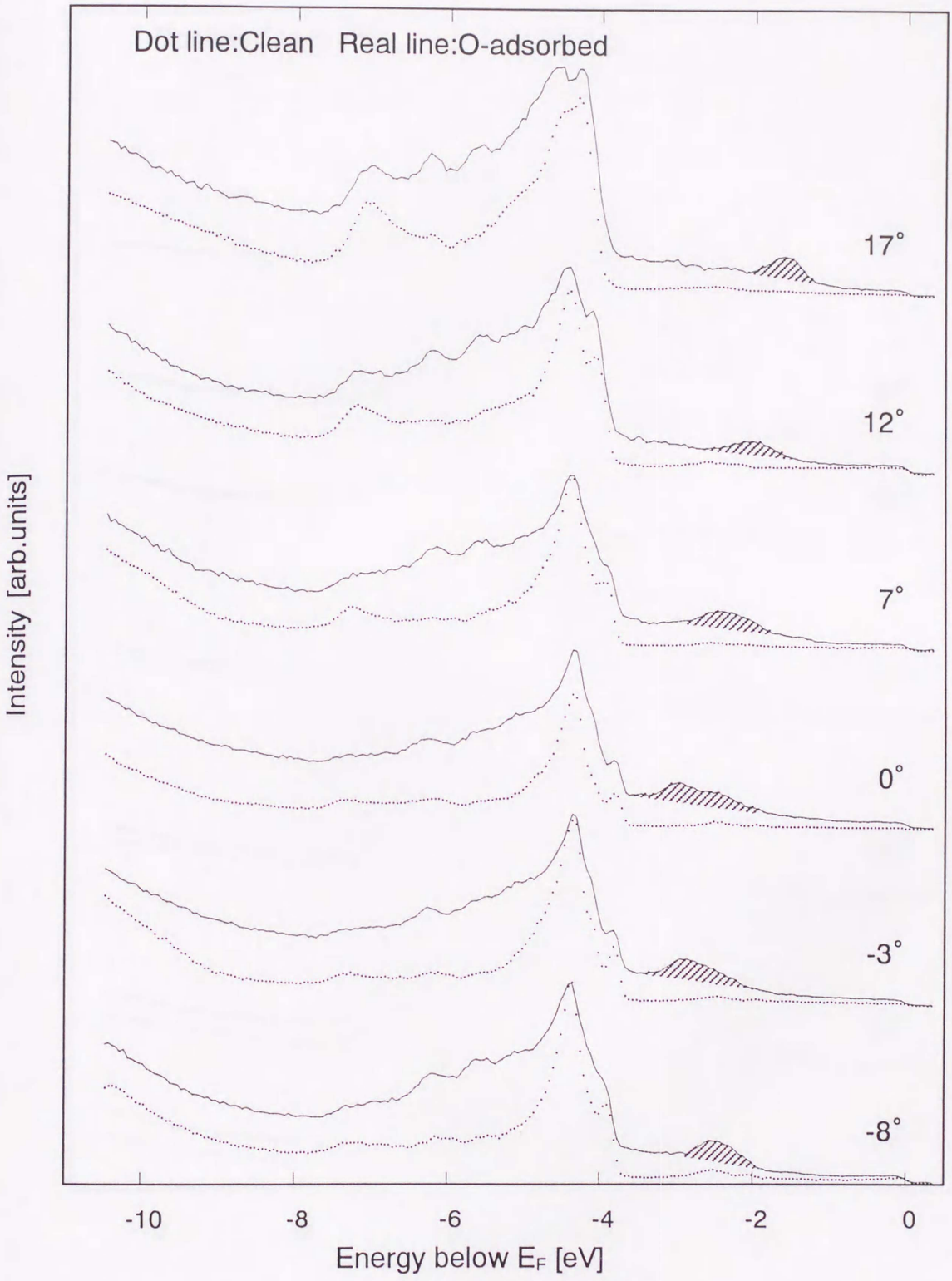

Figure 6-7(a). AREDCs measured using HeI radiation as a function of the emission angle θe (-8°~17°) along the <001> direction ($\overline{\Gamma}$-$\overline{Y}$). The shaded areas indicate the O-induced states.

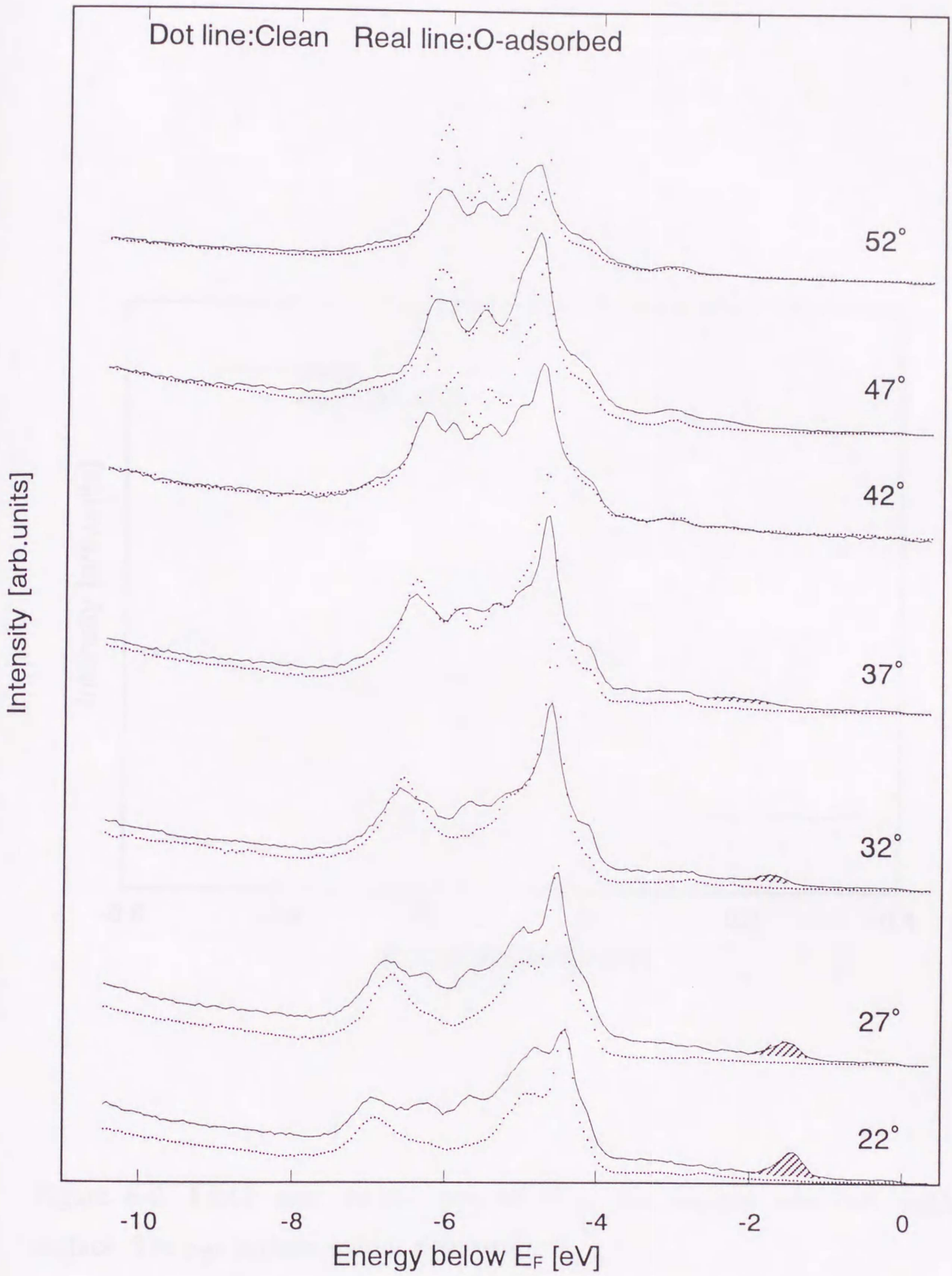

Figure 6-7(b). AREDCs measured using HeI radiation as a function of the emission angle θe (22°~52°) along the <001> direction ($\overline{\Gamma}$-$\overline{Y}$).

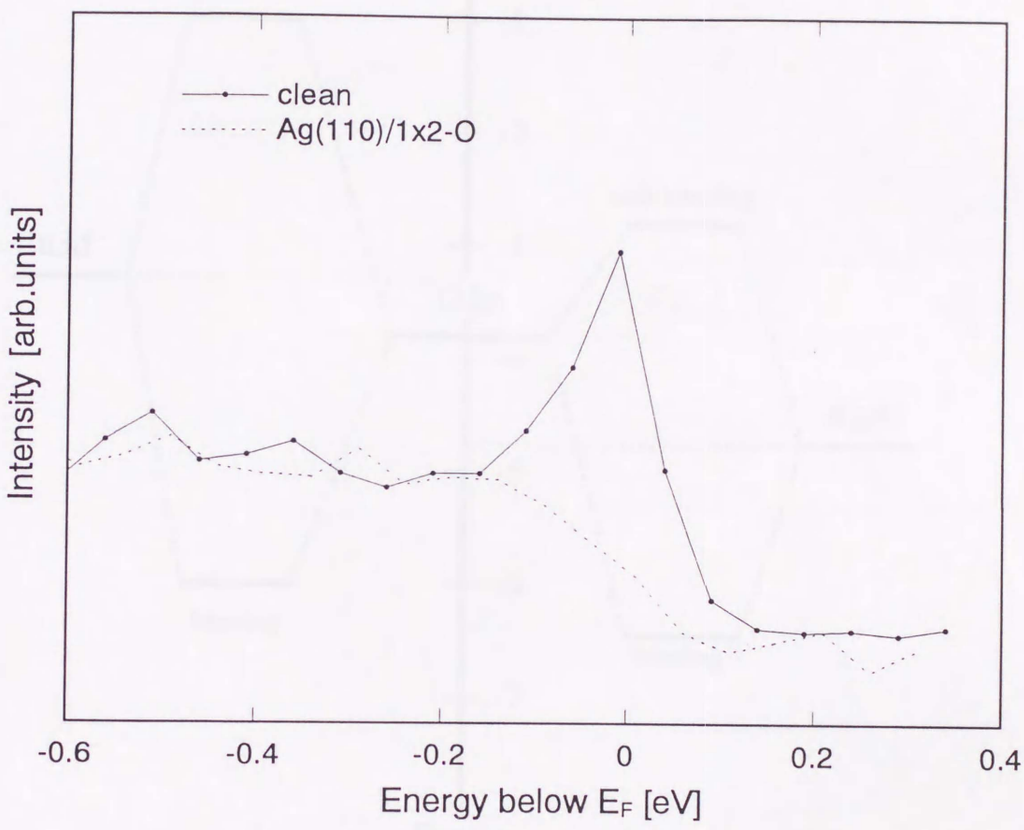

Figure 6-8. EDCs near Fermi edge of clean and oxygen adsorbed Ag(110) surface. The *s-p* surface state is observed.

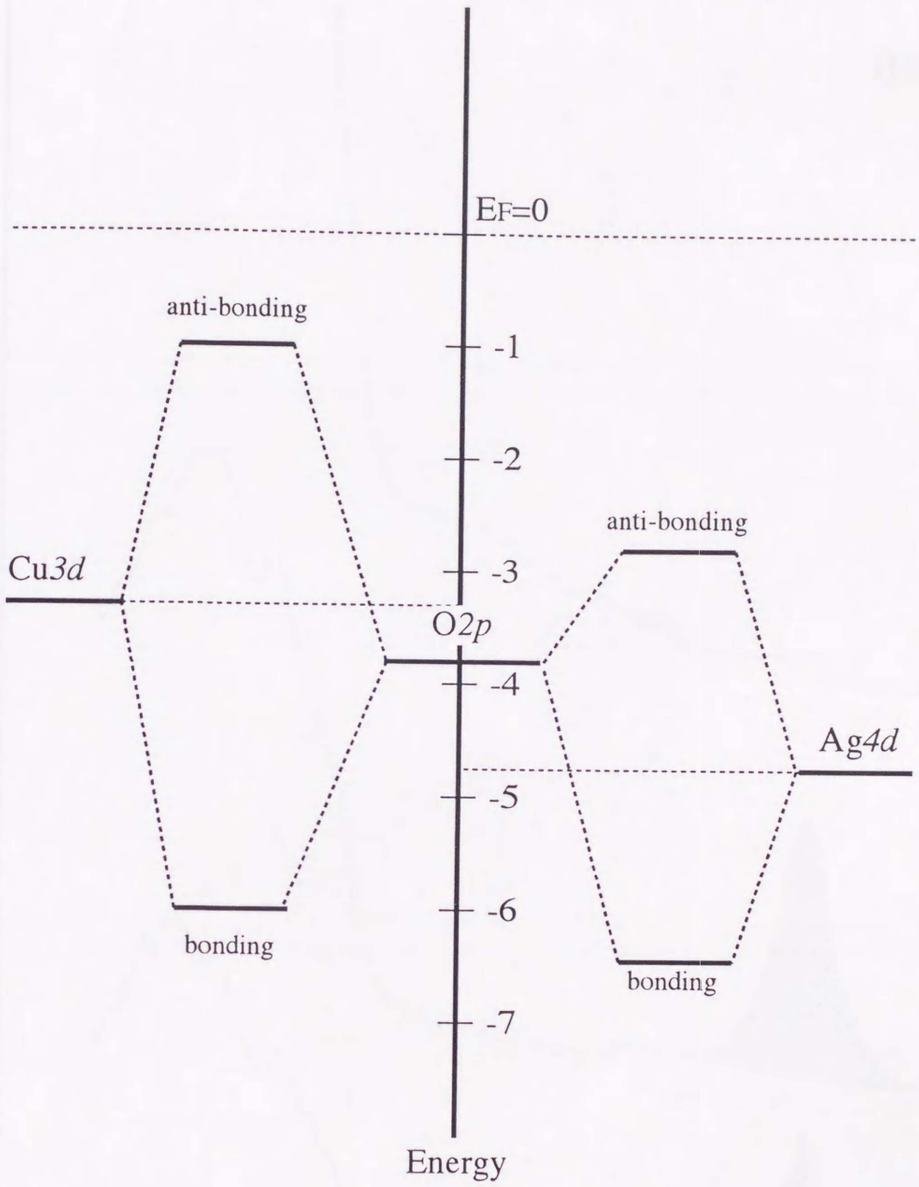

Figure 6-9. Schematic energy diagram of Ag*4d*, Cu*3d* and O*2p* level and their bonding and anti-bonding levels.

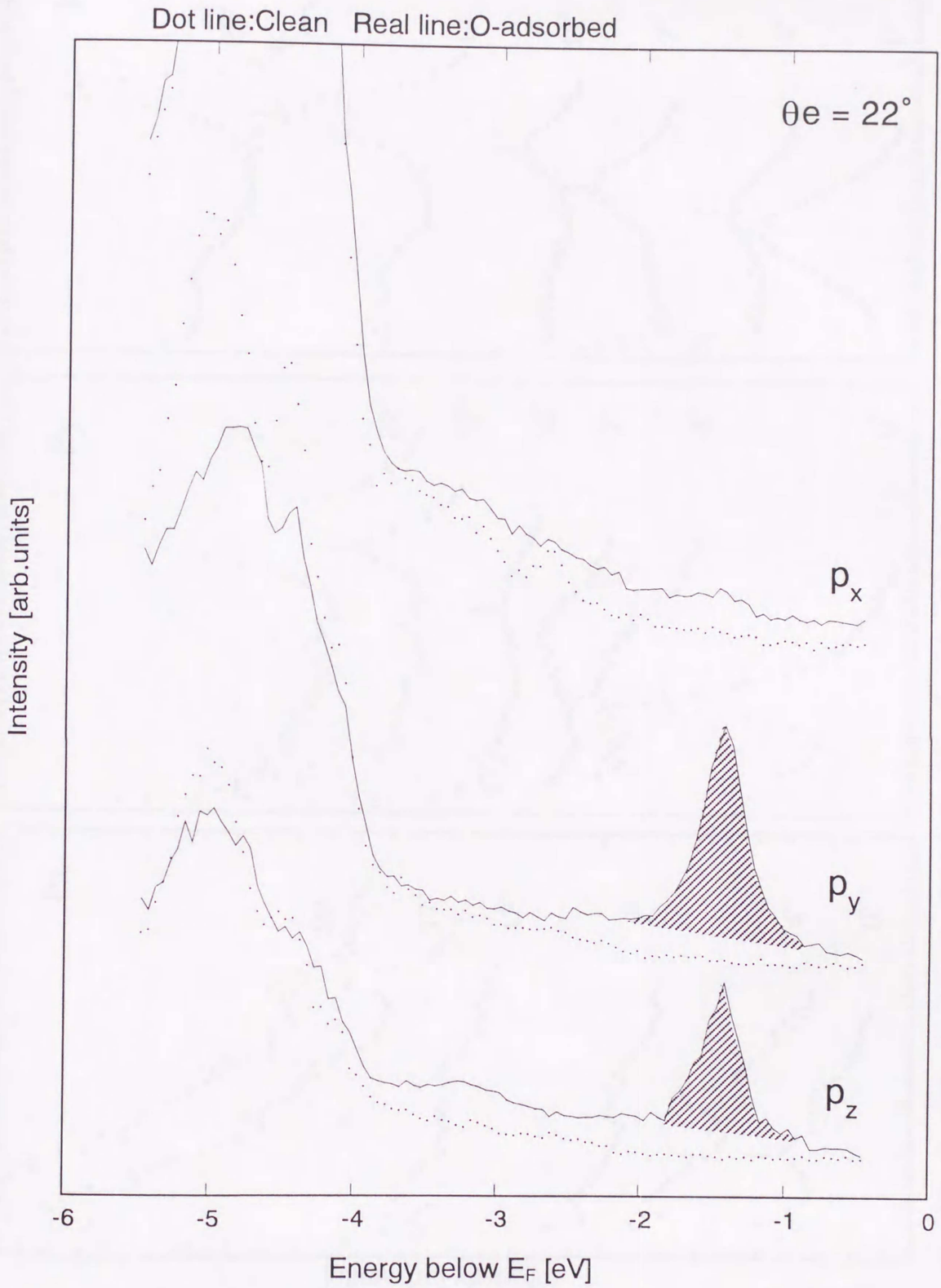

Figure 6-10. EDCs of clean and Ag(110)/2x1-O surface measured using linearly polarized HeI radiation at detection angle θe=22° along the <001> direction ($\overline{\Gamma}$-$\overline{Y}$) ; (p_x) $\hat{A}$ parallel to <$\overline{1}$10> and θ_I=20° (p_y) $\hat{A}$ perpendicular to <$\overline{1}$10> and θ_I=20° (p_z) $\hat{A}$ perpendicular to <$\overline{1}$10> and θ_I=70°.

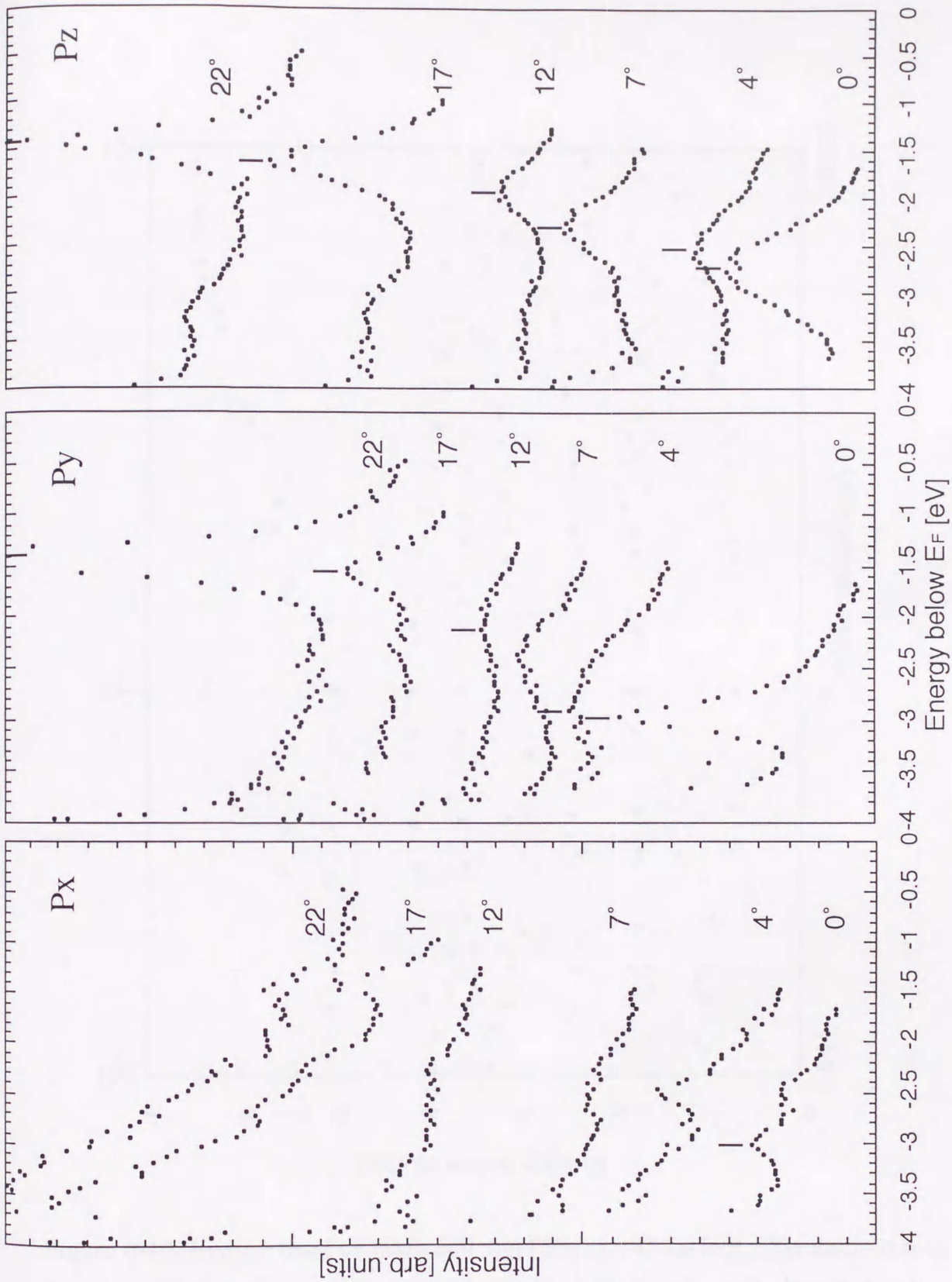

Figure 6-11. AREDCs Ag(110)/2X1-O surface measured using linearly polarized HeI radiation at detection angle θe(0°~22°) along the <001> direction ($\bar{\Gamma}$-$\bar{Y}$); (p_x) $\hat{A}$ parallel to <$\bar{1}$10> and θ_I=20° (p_y) $\hat{A}$ perpendicular to <$\bar{1}$10> and θ_I=20° (p_z) $\hat{A}$ perpendicular to <$\bar{1}$10> and θ_I=70°.

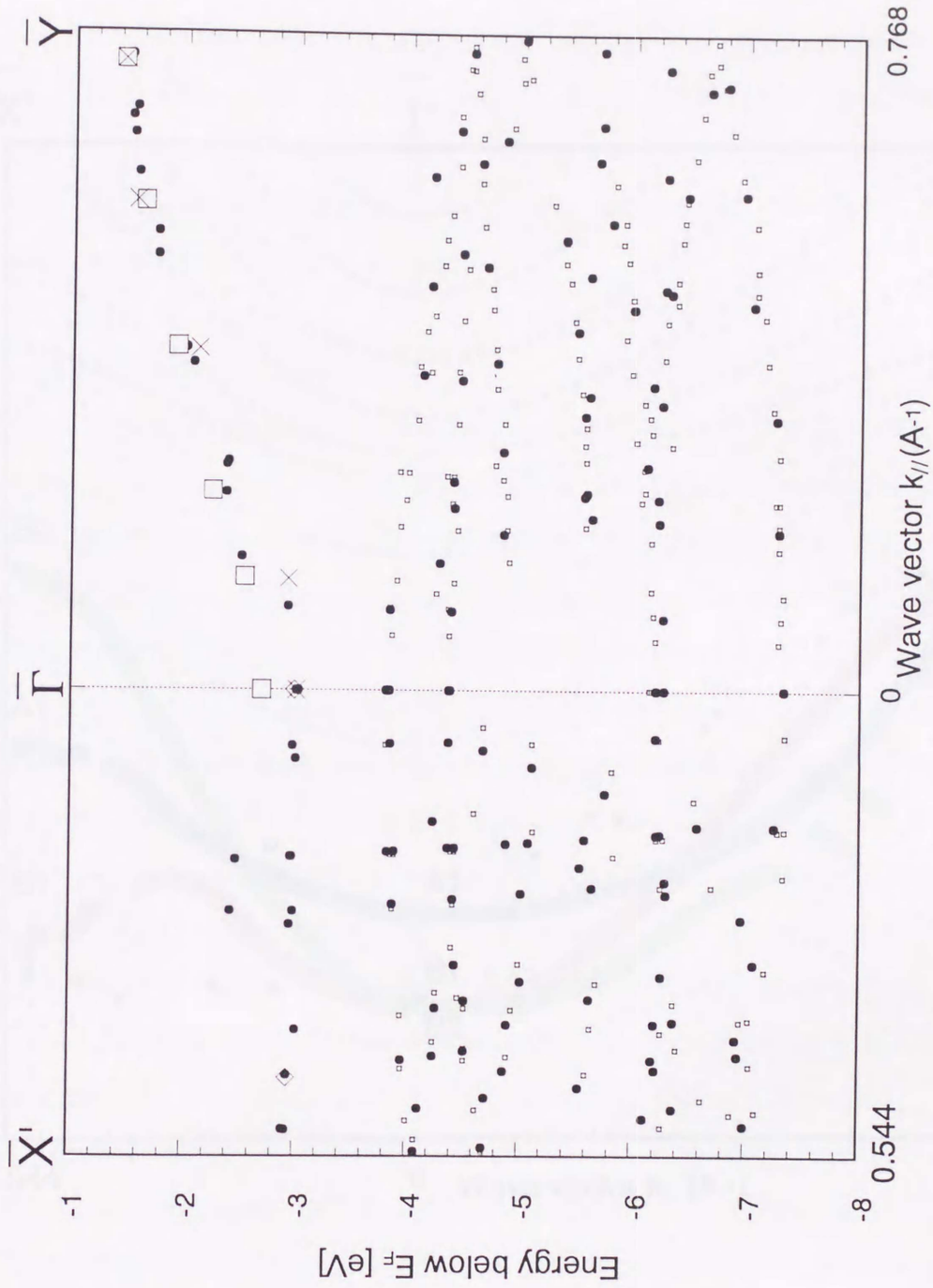

Figure 6-12. Energy band of clean and Ag(110)/2x1-O surface. Symbolic marks for Ag(110)/2x1-O surface denote: (•) hν=21.22 eV and hν=40.8 eV, unpolarized; (◇) hν=21.22 eV, p_x feature; (×) hν=21.22 eV, p_y feature; (□) hν=21.22 eV, p_z feature; and for clean surface: small (□) hν=21.22 eV, unpolarized.

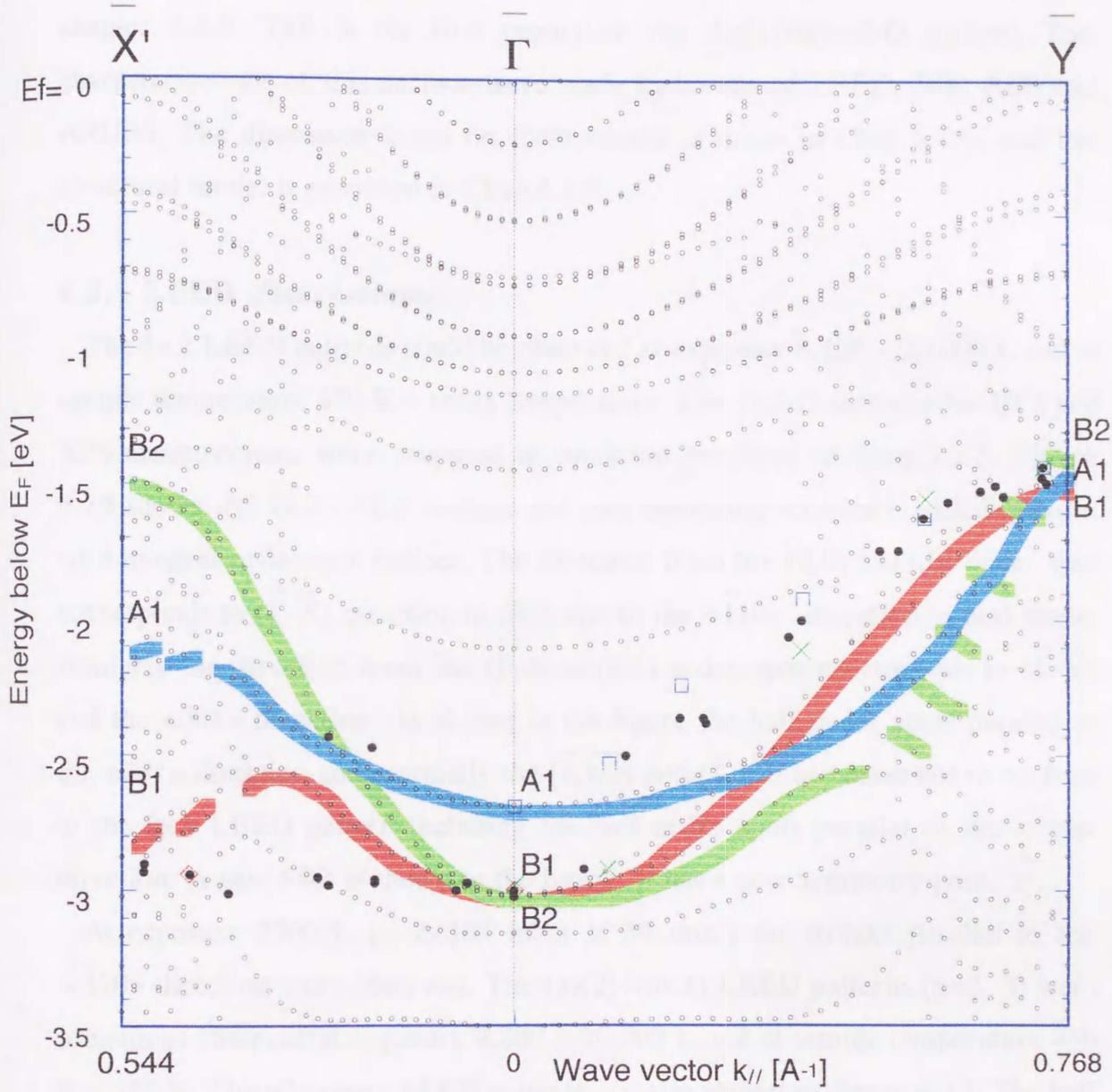

Figure 6-13. Plots of calculated energy bands along the <001> direction (denoted by open circles) compared with experimental points given in Fig.6-12. Each calculated band, p_x-band(B1), p_y-band(B2) and p_z-band(A1), is shaded for the purpose of easy recognition of the correspondence between calculated bands and experimental points.

6.2 Ag(110)/1x2-O surface

The Ag(110)/1x2-O surface was observed through the procedure described in chapter 3.2.5. This is the first report on the Ag(110)/1x2-O surface. The characterizations of this surface were made by means of LEED, WF, XPS and ARUPS. The discussion based on these results is made in Chap.6.2.6, and the structural model is proposed in Chap.6.2.7.

6.2.1 LEED observations

The 1x2 LEED patterns could be observed at exposure 8,120 ~ 20,000 L and at sample temperature 470 K ~ room temperature. The 1x2-O surfaces for UPS and XPS measurements were prepared at condition described in Chap.3.2.5. Figure 6-14 shows the 1x2 LEED pattern and corresponding schematic LEED pattern with integral order spot indices. The direction from the (0,0) to (1,0) order spot corresponds to $(\bar{\Gamma}\text{-}\bar{X})$ direction in SBZ and to the $<\bar{1}10>$ direction in real space, similarly the direction from the (0,0) to (0,1) order spot corresponds to $(\bar{\Gamma}\text{-}\bar{Y})$ and the <001> direction. As shown in the figure the half order spots parallel to the <001> direction and especially the $(\bar{1},\overline{1/2})$ and $(\bar{1},1/2)$ are observed in contrast to the 2x1 LEED pattern including the half order spots parallel to the $<\bar{1}10>$ direction. A new SBZ is shown in the figure. It has a new symmetry point $\overline{Y'}$.

At exposure 2700 L (= $2\text{x}10^{-6}$ mbar x 30 min.) the streaks parallel to the $<\bar{1}10>$ direction were observed. The (1x2)+(nx1) LEED patterns (n=2, 3) were sometimes observed at exposure 9,200 ~ 20,000 L and at sample temperature 450 K ~ 325 K. The schematic LEED patterns are also shown in figure 6-14. The half or 1/3 order spots parallel to the $<\bar{1}10>$ direction appeared with half order spots parallel to the <001> direction. This is interpreted that the 1x2 and nx1 domains coexist within the LEED electron beam area. Discussions about this are described in Chap.6.2.6.

6.2.2 Work function

The WF change of Ag(110)/1x2-O surface was measured: $\Delta\Phi = 0.59 \pm 0.07$ eV for 1x2-O surface. This is almost as same as that of the Ag(110)/3x1-O surface. And it is important that the $\Delta\Phi$ increase is an evidence that the adsorbates behave as the electron acceptor.

6.2.3 Oxygen coverage

Figure 6-15 shows the example of the XPS EDC of Ag(110)/1x2-O surface at incident angle 25° and detection angle 50°. The ratio of the O*2p* to Ag*4d* peak intensities is almost as same as that of the Ag(110)/2x1-O surface (see Fig.6-5). It is established that the oxygen coverage of the Ag(110)/2x1-O surface is 0.5 ML as described in Chap.6.1.3. So the oxygen coverage of the Ag(110)/1x2-O surface also is estimated to 0.5 ML.

The oxygen coverage of Ag(110)/1x2-O surface was quantitatively also estimated from XPS measurements with approximations described in Chap.6.1.3. The measurements were performed at two measurement arrangements: incident angle 0° and emission angle 75°, incident angle 25° and emission angle 50° for the purpose of averaging the anisotropies [41] due to diffraction effect, and totally done five times.

The average $\theta_{(1\times2)}$ was estimated:

$\theta_{(1\times2)} = 0.47$ ML .

6.2.4 Photoemission study of Ag(110)/1x2-O surface

Figure 6-16 shows the normal emission EDCs of the clean and Ag(110)/1x2-O surface measured using HeI and HeII radiations. The oxygen-induced features were observed at energy -3.1 eV in both spectra, whereas the Ag*4d* band states shifted their energies.

This is a typical method for confirming whether the feature is a state localized on the surface or not. If the state is localized on the surface and do not have a

dispersion along the <110> direction (parallel to the surface normal), the kinetic energy of the photoelectron emitted to the surface normal changes as same as the incident light energy difference. On the other hand, if the state has a dispersion along the <110> direction, i.e., the bulk state, the kinetic energy of the photoelectron changes the energy corresponding to the dispersion in addition to the incident light energy difference. So the states localized on the surface do not shift the energies with respect to the E_F, when the states are plotted as a function of energy below E_F. Thus these features at -3.1 eV are the states localized on the surface.

The O*2p* anti-bonding states of the normal emission EDCs of Ag(110)/2x1-O and 3x1-O surface are located at almost the same binding energy. When the energy diagram described in Chap.6.1.4 (Fig.6-9) also could be applied for the Ag(110)/1x2-O surface, i.e., these features at -3.1 eV are originated from a similar O*2p*-Ag*4d* bonding, then these features should have O*2p* character. For the purpose of confirming whether the features have O*2p* character or not, it is useful to consider the atomic photoionization cross-section ratios σ(O*2p*)/σ(Ag*4d*) when the photon energy is increased from 21.22 eV (HeI) to 40.8 eV (HeII). They decrease by a factor of 0.283 [40]. This corresponds to the ratios I(O*2p*)/I(Ag*4d*) when the photon energy is increased from 21.22 eV (HeI) to 40.8 eV (HeII), where I(O*2p*) and I(Ag*4d*) are indicated as shaded ares in Fig.6-16. The ratios are,

I(O*2p*)/I(Ag*4d*) = 0.0138 for HeI ;

I(O*2p*)/I(Ag*4d*) = 0.00480 for HeII .

They decrease by a factor of 0.347. It can be said this corresponds to the factor of cross-section ratios when considering the features have also a certain Ag*4d* component. So it is concluded that these features are consistent with the character of O*2p* states.

6.2.5 Angle resolved photoemission study of Ag(110)/1x2-O surface

Sequences of AREDCs were measured at various emission angles for the clean and Ag(110)/1x2-O surface along the <001> direction ($\bar{\Gamma}$-$\bar{Y}$) and along the <$\bar{1}$10> direction ($\bar{\Gamma}$-$\bar{X}$). Figure 6-17 shows examples of AREDCs measured using HeI radiation as a function of the emission angle θe along the <$\bar{1}$10> direction ($\bar{\Gamma}$-$\bar{X}$). Figure 6-18 shows the similar AREDCs along the <001> direction ($\bar{\Gamma}$-$\bar{Y}$).

Measurements using a polarized HeI were performed at several points to characterize the orbital symmetries. Figure 6-19 shows the example of the clean and Ag(110)/1x2-O surface at θe = 7°. The measuring arrangements are the same as for the Ag(110)/2x1-O surface. The states with p_y and p_z symmetry were observed as a shoulder at -2.89 eV and as a sharp peak at -3.11 eV, respectively.

Figure 6-20 shows the energy (k-E) dispersion along the <001> and <$\bar{1}$10> direction. The symbolic marks are the same as in Fig.6-12. Along the <001> direction ($\bar{\Gamma}$-$\bar{Y}$) there is a flat band without any dispersion at -3.1 eV measured using unpolarized HeI, and this can be assigned to the p_z symmetry using the polarization selection rules. This can be observed through the first SBZ ($\bar{\Gamma}$ to $\bar{Y}$). The states with p_y symmetry were observed at several points, but their intensities were very weak compared with that of the state with p_z symmetry (for example, see Fig.6-19). This makes an assignment of the p_y band to be difficult. The states with p_x symmetry were not observed. As for the band obtained by unpolarized HeI radiation, it has a periodicity which is consistent with the new SBZ. However some states with p_y symmetry obtained by polarized HeI radiation does not belong to the periodicity of the new SBZ, and the origins of these features may be different from that of the O-2p_y state. Along the <$\bar{1}$10> direction ($\bar{\Gamma}$-$\bar{X}$), single band with a slight dispersion could be observed only to half way from $\bar{\Gamma}$ to $\bar{X}$.

6.2.6 Other discussions

It is necessary to discuss whether this reconstructed surface observed as the 1x2 pattern by LEED is induced by the oxygen adsorption, because this is the first observation. Some of the results and discussions above can be the evidences.

At first, the oxygen gas introduced to the vessel was checked by the RGA. The impurities like CO was 1% or less. The impurity atom peak was not observed in the XPS spectra of the Ag(110)/1x2-O surface, and only oxygen peak was observed. The binding energy of this feature is almost the same as the O2*p* anti-bonding states of the normal emission UPS EDCs of the Ag(110)/2x1-O and 3x1-O surface, and is consistent with the interpretation of the energy diagram described in Chap.6.2.4.

It is described that the (1x2)+(nx1) LEED patterns (n=2, 3) were sometimes observed and this is interpreted that the 1x2 and nx1 domains coexist in Chap. 6.2.1. The normal emission EDCs of Ag(110)/[(1x2)+(2x1)]-O surface measured using polarized HeI are shown in figure 6-21 with those of Ag(110)/(1x2)-O and (2x1)-O surface. As shown in the figure both peaks of the (1x2)-O and (2x1)-O surfaces can be assigned in the EDCs of Ag(110)/[(1x2)+(2x1)]-O surface. This also suggests that the 1x2 and 2x1 domains do coexist and patches of them are formed. This supports the interpretation in Chap.6.2.1 and confirms that this reconstructed surface observed as the 1x2 pattern by LEED is induced by the oxygen adsorption.

In addition, as described in Chap.6.2.2 the WF change is an increase. This is consistent with that the adsorbates are the oxygen atoms. In addition, it has been reported that the WF change of O_2 physisorbed surface is a decrease [25], so this is not the physisorption. As described in Chap.6.2.4 the features in Fig.6-16 have O2*p* character, resulting from comparing their photon energy dependence with the atomic photoionization cross-section.

Several systems which shows the 1x2 LEED pattern have been known and the photoemission studies about these have been reported; for example, OH on

Ag(110) [43]. However, in this case the 1x2 LEED pattern was not observed at room temperature. As the other possible adsorbates, the feature at -2.3, -3.6, -8.6 eV for the CO_3 chemisorbed surface [27], the feature at -1.1 eV for the O_2 chemisorbed surface [25] and the feature at -2.3 eV for the CO chemisorbed surface [44] have been reported in the normal EDC of each adsorbate/Ag(110) surface. They were not observed in Fig.6-16, either. We can therefore conclude that the Ag(110)/1x2-O surface in the present study is a reconstructed surface induced by dissociated oxygen atoms.

6.2.7 Ag(110)/1x2-O model and application for LCAO calculation

For the purpose of applying the simplified-LCAO calculation for the Ag(110)/(1x2)-O surface, we assume the 1x2 missing row (MR) model where every second $<\bar{1}10>$ row is missing. Figure 6-22 shows a top-view and side-view of the 1x2 MR-model, neglecting the oxygen atoms. There are the topmost Ag rows and troughs along the $<\bar{1}10>$ direction. The topmost layer, the first and second substrate layers and the new SBZ are indicated.

The reason why we assumed the 1x2 MR-model is the half order spot intensity of the 1x2 LEED pattern. As described in Chap.6.2.1 the half order spots could be observed as almost the same intensity as the fundamental spots. When the electron beam with kinetic energy 100 eV is irradiated to the surface at incident angle 0°, the differential cross-sections for scattering at 2° from the surface normal in units of $Å^2$ per steradian $d\sigma/d\Omega$ of the oxygen and silver are [45]:

$d\sigma/d\Omega(O) = 0.265\ [Å^2]$

$d\sigma/d\Omega(Ag) = 0.688\ [Å^2]$.

This indicates that the intensity originated from the scattering with the oxygen atom is about 1/3 of that of the Ag atom. As a result; the observation of the 1x2 LEED pattern is ascribed to the 1x1 to 1x2 reconstruction of substrates, not to the ordering of the adsorbed oxygen atoms.

The oxygen coverage of the Ag(110)/1x2-O surface was estimated to 0.5 ML in

Chap.6.2.3. This shows that there is single oxygen atom in the new unit cell of the 1x2 MR-model. Figure 6-23 shows six possible models with various oxygen atom sites satisfying these limitations; the substrate is the reconstructed 1x2 MR model and the oxygen coverage is 0.5 ML. The model 1: the oxygen atom is located at a short bridge-site in the Ag row of topmost layer along the $<\bar{1}10>$ direction. And it has two nearest Ag neighbor atoms. The model 2: at a threefold hollow-site among the single Ag atom of the topmost layer and the two Ag atoms of the first substrate layer, three nearest neighbors. The model 3: at a threefold hollow-site among the two Ag atoms of the topmost layer and the single Ag atom of the first substrate layer, three nearest neighbors. The model 4: at a long bridge-site between the atoms of the first substrate layers, two nearest neighbors. The model 5: at a fourfold hollow-site among the four Ag atoms of the first substrate layers, four nearest neighbors. The model 6: at an atop-site on the Ag atom of the topmost layer, single nearest neighbor. The oxygen and silver atom are assumed as the rigid spheres; a radius of oxygen ion = 1.26 Å, and a radius of silver atom = 1.44 Å. Each oxygen position is decided so that the oxygen ion atom touches each nearest neighbor silver atom.

Figure 6-24 shows each calculation of Ag(110)/1x2-O models together with the experimental results. The LCAO parameters for the Ag-Ag interactions were also adopted from the literature [34]. The Ag-O interactions, sPσ , pPσ , pPπ , Pdσ , Pdπ and surface shift were adopted from the parameters of the Ag(110)/2x1-O surface calculation with some revision. The matrix element is proportional to d^n, where d is the interatomic length [46]:

$\propto d^{-2}$: sPσ, pPσ, pPπ

$\propto d^{-7/2}$: Pdσ, Pdπ .

These parameters were multiplied by the factors resulting from such a consideration, as a function of the O-Ag interatomic length change between these models and the Ag(110)/2x1-O surface model. And only the on-site energy of O orbital E_{Op} was adjusted to fit the calculation with the experimental results on the

whole. The parameters: E_{Op}, $r_{(nn)}$, $r_{(nnn)}$, $Fll_{(nn)}$, $Fld_{(nn)}$, $Fll_{(nnn)}$ and $Fld_{(nnn)}$ are listed in table 6-2, where r is the interatomic length, and Fll and Fld are the factors for sPσ, pPσ and pPπ and for Pdσ and Pdπ, respectively. The notations (nn) and (nnn) denote the nearest and next nearest neighbor, respectively. The symbolic marks are the same as in Fig.4-5.

When comparing the p_z band without any dispersion along $\overline{\Gamma}$-$\overline{Y'}$, the model 1 or 6 seems to reproduce the experiment. On the other hand, if the states with p_y symmetry in the first SBZ are originated from the O-2p_y band, it disperses *ca.* 0.3 eV. In this case, a similar dispersion is reproduced by the model 4 or 5. Therefore at present it should be a conclusive evidence to reveal the p_y and/or p_x band by more carefully ARUPS study.

Along the direction <$\bar{1}$10> direction ($\overline{\Gamma}$-$\overline{X}$), the dispersion of the p_y and p_z bands are calculated as about 0.6 $\pm$ 0.3 eV not so depending on the models. So the p_y and p_z band dispersions *ca.* 0.6 $\pm$ 0.3 eV are expected. Figure 6-25 shows the fitting curve together with the experimental energy band along $\overline{\Gamma}$-$\overline{X}$, assuming the cosine function as the simple dispersion curve introduced in Chap.6.1.5 (the cosine corresponds to the real part of exponential). The dispersion width is simulated to ~0.3 eV so that the LCAO calculation is plausible, while the experimental band is not observed from the half way to $\overline{X}$. As shown in those figures, however, some calculated bands across the oxygen induced bands along $\overline{\Gamma}$-$\overline{X}$ appear and hybridize with some oxygen induced bands. They are assigned as the Ag5*s* bands. This may make difficult to measure the oxygen induced bands along $\overline{\Gamma}$-$\overline{X}$.

As for the p_x band, there are little dispersion on all models. If the significant p_x dispersion would be observed experimentally, it must be necessary to introduce the O-O interaction.

The calculations of all models could not reproduce the experiment so well as the cases of the Cu, Ni and Ag(110)/2x1-O surfaces. Then some revisions may be

necessary to reproduce the result more accurately. As one of reasons which prevent reproducing, the few bands revealed their symmetries make fitting difficult. More studies of revealing the band symmetries should be needed; more detailed ARUPS measurements by polarized HeI or PES measurements by synchrotron radiation. As for the calculation, the following improvements may be effective: to change the O-Ag interatomic length, to treat the parameters of O-Ag interactions as adjustable parameters, and introduction of the O-O interactions. The on-site energy of O2*p* was revised 0.15~0.3 eV close to the E_F, i.e., opposite to the on-site energy of Ag4*d* (corresponds to Ag4*d* band binding energies) to fit the calculation with the result on the whole as in table 6-2. This can be a factor which reduces the dispersion comparing with that of the Ag(110)/2x1-O surface by equation (6-4). Practically the dispersions of the Ag(110)/1x2-O surface seem to be small than that of the Ag(110)/2x1-O surface. In addition, the shift of E_{Op} to the E_F is inconsistent with the experimental band shift (from ~-3.0 eV of 2x1 to ~-3.1 eV of 1x2 surfaces at $\overline{\Gamma}$). So it is required that the two-center parameters of the Ag(110)/1x2-O surface are smaller than those of the Ag(110)/2x1-O surface. Therefore to treat the parameters of O-Ag interactions as adjustable parameters may be most effective for improvement.

Table 6-2 : LCAO parameters of Ag(110)/1x2-O surface

	Model1	Model2	Model3	Model4	Model5	Model6	2x1
E_{Op} (eV)	-2.68	-2.58	-2.58	-2.58	-2.58	-2.73	-2.88
$r_{(nn)}$ (Å)	2.70	2.70	2.70	2.70	2.70	2.70	2.04
$r_{(nnn)}$ (Å)	4.24	*	*	3.52	3.91	3.95	3.53
$Fll_{(nn)}$	0.570	0.570	0.570	0.570	0.570	0.570	*
$Fld_{(nn)}$	0.374	0.374	0.374	0.374	0.374	0.374	*
$Fll_{(nnn)}$	0.692	*	*	1.065	0.812	0.798	*
$Fld_{(nnn)}$	0.524	*	*	1.116	0.695	0.674	*

Notation r is the interatomic length, and Fll and Fld are the multiplication factors. sPσ, pPσ and pPπ are multiplied by Fll, and Pdσ and Pdπ are multiplied by Fld. (nn) and (nnn) denote the nearest and next nearest neighbor, respectively. The next nearest neighbor is not considered in model 2 and 3. The notation 2x1 means the 2x1 missing row model explained in Chap.2.2.3

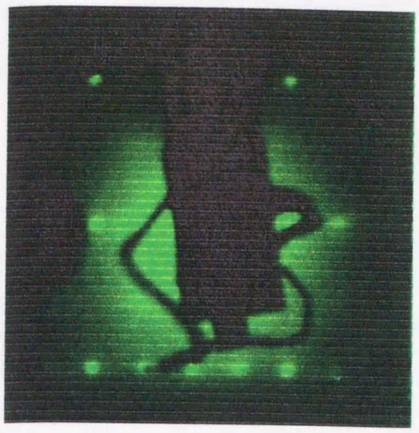

(a) 1x2 LEED

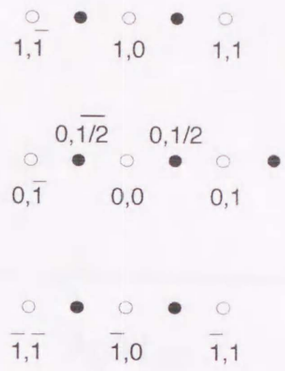

(b) Schematic LEED pattern
○ : fundamental spot
● : half order spot

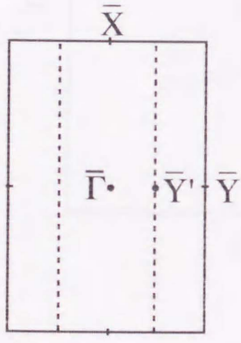

(c) New SBZ of Ag(110)/1x2-O

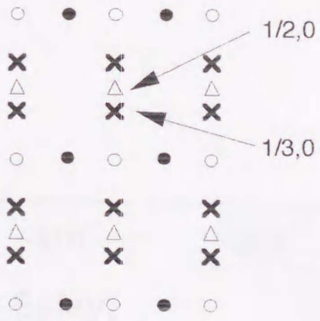

(d) Schematic LEED patterns of the Ag(110)/ (1x2)+(nx1)-O
△ : 2x1
✕ : 3x1
● : 1x2

Figure 6-14. (a) 1x2 LEED pattern. (b) Schematic 1x2 LEED pattern. (c) New SBZ of Ag(110)/1x2-O surface. (d) Schematic LEED patterns of Ag(110)/ (1x2)+(nx1)-O surface (n=2 and 3).

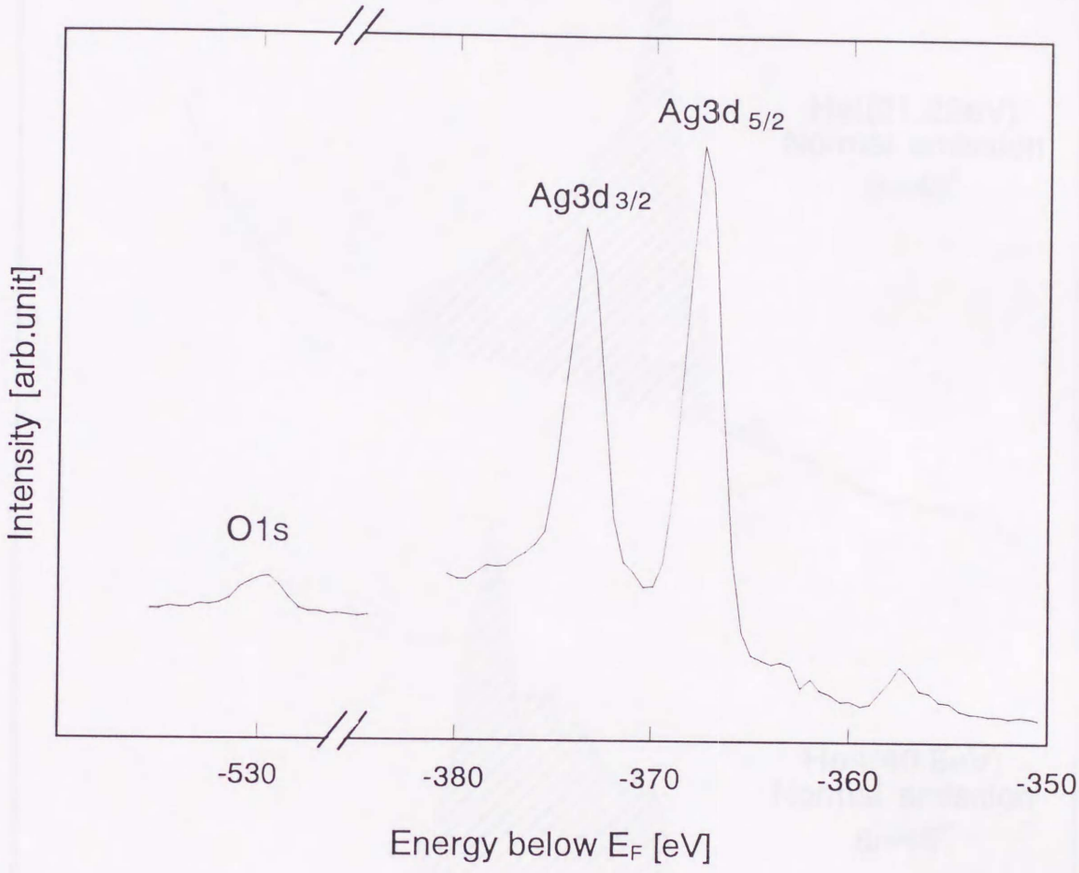

Figure 6-15. XPS EDC of Ag(110)/1x2-O surface; incident angle 25°, emission angle 50°.

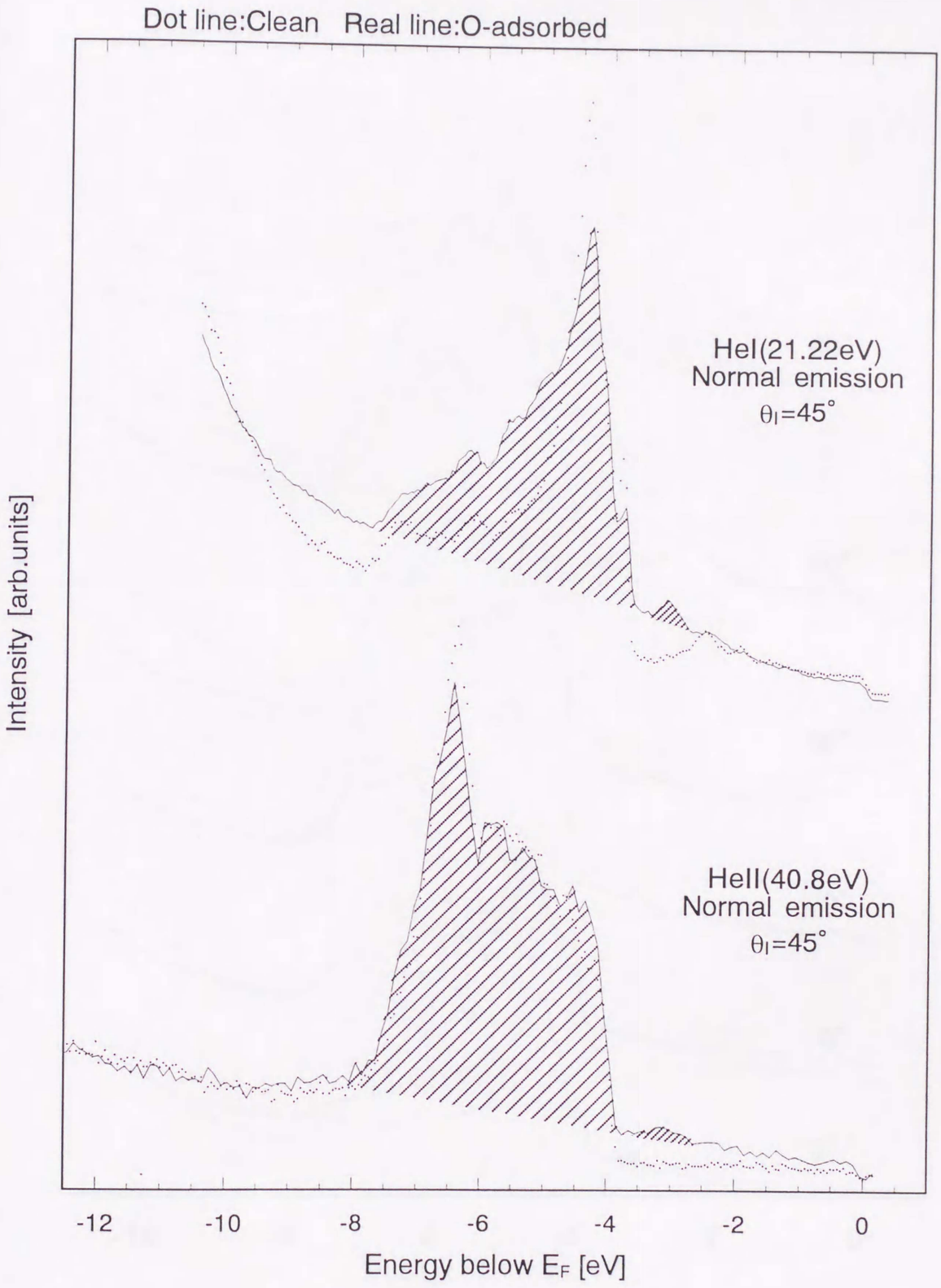

Figure 6-16. Normal emission EDCs of clean and Ag(110)/1x2-O surface measured using HeI and HeII radiations.

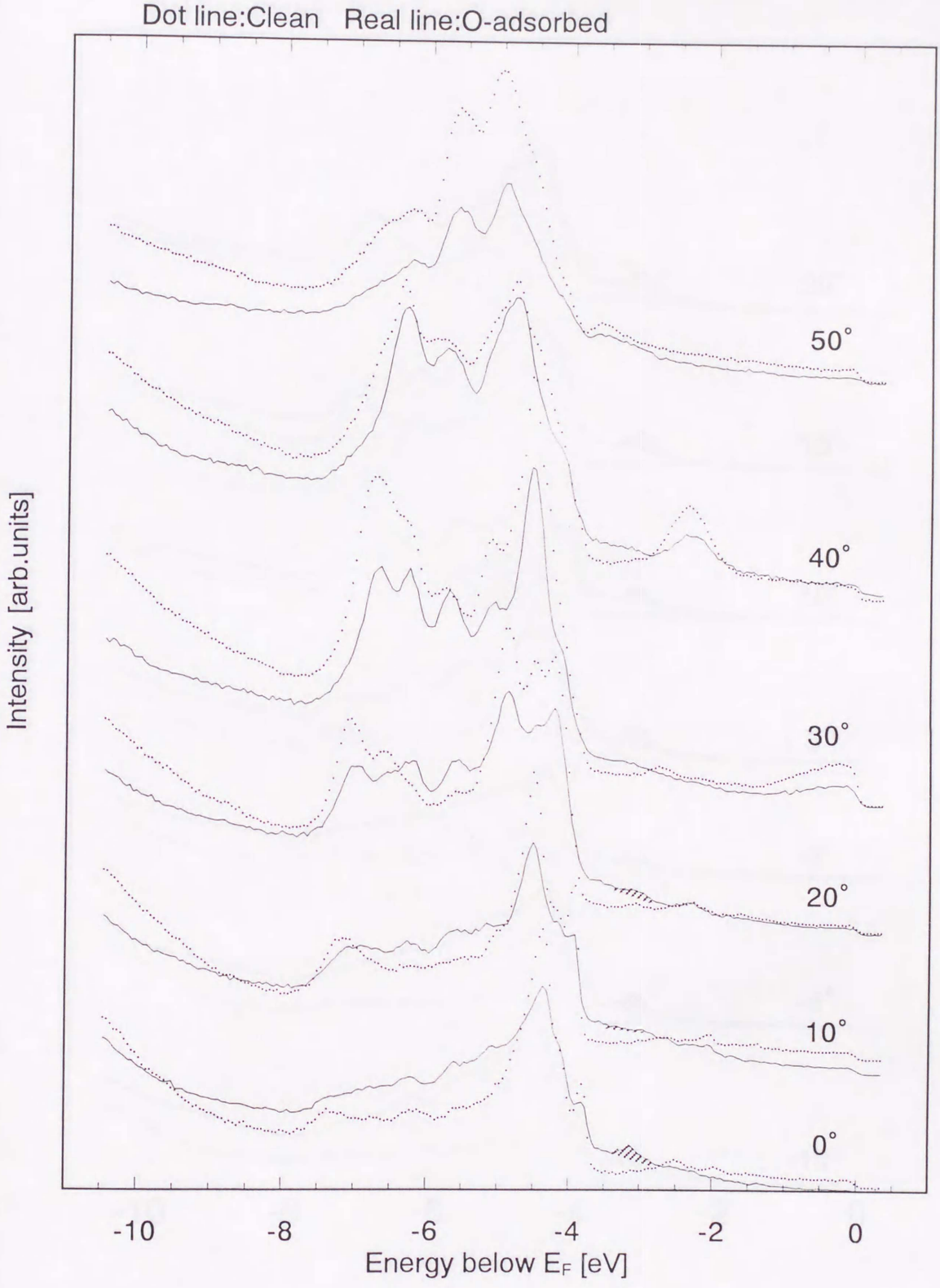

Figure 6-17(a). AREDCs measured using HeI radiation as a function of the emission angle θe (0°~50°) along the <$\bar{1}$10> direction ($\bar{\Gamma}$-$\bar{X}$). The shaded areas indicate the O-induced states.

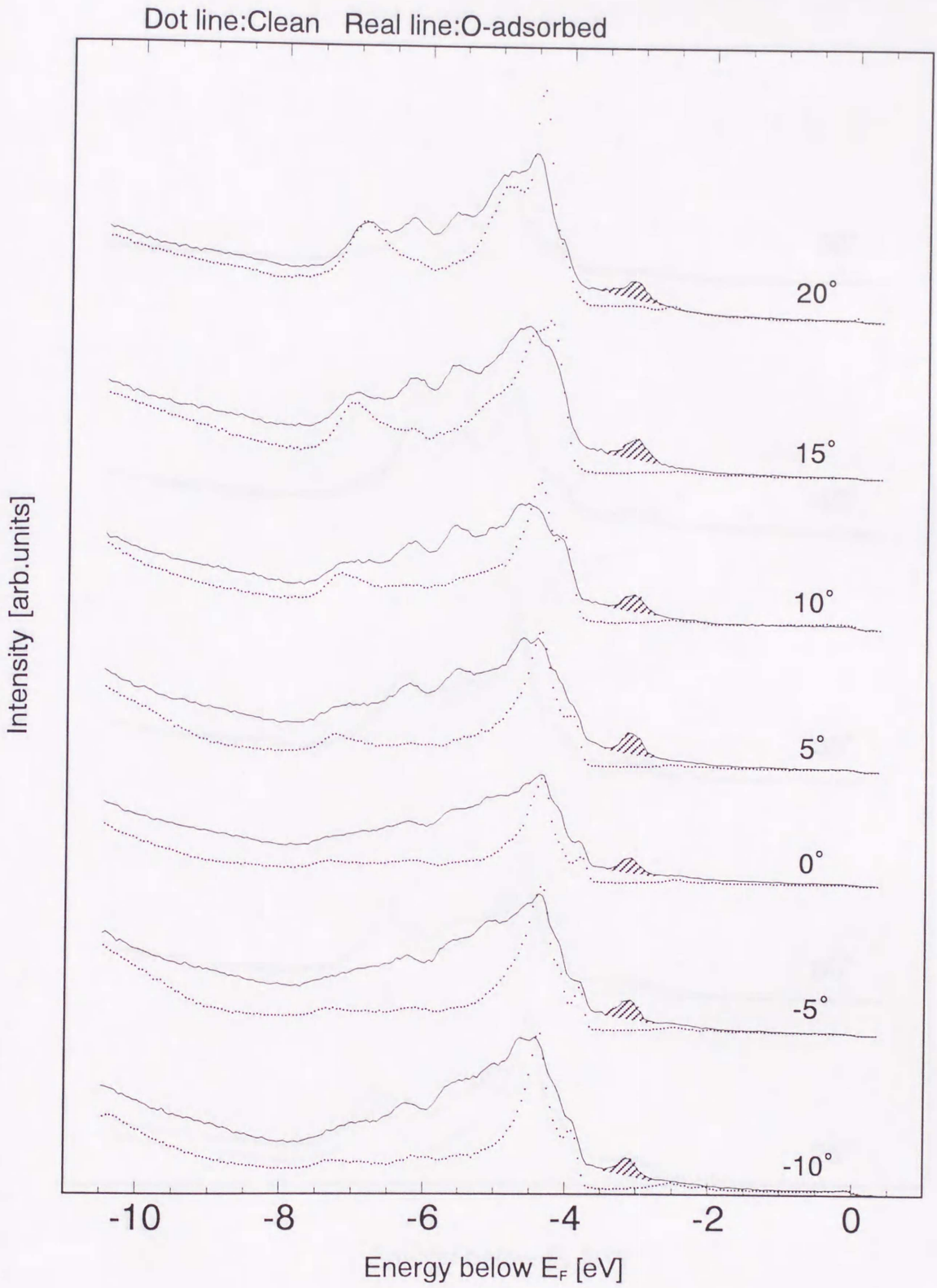

Figure 6-18(a). AREDCs measured using HeI radiation as a function of the emission angle θe (-10°~20°) along the <001> direction ($\overline{\Gamma}$-$\overline{Y}$). The shaded areas indicate the O-induced states.

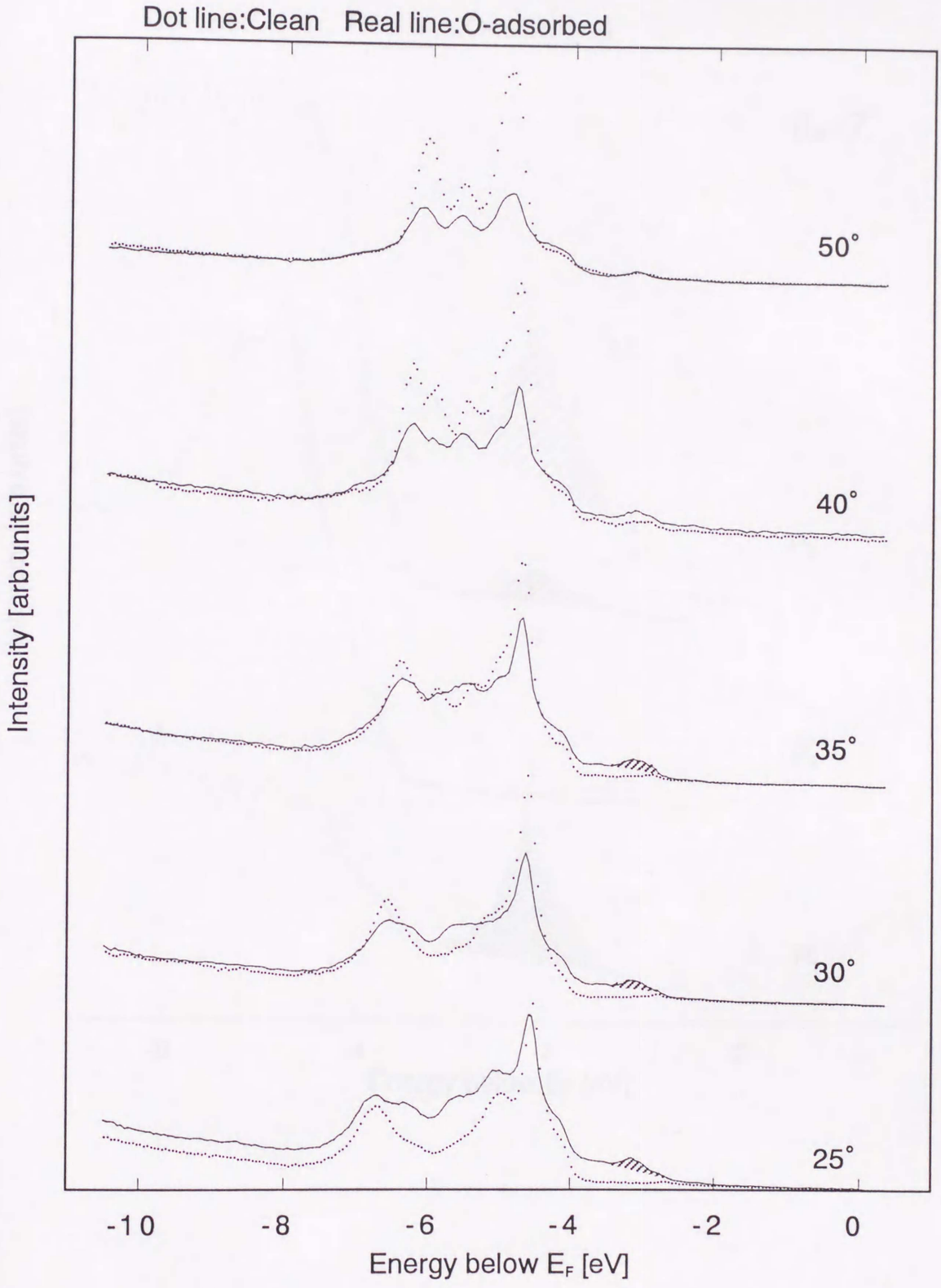

Figure 6-18(b). AREDCs measured using HeI radiation as a function of the emission angle θe (25°~50°) along the <001> direction ($\overline{\Gamma}$-$\overline{Y}$).

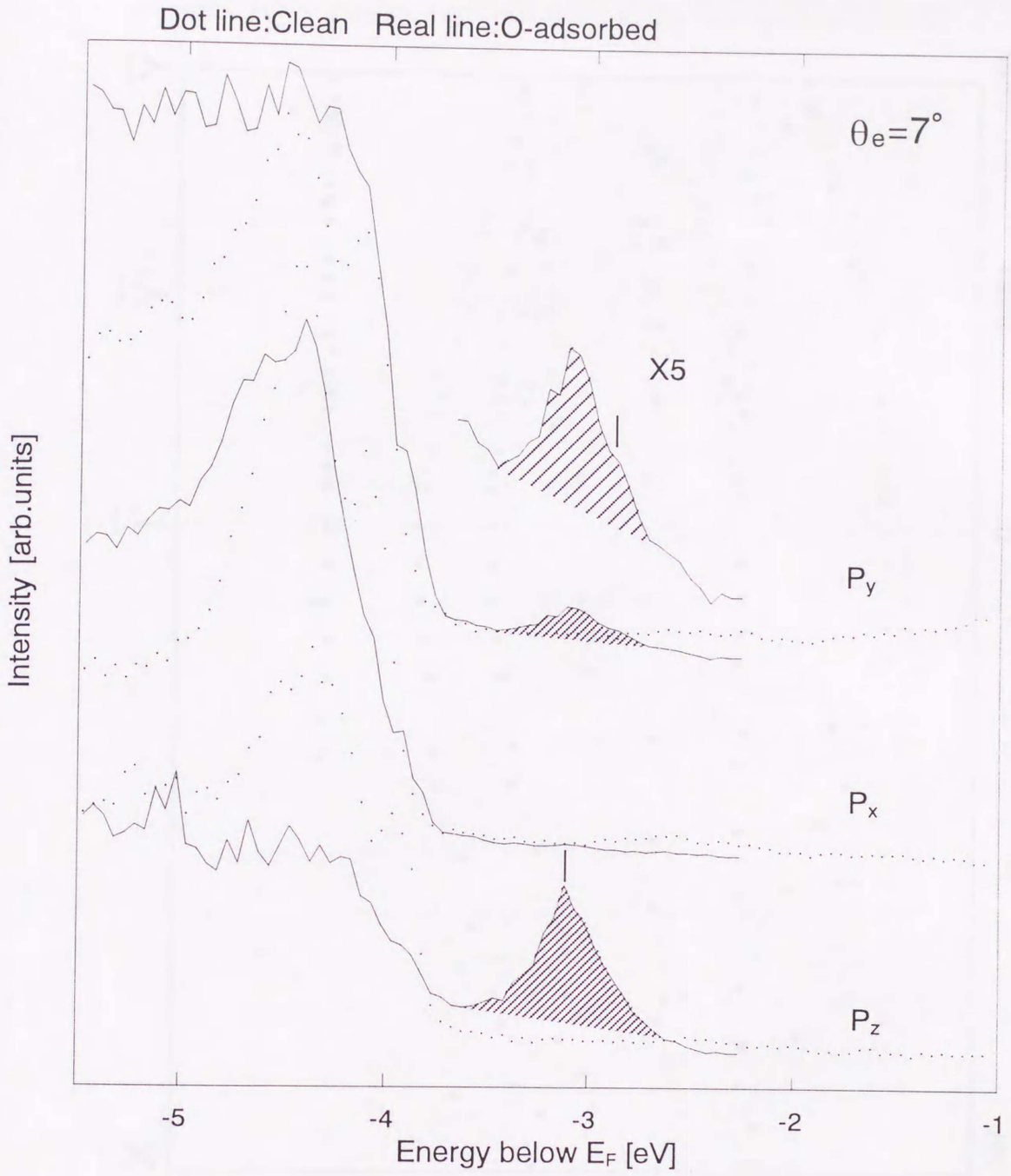

Figure 6-19. EDCs of clean and Ag(110)/1x2-O surface measured using linearly polarized HeI radiation at detection angle θe=7° along the <001> direction ($\bar{\Gamma}$-$\bar{Y}$) ; (p_x) $\hat{A}$ parallel to <$\bar{1}$10> and θ_I=20° (p_y) $\hat{A}$ perpendicular to <$\bar{1}$10> and θ_I=20° (p_z) $\hat{A}$ perpendicular to <$\bar{1}$10> and θ_I=70°.

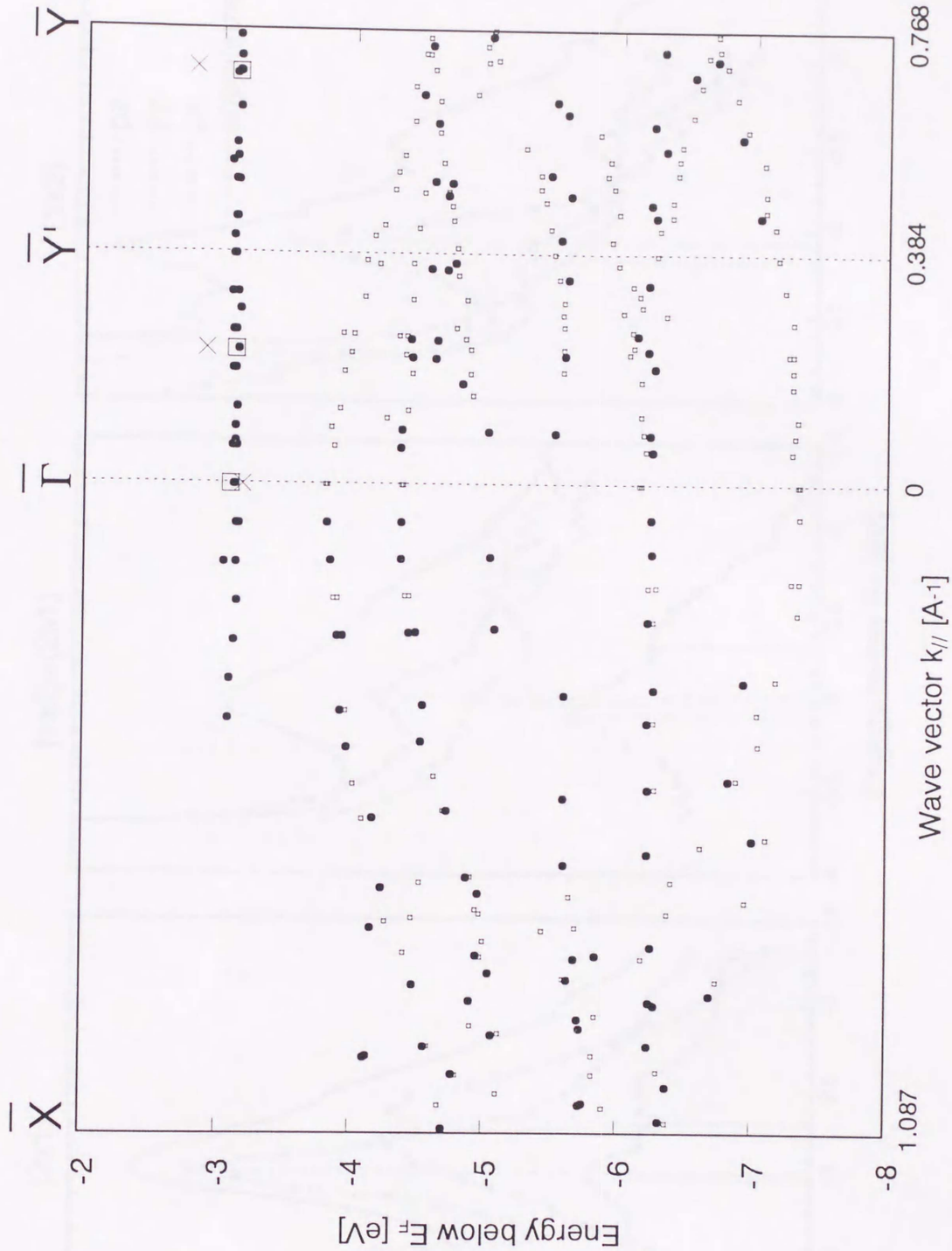

Figure 6-20. Energy band of clean and Ag(110)/1x2-O surface: (•) hν=21.22 eV and hν=40.8 eV, unpolarized; (◇) hν=21.22 eV, p_x feature; (×) hν=21.22 eV, p_y feature; (□) hν=21.22 eV, p_z feature; and for clean surface: small (□) hν=21.22 eV, unpolarized.

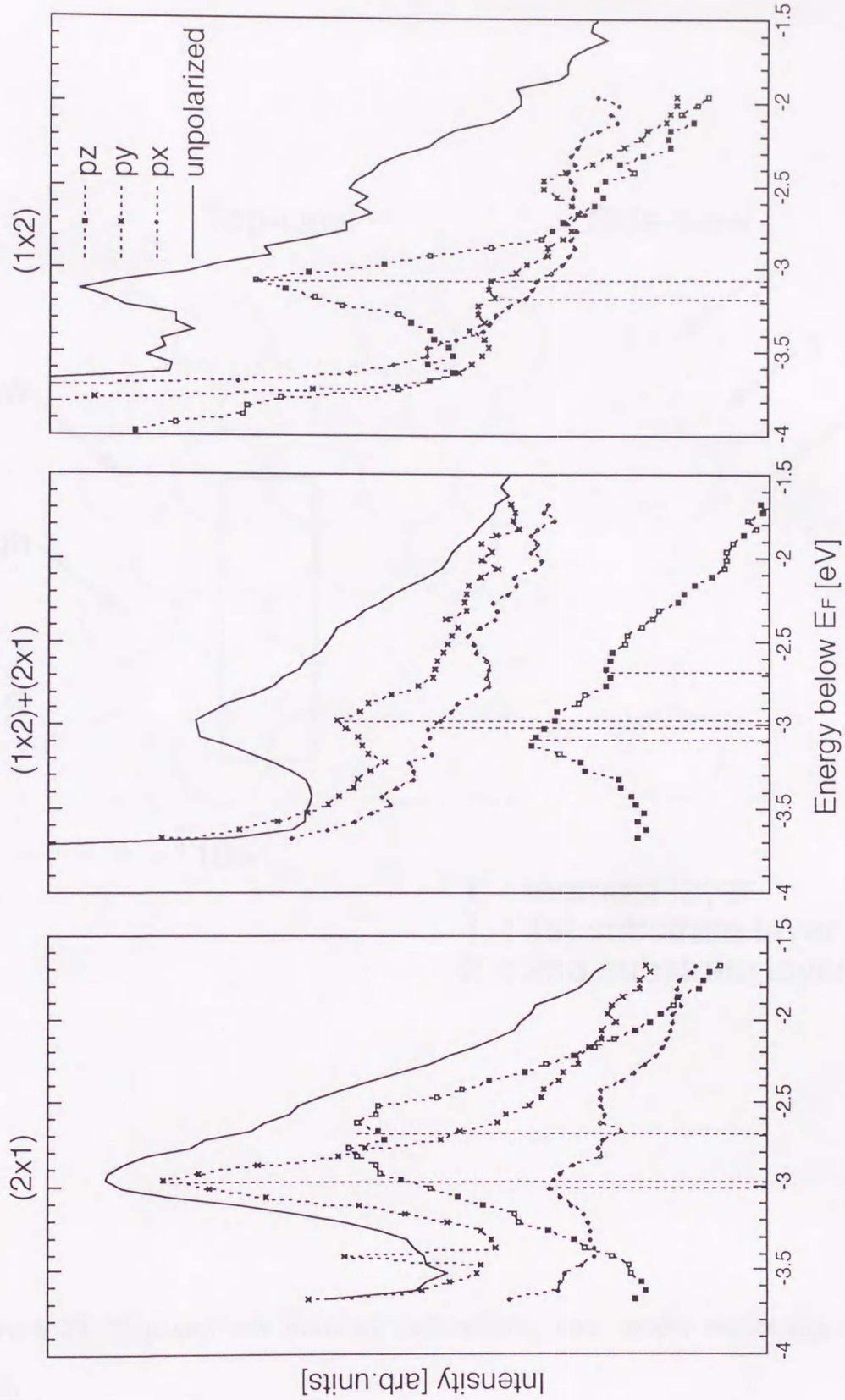

Figure 6-21. Normal emission EDCs of clean and oxygen adsorbed Ag(110) surface measured using linearly polarized HeI radiation.

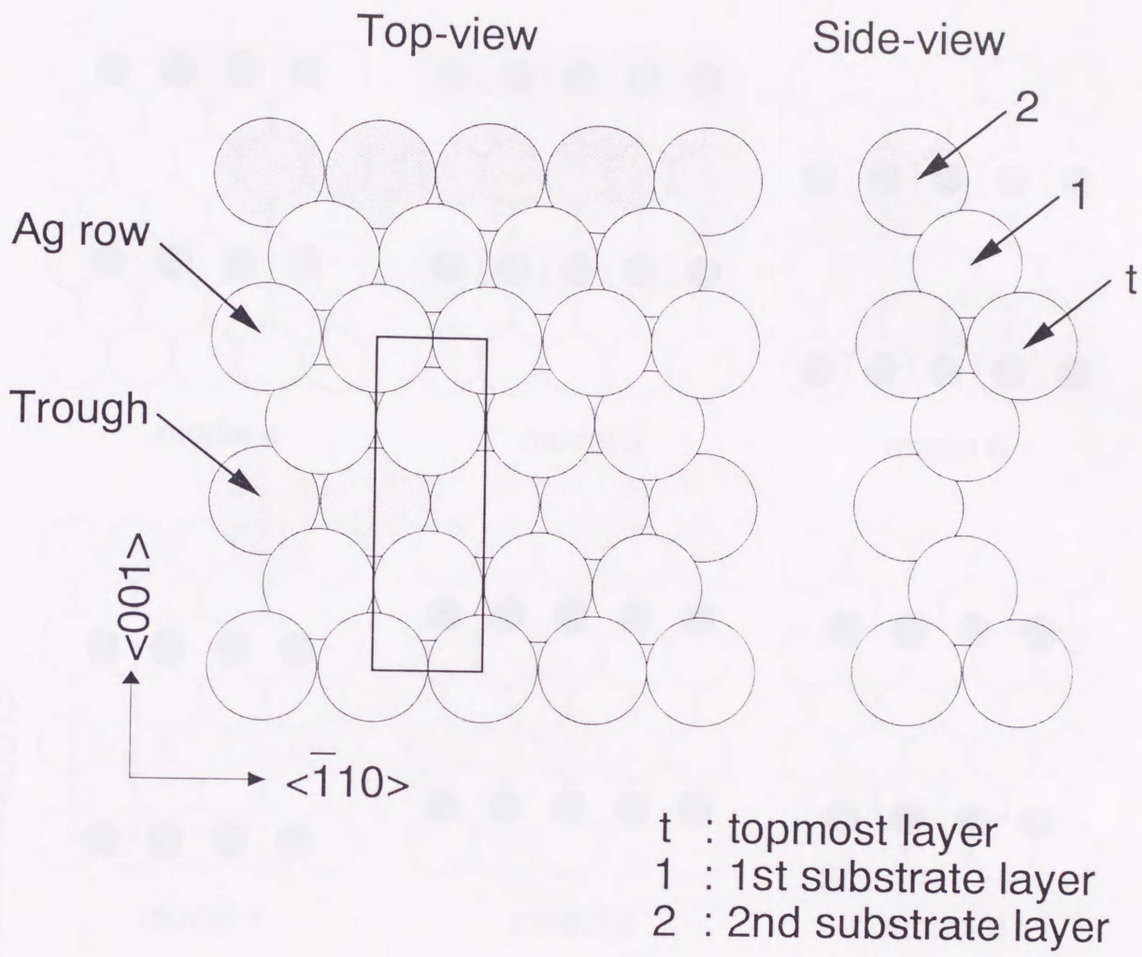

Figure 6-22. Top and side view of 1x2 missing row model neglecting oxygen atoms.

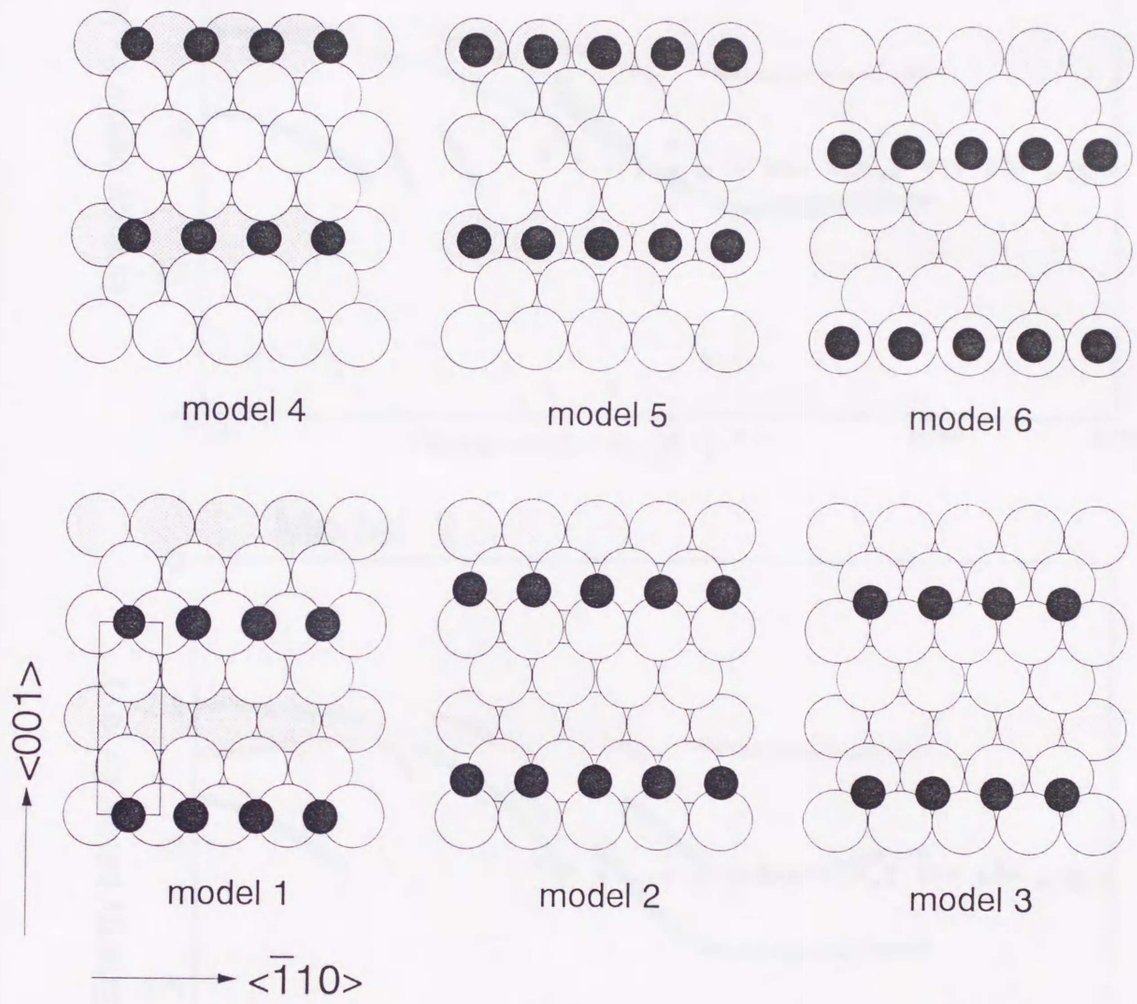

Figure 6-23. Possible 1x2 missing row models with oxygen atoms.

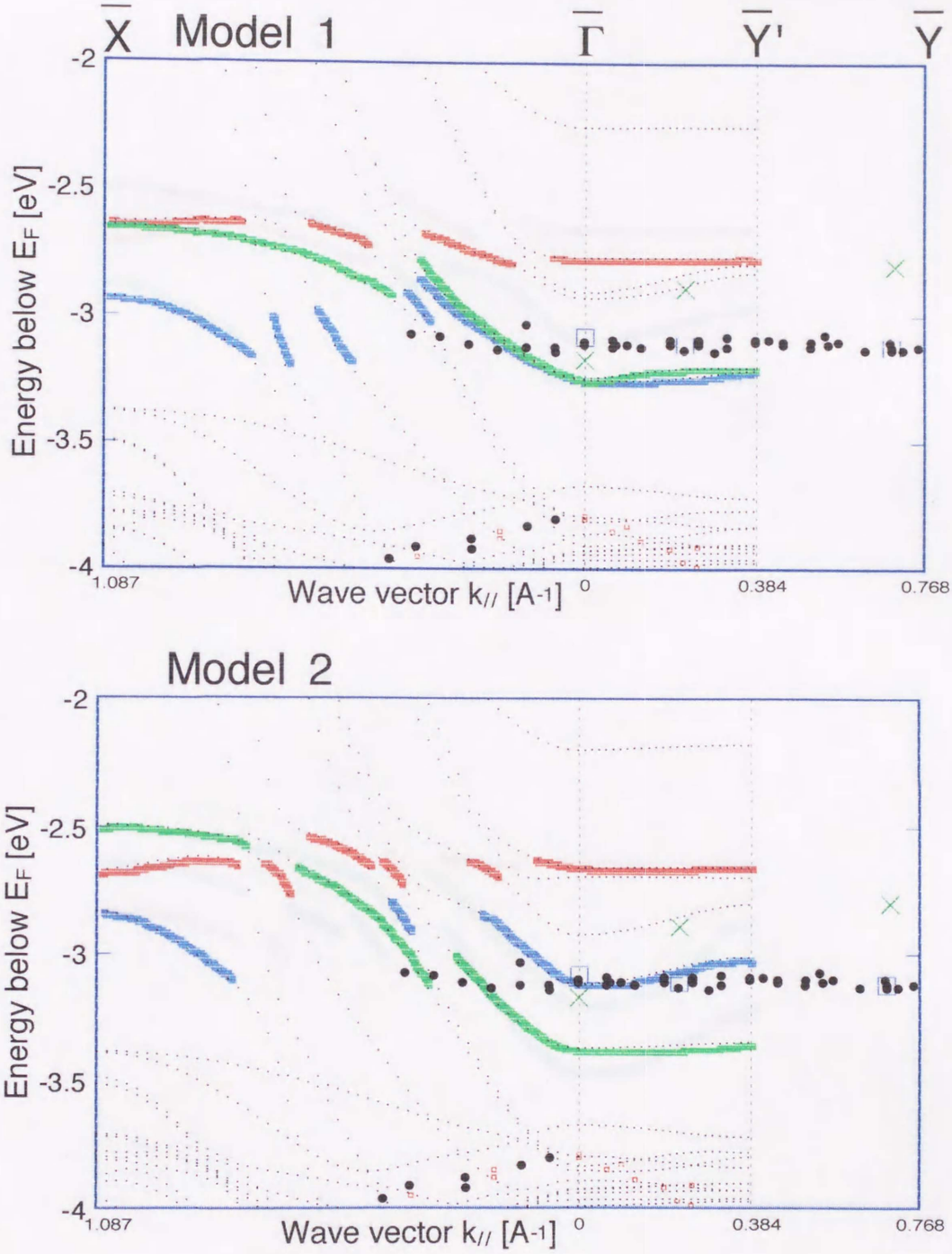

Figure 6-24(a). Plots of calculated energy bands of model 1 and 2 (denoted by dots) compared with experimental points given in Fig.6-20. Each calculated band, which has dominantly p_x, p_y and p_z character, is shaded for the purpose of easy recognition of the correspondence between calculation and experiment.

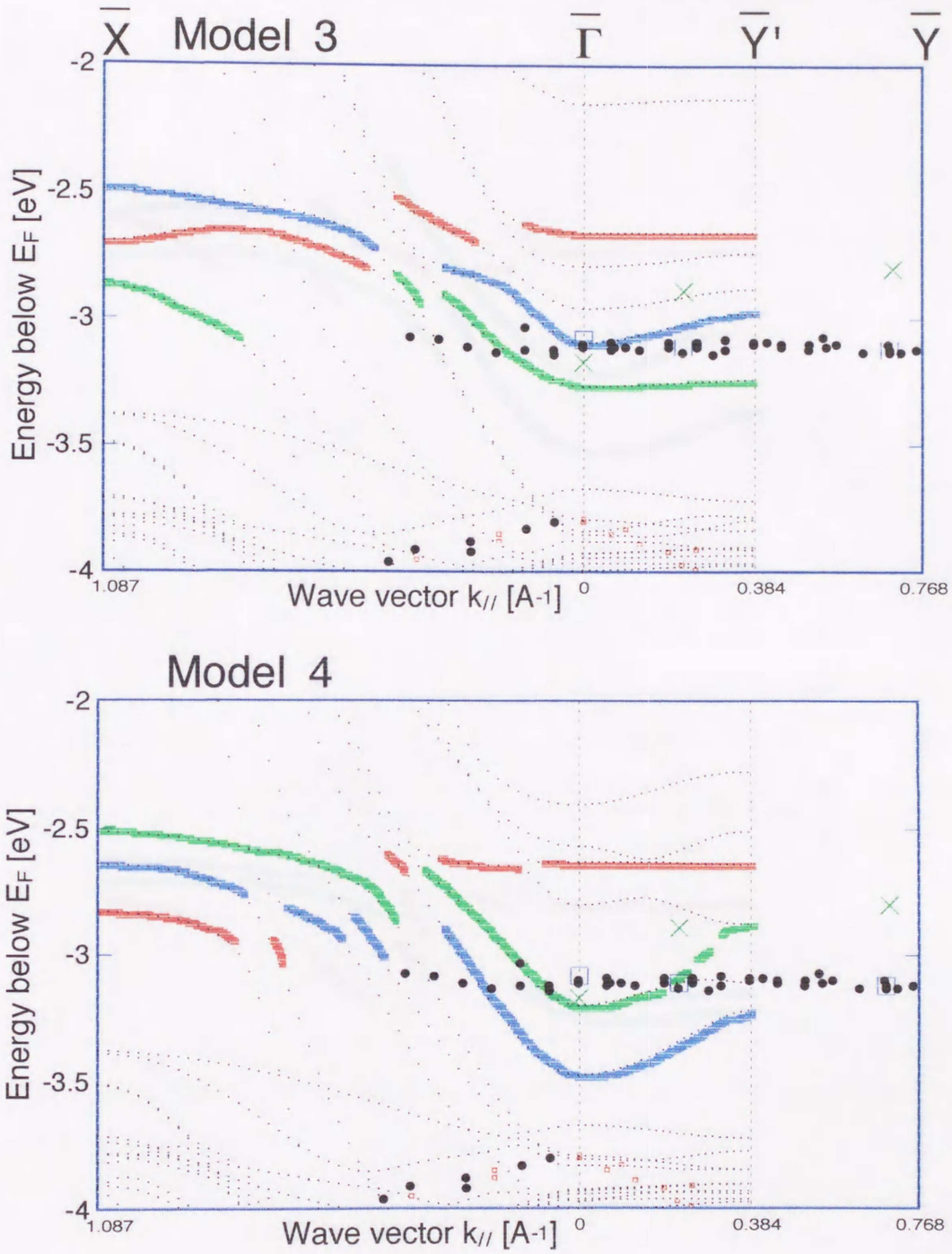

Figure 6-24(b). Plots of calculated energy bands of model 3 and 4 (denoted by dots) compared with experimental points given in Fig.6-20. Each calculated band, which has dominantly p_x, p_y and p_z character, is shaded for the purpose of easy recognition of the correspondence between calculation and experiment.

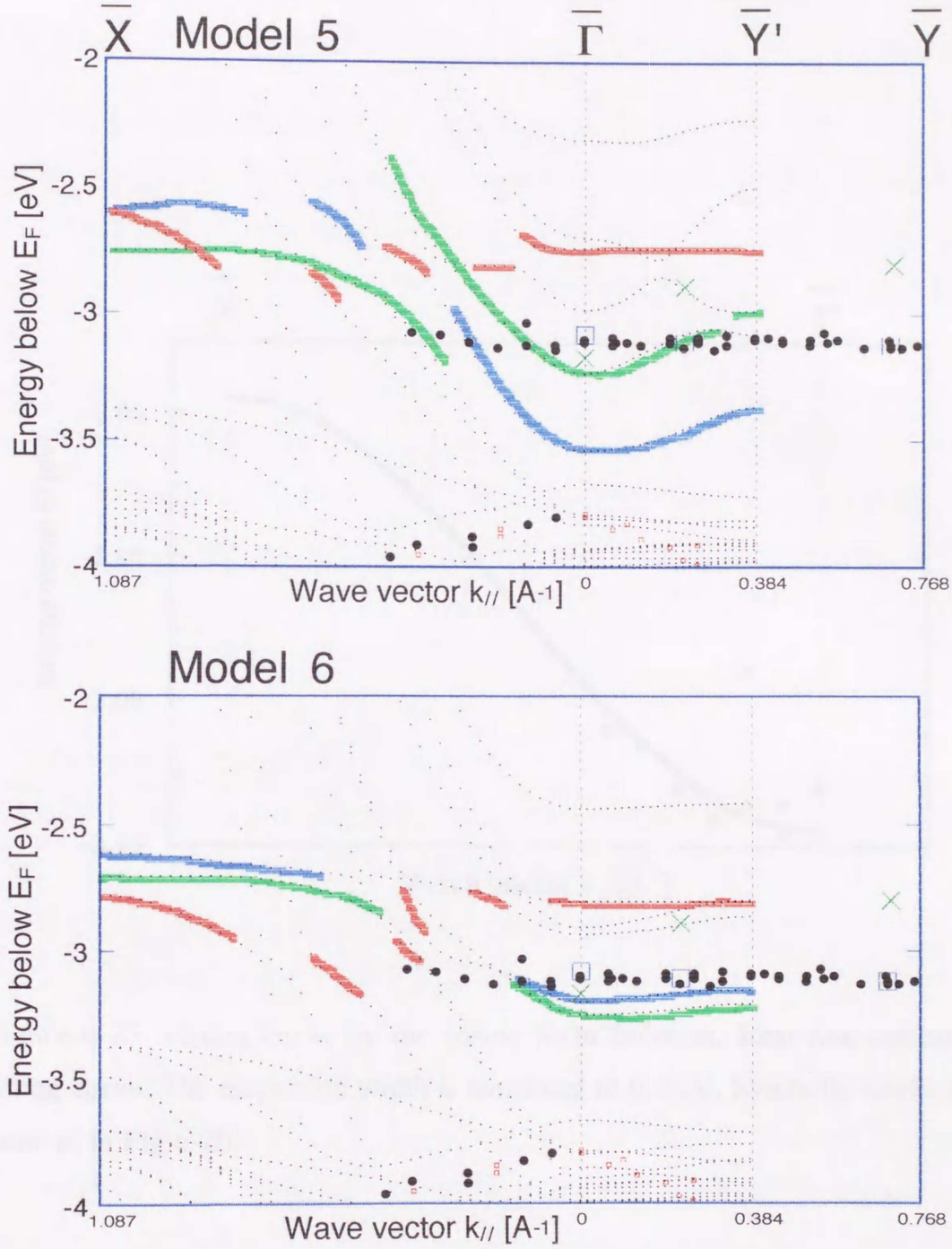

Figure 6-24(c). Plots of calculated energy bands of model 5 and 6 (denoted by dots) compared with experimental points given in Fig.6-20. Each calculated band, which has dominantly p_x, p_y and p_z character, is shaded for the purpose of easy recognition of the correspondence between calculation and experiment.

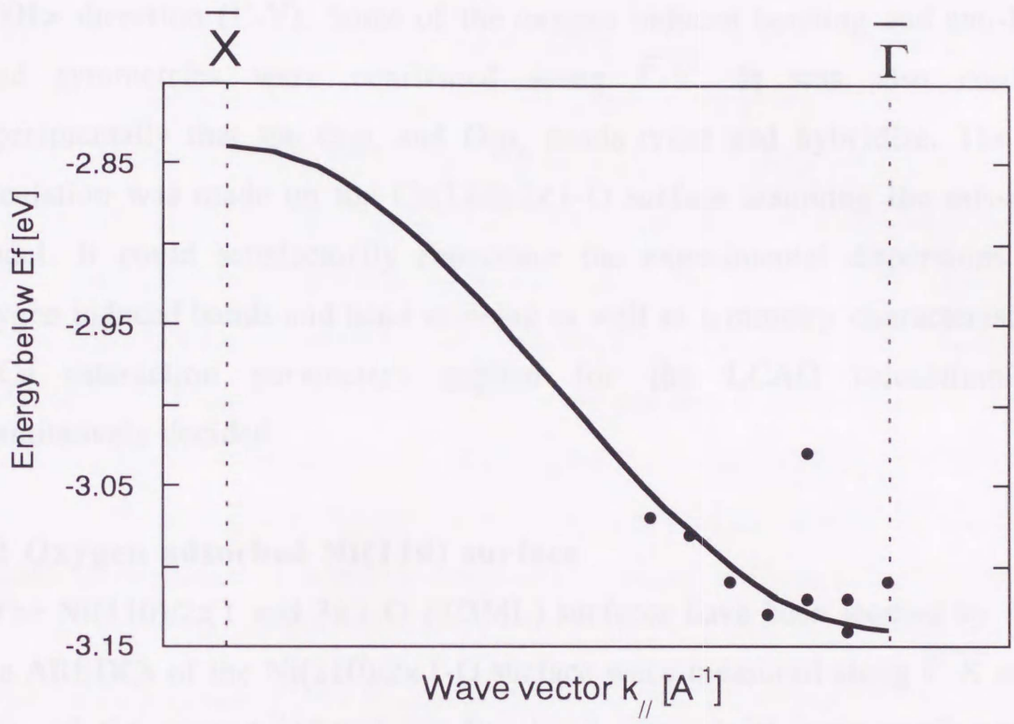

Figure 6-25. Fitting curve by the cosine form function. Real line indicates the fitting curve. The dispersion width is simulated to 0.3 eV. Symbolic marks are the same as in Fig.6-20.

Chapter 7 Conclusion

7.1 Oxygen adsorbed Cu(110) surface

The Cu(110)/2x1-O surface has been studied by ARUPS. The AREDCs of the Cu(110)/2x1-O surface were measured along the <$\bar{1}$10> direction ($\bar{\Gamma}$-$\bar{X}$) and <001> direction ($\bar{\Gamma}$-$\bar{Y}$). Some of the oxygen induced bonding and anti-bonding band symmetries were confirmed along $\bar{\Gamma}$-$\bar{Y}$. It was also confirmed experimentally that the O-p_y and O-p_z bands cross and hybridize. The LCAO calculation was made on the Cu(110)/2x1-O surface assuming the missing row model. It could satisfactorily reproduce the experimental dispersions of the oxygen induced bands and band crossing as well as symmetry characteristics. The O-Cu interaction parameters applied for the LCAO calculation were quantitatively decided.

7.2 Oxygen adsorbed Ni(110) surface

The Ni(110)/2x1 and 3x1-O (2/3ML) surfaces have been studied by ARUPS. The AREDCs of the Ni(110)/2x1-O surface were measured along $\bar{\Gamma}$-$\bar{X}$ and $\bar{\Gamma}$-$\bar{Y}$. Some of the oxygen induced bonding band symmetries were confirmed along $\bar{\Gamma}$-$\bar{Y}$. The AREDCs of the Ni(110)/3x1-O (2/3ML) surface were measured along $\bar{\Gamma}$-$\bar{X}$ and $\bar{\Gamma}$-$\bar{Y}$ for the first time. Some of the oxygen induced bonding band symmetries were confirmed along $\bar{\Gamma}$-$\bar{X}$ and $\bar{\Gamma}$-$\bar{Y}$. The LCAO calculations were made on the Ni(110)/2x1 and 3x1-O surface assuming the 2x1 and 3x1 missing row models. They reproduced the experimental dispersions of the oxygen induced bands for each and the O-Ni interaction parameters were quantitatively decided. The energy bands of the Ni(110)/3x1-O surface were reproduced and interpreted by the introduction of the O-O interaction and the oxygen on-site energy shift. With oxygen exposure lager than 10 L, the high-exposed Ni(110)/2x1-O surface was found. The ARUPS, WF and XPS measurements on this surface indicate the almost same results as the low-exposed Ni(110)/2x1-O surface. This suggests that

the high and low-exposed Ni(110)/2x1-O surfaces are the same structure, but it is still an open question.

7.3 Oxygen adsorbed Ag(110) surface

The Ag(110)/2x1-O surface has been studied by ARUPS. The AREDCs of the Ag(110)/2x1-O surface were measured along $\overline{\Gamma}$-$\overline{X}$ and $\overline{\Gamma}$-$\overline{Y}$. Some of the oxygen induced bonding band symmetries were confirmed along $\overline{\Gamma}$-$\overline{X}$ and $\overline{\Gamma}$-$\overline{Y}$. The LCAO calculation was made on the Ag(110)/2x1-O surface assuming the missing row model. And it reproduced the experimental dispersions of the oxygen induced bands as for symmetry characteristics.

The Ag(110)/1x2-O surface was newly found. It was confirmed that the Ag(110)/1x2-O surface is an oxygen induced reconstructed surface by UPS, WF, LEED and XPS measurements. We proposed a 1x2 missing row model. The AREDCs of the Ag(110)/1x2-O surface were measured along $\overline{\Gamma}$-$\overline{X}$ and $\overline{\Gamma}$-$\overline{Y}$. The LCAO calculation was made on the Ag(110)/1x2-O surface assuming the various 1x2 missing row models. Some revisions may be necessary to reproduce the result more accurately. For the purpose of deciding the substrate structure and the oxygen position, studies like PED, SEXAFS, STM and so on are expected.

Appendix Phase diagram

The phase diagram of oxygen adsorbed Ag(110) surface is shown in figure 6-26, while it is **in progress**. LEED patterns were observed at sample temperature 50, 100, 150 and 200 ℃, and at oxygen exposure of 10,000 and 20,000 L. The sample was kept at each constant temperature through the oxygen exposure. The notation *streak* denotes that the streaks through the integral orders parallel to the $<\bar{1}10>$ direction were observed. This suggests that the Ag-O rows along the <001> direction have grown on the surface. The phase boundary between nx1 and 1x2 phases seem to exist at ~100 ℃, depending dominantly on the sample temperature. However, it has been reported that the nx1 LEED patterns were observed by prepared at room tey perature (RT) [2,26,37,81]. We are planning the more study including at RT, and this should give important information on oxygen reconstruction mechanism.

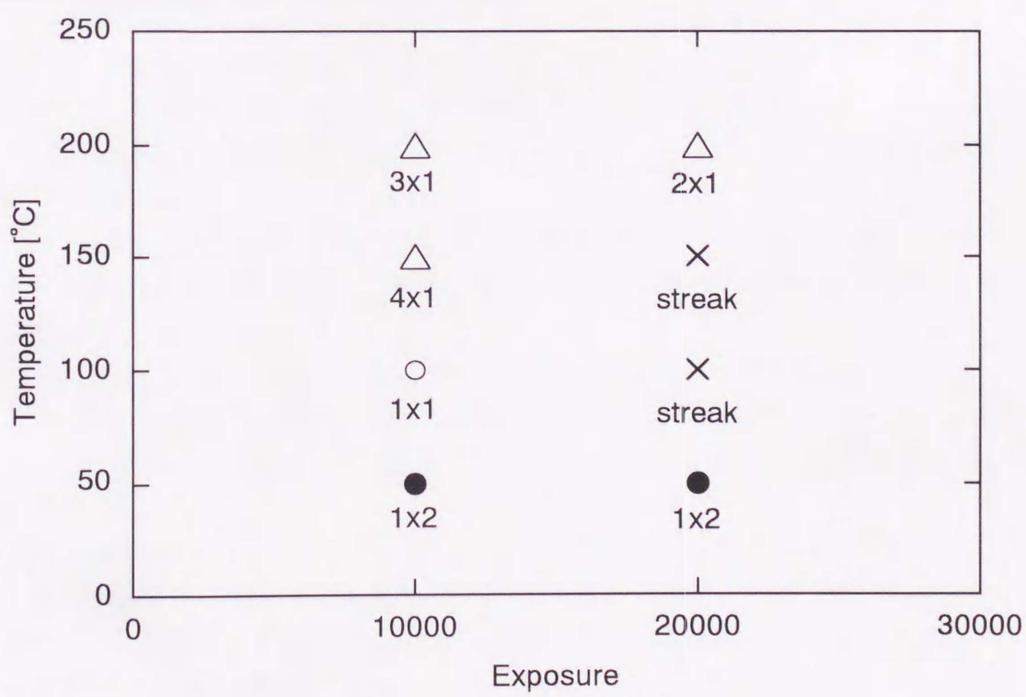

Figure 6-26. Phase diagram of oxygen adsorbed Ag(110) surface.

Acknowledgments

I would like to express my sincerest gratitude to Professor H. Fukutani for his continual encouragement, guidance and a great deal of advice. I have received valuable advice to complete the whole course of study from him. I am also grateful to Dr. K. Higashiyama for his relevant advice.

I thank Dr. T. Koide and Dr. H. Kato for the distribution of the sample and the equipment, and for the suggestion with the crystal preparation. I am greatly indebted to Dr. K. Yagi for his help with technical advice.

I wish to thank Mr. T. Kambe, Dr. K. Morikawa and Mr. M. Ohwada for their instruction in many aspects of experiments. I am grateful to my collaborator A. Yamane, and he stimulated me in the experiment. I am also grateful to Mr. K. Suzuki, Mr. S. Takeda, Mr. Y. Gunji, Mr. S. Yamazaki, Mr. D. Sekiba and Mr. H. Nakamizo for their experimental assistance.

Finally, I am greatly indebted to all the members of the Fukutani Laboratory for their hospitality and encouragement.

References

[1] F. Besenbacher and J.K. Norskov: Surface Sci. **44** (1993) 5

[2] H.A. Engelhardt and D. Menzel: Surface Sci. **57** (1976) 591

[3] D.J. Coulman, J. Wintterlin, R.J. Behm and G. Ertl: Phys. Rev. Lett. **64** (1990) 1761

[4] Y. Kuk, F.M. Chua, P.J. Silverman and J.A. Meyer: Phys. Rev. **B41** (1990) 163

[5] F. Bloch: Z. Physik **52** (1928) 555

[6] R. Feidenhans'l, F. Grey, M. Neilsen, F. Besenbacher, F. Jensen, E. Laegsgaard and I. Stensgaard: Phys. Rev. Lett. **65** (1990) 2027

[7] F. Jensen, F. Besenbacher, E. Laegsgaard and I. Stensgaard: Phys. Rev. **B41** (1990) 10233

[8] A.M. Baro, G. Binnig, H. Rohrer, Ch. Gerber, E. Stoll, A. Baratoff and F. Salvan: Phys. Rev. Lett. **52** (1984) 1304

[9] L. Ruan, F. Besenbcher, I. Stensgaard and E. Laegsgaad: Phys. Rev. Lett. **70** (1993) 4079

[10] L. Eierdal, F. Besenbcher, E. Laegsgaad and I. Stensgaard: Surface Sci. **312** (1994) 31

[11] T. Hashizume, M. Taniguchi, K. Motai, H. Lu, K. Tanaka and T. Sakurai: Japan. J. Appl. Phys. **30**(8B) (1991) L1529

[12] M. Taniguchi, K. Tanaka, T. Hashizume and T. Sakurai: Surface Sci. Lett. **262** (1992) L123

[13] T. Hashizume, M. Taniguchi, K. Motai, H. Lu, K. Tanaka and T. Sakurai: Surface Sci. **266** (1992) 282

[14] T. Simizu and M. Tsukada: Solid State Comm. **87** (1993) 193

[15] G.Ertl: Angew. Chem. **102** (1990) 1258

[16] V. Penka, K. Christmann and G. Ertl: Surface Sci. **136** (1984) 307

[17] M. Taniguchi, K. Tanaka, T. Hashizume and T. Sakurai: Surface Sci. **262** (1992) L123

[18] C. Backx, C.P.M. de Groot and P. Biloen: Surface Sci. **104** (1981) 300

[19] R.A. Didio, D.M. Zehner and E.W. Pluummer: J. Vac. Sci. Technol. **A61** (1984) 852

[20] R. Courths, B. Cord, H. Wern, H. Saalfeld and S. Hufner: Solid State Commun. **63** (1987) 619

[21] L.H. Tjeng, M.B.J. Meinders and G.A. Sawatzky: Surface Sci. **233** (1990) 163

[22] P. Pollak, R. Courths and St. Witzel: Surface Sci. **255** (1991) L523

[23] T. Komeda, Y. Sakisaka, M. Onchi, H. Kato, S. Masuda and K. Yagi: Surface Sci. **188** (1987) 45

[24] B. Weimert, J. Noffke and L. Fritsche: Surface Sci. **264** (1992) 365

[25] K.C. Prince, G. Paolucci and A.M. Bradshaw: Surface Sci. **175** (1986) 101

[26] L.H. Tjeng, M.B.J. Meinders and G.A. Sawatzky: Surface Sci. **236** (1990) 341

[27] K.C. Prince and A.M. Bradshaw: Surface Sci. **126** (1983) 49

[28] W. Segeth, J.H. Wijngaard and G.A. Sawatzky: Surface Sci. **194** (1988) 615

[29] M.P. Seah and W.A Dench: Surf. Interfacial Anal. **1** (1979) 1

[30] C.J. Powell: Surf. Sci. **44** (1974) 29; J. Vac. Sci. Technol **A3** (1985) 1338

[31] I.Lindau and W.E. Spicer: in Synchrotron Radiation Research, H. Winick and S. Doniach ed. (Plenum Press, New York, 1980)

[32] J.C. Slater and G.F. Koster: Phys. Rev. **94** (1954) 1498

[33] R. Ozawa, A. Yamane, K. Morikawa, M. Ohwada, K. Suzuki and K. Fukutani: Surface Sci. **346** (1996) 237

[34] D.A. Papaconstantopoulos, 'Handbook of the band structure of elemental solids' (Plenum Press, 1986)

[35] K. Suzuki, A. Yamane, R. Ozawa, Y. Gunji. K. Higashiyama and H. Fukutani: Surface Sci. **365** (1996) 248

[36] W. Heiland, F. Iberl, E. Taglauer and D. Menzel: Surface Sci. **53** (1975) 383

[37] H. Albers, W.J.J. van der Wal, O.L.J. Gijzeman and G.A. Bootsma: Surface Sci. **77** (1978) 1

[38] C.T. Campbell and M.T. Paffett: Surface Sci. **143** (1984) 517

[39] C.S. Fadley: Electron Spectroscopy, Theory, Techniques and Applications, C.R. Brundle and A.D. baker, Eds. (Pergamon Press, 1978) **II** (1)

[40] J.J. Yeh and I. Lindau: Atomic Data and Nuclear Data Tables **32** (1985) 1-155

[41] S. Takahashi, S. Kono, H. Sakurai and T. Sagawa: J. Phys. Soc. Jpn. **51**(10) (1982) 3296

[42] R. Courths, H. Wern, U. Hau, B. Cord, V. Bachelier and S. Hüfner: J. Phys. F: Mct. Phys. **14** (1984) 1559

[43] M. Canepa, P. Cantini, L. Mattera, E. Narducci, M. Salvietti and S. Terreni: Surface Sci. **322** (1995) 271

[44] A. Sandell, P. Bennich, A. Nilsson, B. Hernnäs, O. Björneholm and N. Mårtensson: Surface Sci. **310** (1994) 16

[45] M. Fink and J. Ingram: Atomic Data **4** (1972) 129 (Academic Press,Inc)

[46] S. Froyen and W.A. Harrison: Phys. Rev. **B20** (1979) 2420

[47] P.R. Norton, P.E. Bindner and T.E. Jackman: Surface Sci. **175** (1986) 313

[48] G. Kleinle, J. Wintterlin, G. Ertl, R.J. Behm, F. Jona and W. Moritz: Surface Sci. **225** (1990) 171

[49] S. Masuda, M. Nisijima, Y. Sakisaka and M. Onchi: Phys. Rev. **B25** (1982) 863

[50] G. Rovida and F. Pratesi: Surface Sci. **52** (1975) 542

[51] E. Zanazzi, M. Maglietta, U. Bardi, F. Jona and P.M. Marcus: J. Vac. Sci. Technol. **A1**(1) (1983) 7

[52] U. Dobler, K. Baberschke, J. Haase and A. Puschmann: Phys. Rev. Lett. **52** (1984) 1437

[53] M. Bader, A. Puschmann, C. Ocal and J. Haase: Phys. Rev. Lett. **57** (1984) 1437

[54] K. Baberschke, U. Dobler, L. Wenzel, D. Arvanitis, A. Baratoff and K.H. Rieder: Phys. Rev. **B33** (1986) 5910

[55] A. Puschmann and J. Haase: Surface Sci. **144** (1984) 559

[56] C. Benndorf, B. Egert, C. Nobl, H. Seidel and F. Thieme: Surface Sci. **92** (1980) 636

[57] P.H. Holloway and R.A. Outlaw: Surface Sci. **111** (1981) 300
[58] B. Voigtlander, S. Lehwald and H. Ibach: Surface Sci. **225** (1990) 162
[59] T. Komeda, Y. Sakisaka, M. Onchi, H. Kato, S. Masuda and K. Yagi: Surface Sci. **188** (1987) 32
[60] C. Backx, C.P.M. de Groot, P. Biloen and W.H.M. Sachtler: Surface Sci. **128** (1983) 81
[61] G. Bracco and R. Tatarek: Surface Sci. **251/252** (1991) 498
[62] K. Desinger, V. Dose, A. Goldmann, W. Jacob and H. Scheidt: Surface Sci. **154** (1985) 695
[63] C. Benndorf, C. Nobl and F. Thieme: Surface Sci. **126** (1983) 265
[64] H. Martensson and P.O. Nilsson: Phys. Rev. **B30** (1984) 3067
[65] A.M. Bradshaw, D. Menzel and M. Steinkilberg: Faraday Disc. Chem. Soc. **58** (1974) 46
[66] P. Heimann, J. Hermanson, H. Miosga and H. Neddermeyer: Surface Sci. **85** (1979) 263
[67] S. Kevan: Phys. Rev. **B28** (1983) 4822
[68] D.F. Mitchell, P.B. Sewell and M. Cohen: Surface Sci. **69** (1977) 310
[69] J.C. Fuggle and D. Menzel: Surface Sci. **53** (1975) 21
[70] W. Jacob, V. Dose and A. Goldmann: Appl. Phys. **A41** (1985) 145
[71] B. Reihl, R.R. Schlitter and H. Neff: Phys. Rev. Lett. **52**(20) (1984) 1826
[72] B. Reihl, R.R. Schlitter and H. Neff: Surface Sci.**152/153** (1985) 231
[73] Horst Niehus and George Cosma: Surface Sci. **140** (1984) 18
[74] J. Lapujoulade, Y.le. Cruer, M. Lefort, Y.Lejay and E. Mauerel: Surface Sci. **118** (1982) 103
[75] R. Feidenhans'l and I. Stensgaard: Surface Sci. **133** (1983) 453
[76] A.G.J. de Wit, R.P.N. Bronckers and J.M. Fluit: Surface Sci. **82** (1979) 177
[77] R.P.N. Bronckers and A.G.J. de Wit: Surface Sci. **112** (1981) 133
[78] E. Van. de Riet, J.B.J. Smeers, J.M. Fluit and A. Niehaus: Surface Sci. **214** (1989)
[79] M. Canepa, P. Cantini, F. Fossa, L. Mattera and S. Terreni: Phys. Rev. B **47**(23) (1993) 47
[80] M. Canepa, M. Salvietti, M. Traverso and L. Mattera: Surface Sci. **331-333** (1995) 183
[81] Y. Matsumoto, Y. Okawa and K. Tanaka: Surface Sci. **336** (1995) L762

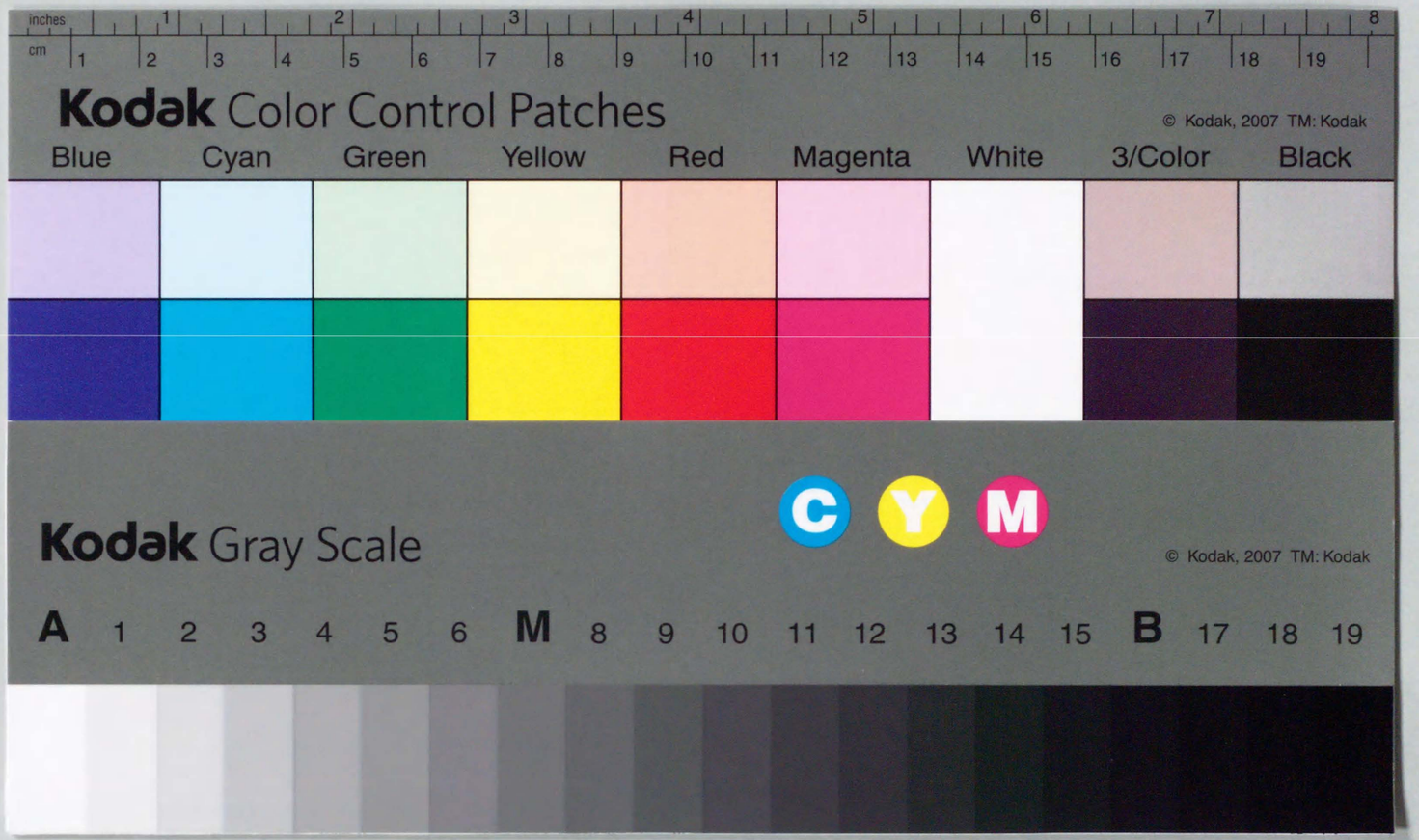
inches
cm
Kodak Color Control Patches
© Kodak, 2007 TM: Kodak
Blue
Cyan
Green
Yellow
Red
Magenta
White
3/Color
Black
Kodak Gray Scale
C
Y
M
© Kodak, 2007 TM: Kodak
A 1 2 3 4 5 6 M 8 9 10 11 12 13 14 15 B 17 18 19